Dissipative phases in open quantum systems

Dissertation

zur Erlangung des akademischen Grades
doctor rerum naturalium
(Dr. rer. nat.)

vorgelegt

dem Fachbereich für Physik, Mathematik und Informatik
der Johannes Gutenberg-Universität Mainz

Oksana Chelpanova
geboren in Cherson, Ukraine

Mainz, den 16. Januar 2025

Oksana Chelpanova
Institut für Physik
KOMET 7
Johannes Gutenberg-Universität Mainz
Staudingerweg 7
55128 Mainz

D77 / Dissertation der Johannes Gutenberg-Universität Mainz

Erster Gutachte: J-Prof. Dr. Jamir Marino

Zweiter Gutachter: Prof. Dr. Claudiu Genes

Datum der mündlichen Prüfung: 25. Februar 2025

ABSTRACT. Phase transitions are widespread phenomena occurring during the early stages of the Universe as well as in our everyday experience. Many systems enjoy similar critical properties governed by symmetries, range of interaction, and dimensionality, disregarding microscopic properties. At the same time, some of them are much easier to recreate in the lab than others. A particular boost in the investigation of phase transitions is associated with the development of quantum simulators, such as light-matter interfaces, trapped ions, Rydberg atoms, etc., which allow to controllably study critical properties at near-zero or finite temperatures. Such simulators allow for tuning of parameters, which can be quite robust in the real-world system, driving transition dynamically as well as giving access to real-time observables. It is also important that these platforms enable not only coherent control of couplings but also can host incoherent, dissipative channels due to the environment in which they are embedded. Over the last years, such dissipations have been shown to be more than just a source of decoherence, but rather a resource for more sophisticated control of dynamics, allowing the generalization of new phases or stabilizing dynamical regimes. In this thesis, we study phase transitions in the experimentally accessible analogous quantum simulators. We start with a spintronics-inspired dissipative model, which hosts various phases generated through the competition of continuous and discrete symmetries and incoherent drive and dissipations. The model possesses a rich dynamical phase diagram, combining stationary and non-stationary regimes. Then, we go deeper into the experimental implementation of the models with different atomic degrees of freedom and see how the interplay of spin and momentum can result in non-stationary phases, manifesting spin-momentum entanglement. We also examine a particular role of dissipation in this case, showing how it helps stabilize dynamical phases and gives a perspective for non-destructive monitoring of the system properties. The thesis covers the implementation of dissipative models in quantum simulators and their relevant dynamical aspects.

ZUSAMMENFASSUNG. Phasenübergänge sind weit verbreitete Phänomene, die sowohl in der Frühphase des Universums als auch in unserer täglichen Erfahrung auftreten. Viele Systeme weisen ähnliche kritische Eigenschaften auf, die von Symmetrien, der Reichweite der Wechselwirkung und der Dimensionalität bestimmt werden, wobei mikroskopische Eigenschaften außer Acht gelassen werden. Gleichzeitig lassen sich einige von ihnen im Labor viel leichter nachbilden als andere. Ein besonderer Aufschwung bei der Erforschung von Phasenübergängen ist mit der Entwicklung von Quantensimulationen verbunden, wie z.B. Licht-Materie-Grenzflächen, gefangene Ionen, Rydberg-Atome usw., die es ermöglichen, kritische Eigenschaften bei Temperaturen nahe Null oder bei endlichen Temperaturen kontrolliert zu untersuchen. Solche Simulationen ermöglichen die Einstellung von Parametern, die im realen System recht robust sein können, indem sie den Übergang dynamisch steuern und Zugang zu den Echtzeit-Beobachtungsdaten bieten. Wichtig ist auch, dass diese Plattformen nicht nur eine kohärente Steuerung von Kopplungen ermöglichen, sondern aufgrund der Umgebung, in die sie eingebettet sind, auch inkohärente, dissipative Kanäle aufnehmen können. In den letzten Jahren hat sich gezeigt, dass solche Dissipationen mehr als nur eine Quelle der Dekohärenz sind, sondern vielmehr eine Ressource für eine ausgefeiltere Kontrolle der Dynamik, die die Verallgemeinerung neuer Phasen oder die Stabilisierung dynamischer Regime ermöglicht. In dieser Arbeit untersuchen wir Phasenübergänge in den experimentell zugänglichen analogen Quantensimulatoren. Wir beginnen mit dem von der Spintronik inspirierten dissipativen Modell, das verschiedene Phasen beherbergt, die durch die Konkurrenz von kontinuierlichen und diskreten Symmetrien und inkohärenten Antrieben und Dissipationen entstehen. Das Modell verfügt über ein reichhaltiges dynamisches Phasendiagramm, das stationäre und nicht-stationäre Zustände kombiniert. Anschließend gehen wir näher auf die experimentelle Umsetzung der Modelle mit verschiedenen atomaren Freiheitsgraden ein und sehen, wie das Zusammenspiel von Spin und Impuls zu nicht-stationären Phasen führen kann, in denen sich die Spin-Moment-Verschränkung manifestiert. Wir untersuchen auch die besondere Rolle der Dissipation in diesem Fall und zeigen, wie sie zur Stabilisierung der dynamischen Phasen beiträgt und eine Perspektive für eine zerstörungsfreie Überwachung der Systemeigenschaften bietet. Die Arbeit befasst sich mit der Implementierung dissipativer Modelle in Quantensimulatoren und ihren relevanten dynamischen Aspekten.

Contents

Publications and Author's contributions

This thesis is a cumulative dissertation based on the following publications:

[1] **Oksana Chelpanova**, Alessio Lerose, Shu Zhang, Iacopo Carusotto, Yaroslav Tserkovnyak, and Jamir Marino. *Intertwining of lasing and superradiance under spintronic pumping*, Phys. Rev. B 108, 104302 (2023).

[2] **Oksana Chelpanova**, Kushal Seetharam, Rodrigo Rosa-Medina, Nicola Reiter, Fabian Finger, Tobias Donner, and Jamir Marino. *Dynamics of spin-momentum entanglement from superradiant phase transitions*, Phys. Rev. Research 6, 033193 (2024).

Preliminary results are shown in Chapter 5 are based on the ongoing research:

Chelpanova, O., Hosseinabadi, H., Marino, J. *Discrete Truncated-Wigner dynamics from Keldysh field theory*, in preparation (2025)

Chelpanova, O., Hosseinabadi, H., Marino, J. *Semi-classical dynamics of spin chains in the presence of non-Markovian environment*, in preparation (2025)

Complementary to the main direction of the thesis, I've been studying commensurate-incommensurate transition in ion chains. The results are published in

[3] **Oksana Chelpanova**, Shane P Kelly, Giovanna Morigi, Ferdinand Schmidt-Kaler, Jamir Marino. *Injection and nucleation of topological defects in the quench dynamics of the Frenkel-Kontorova model*, EPL 143 25002 (2023).

[4] **Oksana Chelpanova**, Shane P. Kelly, Ferdinand Schmidt-Kaler, Giovanna Morigi, and Jamir Marino. *Dynamics of quantum discommensurations in the Frenkel-Kontorova chain*, Phys. Rev. B 109, 214107 (2024).

Author's contributions

Author's contributions: I carried out most of the calculations (except Gilbert damping derivation in the Appendix of [1]) and all numerical simulations reported in the papers under the guidance and recommendations of my collaborators and supervisor.

Abbreviations

AMO: atomic, molecular and optical physics

BEC: Bose-Einstein condensate

QED: quantum electrodynamics

MF: mean field

SR: superradiance

TWA: truncated Wigner approximation

DTWA: discrete truncated Wigner approximation

RG: renormalization group

IR: Infrared

H.C.: Hermitian conjugate

RWA: Rotating Wave Approximation

NV: nitrogen-vacancy

HS: Hubbard-Stratonovich

BBGKY: Bogoliubov-Born-Green-Kirkwood-Yvon

—

CHAPTER 1

Introduction

The phenomena of the phase transitions are very broad, including changes in the aggregate state of water when varying the temperature and emergence of magnetization in metal when applying a magnetic field, as well as a set of high-energy transitions in the early Universe, such as a transition from the plasma of quarks and gluons to hadronic matter, breaking of the electroweak symmetry by separation of electromagnetic interaction into two, inflation phase transition, separation of the sterile neutrino, etc. A comprehensive study of the various phase transitions is necessary for our deep understanding of physics, including connections between different areas, such as high energy physics and condensed matter, as well as practical applications in technologies.

The theoretical development of the theory of phase transitions was stimulated by the experiments with liquid Helium [5], where the specific heat displayed discontinuity as a function of temperature (so-called λ-transition), with the further classification of the first- and second order phase transitions in the work of Ehrenfest [6]. The attempts to generalize the description of phase transitions were made by Landau in Kharkiv later on when he introduced the phenomenological description in terms of the order parameter, which is equal to zero in one phase but develops a non-zero value in another [7]. The idea is to assume that near transition, the free energy can be expanded in powers of the order parameter (for instance, magnetization). The form of the expansion is mostly set by symmetry considerations and physical arguments. In equilibrium, the order parameter minimizes the free energy, and depending on whether the temperature is below or above the critical value, such an order parameter is finite or zero.

The formalism was later expanded to Ginzburg-Landau theory by encountering spatial inhomogeneity of the order parameters (local order parameter), allowing the description of the development of spatial ordering in the second-order phase transitions. Ginzburg criterion states that to maintain the mean-field theory description correct, the order parameter fluctuations must be much smaller than the mean-field value [8]. The Landau (Ginzburg-Landau) theory works very well for systems where the quantum fluctuations are weak, such as superfluidity. However, the theory becomes invalid in the vicinity of the second-order phase transition in low dimensions, where spatial fluctuations diverge at an arbitrary length scale (divergent correlation length). Therefore, higher-order corrections in perturbation theory should be accounted for.

The giant leap in the investigation of phase transitions was the development of the renormalization group (RG) theory, which arose from the examination of the scaling behavior of effective couplings in the Infrared (IR), i.e., low-energy, limit of the theory [8, 9]. The idea is to separate relevant (slow) and irrelevant (fast) degrees of freedom at criticality and systematically integrate irrelevant corrections. The important development of the theory includes Kadanoff spin block constructions along with the field-theoretical renormalization techniques [8, 10–13]. The RG procedure shows the relevant couplings of the model scale with the energy scale on which they are observed (the value of the observed coupling is dressed by the fast degrees of freedom, which we disregard). The correct evaluation of the couplings and their scaling allows the building of RG flows, which characterize the model at criticality [13].

Many microscopically distinct models have been shown to enjoy identical sets of critical exponents, resulting in the notion of universality classes [10, 12–14]. The explanation of this phenomenon is that in the long-wavelength limit, the phase transition is mostly determined by the dimensionality, symmetries (conservation laws), and range of the interaction, while microscopic details are washed out. This result is crucial for connecting physics in different research fields. Importantly, even though all models have quantum constituents on a microscopic level, the long-wavelength limit, in many cases, results in purely classical dynamics, especially for models with all-to-all interactions. The classification covers classical phase transitions as well as quantum ones, for which quantum fluctuations dominate the thermal ones. The quantum phase transition is characterized by the discontinuity in the ground state spectrum when the non-thermal parameter is varied [15] and can be found, for instance, in magnetism (see Mott metal-insulator transition in Hubbard models).

An important direction in physics at criticality is non-equilibrium properties and emergent phenomena. Such dynamics can be induced in different ways, for instance, by adding perturbation to the equilibrium system, which breaks its symmetry. Nowadays, an emergent theory and dynamical phase transition can be studied with various quantum simulators. Novel quantum simulators, such as cold atoms (including Bose-Einstein condensate [16–19], atoms trapped in the lattice potential [20–23] or (and) in tweezers [24, 25]), trapped ions [26–28], superconducting circuits [29], light-matter interfaces [30–32], allow not only for the implementation of different models, such as the Dicke model, Hubbard model, Ising model, and sine-Gordon model, but also for a high degree of tunability of different model parameters, which, as a rule, are quite robust in the existing physical systems. Such a degree of control allows the exploration of various phase transitions, and real-time access for observables allows for the exploration of transient out-of-equilibrium phenomena, such as the establishment of phases and the build-up of correlations. The non-equilibrium aspect of phase transition, like emergent self-organization, is an important resource for realizing novel phases and non-trivial

dynamical behavior, which are inaccessible when the system is in thermal equilibrium. Some examples of such phases are lasing and superradiance (SR) [33], Bose-Einstein condensate (BEC) of polaritons [17], time crystals [34–36], supersolid [37–45], etc.

An important property of quantum simulators is their coupling to the environment, which allows to switch between closed systems and open ones. For instance, atoms are coupled to the fluctuations of the electromagnetic field, which results in a finite lifetime of their excited states and, as follows, a spontaneous decay [46, 47]. In cavity quantum electrodynamics (QED), the mirrors have finite transparency, which results in the leaking of photons out and their finite lifetime. All this coupling to the exterior of quantum simulators results in the *dissipation*, breaking detail balance and disabling equilibrium.

Naively, dissipation may be considered to have a negative impact on the dynamics, washing out correlations over time. However, detailed studies revealed that dissipation might be utilized as well as a coherent drive to engineer desired phases and properties. It has been shown that adding drive and dissipation may result in novel critical behavior beyond one predicted for dynamical phase transitions [48, 49]. In particular, studying the dissipative dynamics with a non-local dissipation profile revealed a possibility of a distinct universality class beyond long-range Ising [50, 51]. The further clever utilization of dissipation includes the generation of dark states [52–55], stabilization of different phases [56, 57], and novel applications such as superradiant lasers [58, 59] etc.

In this work, we concentrate on experimentally accessible dissipative phase transitions realized with quantum simulators. There are a few benefits of such an approach, which we summarize below.

- **High degree of tunability.** Modern quantum simulators propose a high degree of control, allowing tuning couplings and level splittings of the model and allowing studying various classical and quantum phase transitions.
- **Dynamical control.** The system can be initialized in the excited state/ couplings can be changed during dynamics, resulting in non-equilibrium phenomena, such as dynamical phase transitions and non-equilibrium steady-states.
- **Coupling to the environment.** Quantum simulators allow exploring dynamical regimes with strong and weak dissipation induced by the coupling to the external degrees of freedom (environment). Such dissipation may result in novel dynamical phenomena, such as non-stationary phases, non-equilibrium steady states, etc., as well as can be used for non-destructive monitoring of the system [60].

Through this thesis, we consider transitions that can be implemented via cold atoms in the cavity system. We also consider different mechanisms for implementing desired

models with different degrees of freedom of particles, such as spin or momentum of atoms.

Focus of this thesis

This thesis is dedicated to exploring the emergent self-organized phases in the presence of dissipation. Starting from transitions in the dissipative collective model, inspired by the spintronics setup, we slowly increase the level of complexity of models under consideration, exploring later on the interplay of different degrees of freedom, which results in no-stationary states. Then, we concentrate on non-equilibrium dynamics and introduce a method to account for quantum corrections. In the end, we also revisited the nature of dissipations and studied more general forms of time non-local dissipations. The thesis explores out-of-equilibrium properties of many-body systems in the presence of dissipations.

This thesis follows the following structure:

- **Chapter 2** introduces the platform under consideration and the main theory concepts and methods.
- **Chapter 3** includes publication [1] where we study dynamical phase diagram of spintronics-inspired model. We examine how the competition of discrete and continuous symmetries, as well as incoherent pump and dissipation, give rise to exotic dynamical phases in such a platform.
- **Chapter 4** includes publication [2] where we study dynamics of experimentally feasible model with multi-level atoms, where each level is a hybrid combination of different spin and momentum states. We show that self-organization transitions in such a system are much richer, including oscillatory phases unavailable in two-level systems. Moreover, there is an extensive part of the phase diagram where the spin and momentum of atoms are entangled. Such entanglement is stable under the presence of the dissipation (finite lifetime of the cavity mode), and actually, it is stabilized by the cavity losses since this dissipation makes the system relax into the state with proper entanglement.
- In **Chapter 5**, we develop a semiclassical method to examine quantum effects in dissipative spin models. We also discuss how the formalism can be extended to a case when the environment has a memory and system dynamics become non-Markovian.
- **Chapter 6** includes conclusion and outlook.

CHAPTER 2

Theoretical framework

This chapter contains minimal preliminary knowledge, which was used to derive the main results in the first part of this thesis. In particular, we discuss

- Lindblad master equation as a tool for the description of the dissipative systems
- Phase transition in the Dicke model and Tavis-Cummings model
- Cavity QED simulation of the Dicke model

2.1. Description of the dynamics of open quantum systems

The core of this part of the thesis is built around dynamics in many-body open quantum systems. Here, we discuss the origin of the 'open' part and how it can be treated efficiently with the Lindblad master equation. We start with a brief overview of the method, adding some technical steps below.

2.1.1. *Introduction*

In most practical applications, quantum systems are not isolated but embodied in some environment, which can have a nontrivial impact on them. It can be a gas of molecules at a given temperature that scatters elastically or non-elastically with particles in the system, or a magnetic material that creates an effective magnetic field in the system, etc. A famous example is the finite linewidth of the spectral lines, which originate from the coupling of atoms to the modes of the electromagnetic field [61]. Treating such 'system plus environment' models can form a formidable challenge since, even though the system part may contain just a few particles, the environment, as a rule, is a macroscopic object containing $\propto 10^{23}$ particles. The solution is to 'integrate out' environment and concentrate on the effective dynamics of the system.

Such procedure, under some assumptions, results in a Lindblad master equation, which describes the evolution of the system density matrix $\hat{\rho}$ and reads

$$\dot{\hat{\rho}} = -i[\hat{H}, \hat{\rho}] + \sum_i \gamma_i \mathcal{D}[\hat{L}_i]. \tag{2.1}$$

Dissipation channel	Jump operator, $\hat{L}_i$
Spin loss	$\hat{\sigma}_i^-$
Spin pump	$\hat{\sigma}_i^+$
Spin deplaning	$\hat{\sigma}_i^z$
Photon loss	$\hat{a}$

TABLE 2.1. Dissipation channels considered in this thesis

Here $\hat{H}$ is the Hamiltonian of the system part, $\mathcal{D}[\hat{L}_i]$ are dissipators with jump operators $\hat{L}_i$ and dissipation rates γ_i. For each jump operator $\hat{L}_i$ the dissipator term is given by

$$\mathcal{D}[\hat{L}_i] = \hat{L}_i \hat{\rho} \hat{L}_i^\dagger - \frac{1}{2}\left\{\hat{L}_i^\dagger \hat{L}_i, \hat{\rho}\right\}, \tag{2.2}$$

where $\{\cdot,\cdot\}$ is anti-commutator. The dissipation rates γ_i are determined by the correlation functions of the bath and can be evaluated from the bath spectral function.

The structure of the dissipator $\mathcal{D}[\hat{L}_i]$ is the following. The term $\left\{\hat{L}_i^\dagger \hat{L}_i, \hat{\rho}\right\}$ can be absorbed into the Hamiltonian, making it non-Hermitian, $\hat{H} \to \hat{H} - \sum_i \frac{i\gamma_i}{2} \hat{L}_i^\dagger \hat{L}_i$, and describes the relaxation (decay) of the system towards the steady state. The term $\hat{L}_i \hat{\rho} \hat{L}_i^\dagger$ is called a recycling term, and it redistributes the excitation lost from the excited state between other states [62].

We consider a few common dissipation channels in this thesis, summarized in Table 2.1. The first one is given by the jump operator $\hat{L} = \hat{a}$ and describes photon decay with the rate $\gamma_i = \kappa$. Precisely, if the system contains a quantized photon field, described by the field operator $\hat{a}$, this dissipation channel describes a finite lifetime of this cavity photon, $\propto \kappa^{-1}$. In the cavity QED platform, this dissipation channel describes leaking the photon from the cavity. Another dissipation channel describes a spin loss process, and it is given by the jump operator $\hat{L}_i = \hat{\sigma}_i^-$. This dissipator favors spin to the spin-down polarized state and models the transition of spin from the excited to the ground state through the emission of the photon to the environment. This process is responsible for the finite lifetime of the excited states. Similarly, spins can be incoherently driven to the excited states, with the jump operators $\hat{L}_i = \hat{\sigma}_i^+$. Last but not least, spins can experience dephasing, which results in the loss of the coherences (averaging of the non-diagonal elements of the density matrix to zero over time), which model, for instance, coupling to the fluctuating infinite temperature electromagnetic field. Spin dephasing is modeled in the Lindblad master equation with the jump operator $\hat{L}_i = \hat{\sigma}_i^z$.

The dissipative dynamics for the density matrix $\hat{\rho}$ according to Eq. (2.1) can be rewritten as the stochastic average over individual trajectories. According to this method, instead of solving dynamics for the density matrix, one can evaluate stochastic dynamics for the wave-function [62]. The stochastic unraveling of the Lindblad master equation is commonly used to perform memory-efficient calculations: given a Hilbert

space of dimension N_H, the density matrix is specified by N_H^2 complex numbers, while it is needed only N_H numbers to specify the pure state. If the number of quantum trajectories is below N_H, the stochastic description is more efficient [46]. According to the method, the dissipative dynamics are given by the non-Hermitian Hamiltonian $\hat{H} - \sum_i \frac{i\gamma_i}{2} \hat{L}_i^\dagger \hat{L}_i$, interrupted randomly by the stochastic jumps corresponding to the recycling term $\hat{L}_i \hat{\rho} \hat{L}_i^\dagger$. These jumps ensure the correct normalization of the wave function in time (note that non-Hermitian Hamiltonian does not preserve normalization). For a two-level system with spontaneous decay, $\hat{L} = \sigma^-$, the non-Hermitian part governs relaxation, and the recycling term governs the spontaneous projection of the spin on the ground state. While for some problems, for instance, post-selection [63], the non-Hermitian Hamiltonian gives reasonable results, the vast majority of the quantum mechanical tasks need to be solved accurately, which can be achieved with the quantum trajectories or, equivalently, Lindblad master equation (of course, under some restrictions on bath and system).

Below, we present a sketch of the derivation of the Lindblad master equation for completeness. The more detailed discussion and derivations are given in Refs. [47, 61, 64] and many others.

2.1.2. *Derivation of the Lindblad master equation*

Consider the dynamics of the system interacting with the environment, which consists of a set of Harmonic oscillators. The total Hamiltonian reads

$$\hat{H} = \hat{H}_s + \hat{H}_b + \hat{H}_{sb} \tag{2.3}$$

where $\hat{H}_s$ describes the dynamics of the system, $\hat{H}_b = \sum_k \omega_k \left(\hat{f}_k^\dagger \hat{f}_k + \frac{1}{2} \right)$ is the Hamiltonian of the bath, with $\hat{f}_k$[1] a bath annihilation operator, and $\hat{H}_{sb}$ describes linear interaction between system and the bath. The most general form of such interaction is

$$\hat{H}_{sb} = \sum_{ki} \left(\lambda_{ik} \hat{f}_k^\dagger \hat{L}_i + \text{H.C.} \right) = \sum_{ik} \hat{H}_{ik} \tag{2.4}$$

where indices k and i refer to bath and system degrees of freedom, and we denote Hermitian conjugate (H.C.). Here, we include only linear coupling for simplicity. We also neglect couplings of the form $\hat{f}_k O_i + \text{H.C.}$, which can be included separately. Our goal is to integrate the bath degrees of freedom and obtain the effective equation of motions for system-only degrees of freedom.

[1]Through this thesis we consider the bath with boson statistics.

The natural step is to switch to the interaction picture following the transformation

$$\hat{\rho}_I(t) = \exp\left[\frac{i}{\hbar}\left(\hat{H}_s + \hat{H}_b\right)t\right]\hat{\rho}_{\rm tot}(t)\exp\left[-\frac{i}{\hbar}\left(\hat{H}_s + \hat{H}_b\right)t\right] \tag{2.5}$$

where $\rho_{\rm tot}(t)$ is the total density matrix of system and environment, and $\hat{\rho}_I(t)$ is the density matrix in the interaction picture. The time evolution of the $\hat{\rho}_I(t)$ is given by the von Neumann equation

$$\frac{d}{dt}\hat{\rho}_I(t) = -\frac{i}{\hbar}[\hat{H}_{sb}(t), \hat{\rho}_I(t)] \tag{2.6}$$

where $\hat{H}_{sb}(t)$is similarly given by the transformation

$$\hat{H}_{sb}(t) = \exp\left[\frac{i}{\hbar}\left(\hat{H}_s + \hat{H}_b\right)t\right]\hat{H}_{sb}\exp\left[-\frac{i}{\hbar}\left(\hat{H}_s + \hat{H}_b\right)t\right] \tag{2.7}$$

In Eq. (2.5), one can take a trace over bath degrees of freedom. Since the system and the bath parts of the Hamiltonian act on different degrees of freedom, and they commute, $[\hat{H}_s, \hat{H}_b] = 0$, the reduced density matrix of the system reads

$$\hat{\rho}(t) = \exp\left[-\frac{i}{\hbar}\hat{H}_s t\right]\hat{\rho}(t)\exp\left[\frac{i}{\hbar}\hat{H}_{\rm s}\,t\right] \tag{2.8}$$

where

$$\hat{\rho}(t) \equiv {\rm Tr_b}\left\{\hat{\rho}_I(t)\right\}. \tag{2.9}$$

To proceed, we assume that at time $t = 0$, the system bath correlations are absent, and the total state can be written as a tensor product of density matrices of the system and bath

$$\hat{\rho}(0) = \hat{\rho}_b \otimes \hat{\rho}_s(0) \tag{2.10}$$

Additionally, here, the bath is assumed to be in the (thermal) equilibrium, and we neglect its evolution over time due to the weak coupling to the system. As such, we can further factorize the total density matrix and write

$$\hat{\rho}_I(t) = \hat{\rho}(t) \otimes \rho_B. \tag{2.11}$$

This is the **Born approximation**, which results from the assumption that the system-bath couplings λ_{ik} are much smaller than typical energy scales of H_s and H_b. This assumption ensures there are no macroscopic system-bath correlations established dynamically.

Now, one can integrate the von Naumann equation for the density matrix

$$\hat{\rho}_I(t) = \hat{\rho}_I(0) - \frac{i}{\hbar}\int_0^t \left[\hat{H}_{sb}(t'), \hat{\rho}_I(t')\right] dt'. \tag{2.12}$$

We substitute expression (2.12) instead of $\hat{\rho}_i(t')$, and neglect the commutator $[\hat{H}_{sb}(t'), \hat{\rho}_I(0)] = 0$. Differentiation of the obtained expression with respect to t gives

$$\dot{\hat{\rho}}_I(t) = -\frac{1}{\hbar^2}\int_0^t \left[\hat{H}_{sb}(t), \left[\hat{H}_{sb}(t'), \hat{\rho}_I(t')\right]\right] dt' \tag{2.13}$$

Now, one can trace over the bath degrees of freedom, which results in the following equation for the reduced system density matrix

$$\dot{\hat{\rho}}(t) = -\frac{1}{\hbar^2}\int_0^t \mathrm{Tr}_b \left[\hat{H}_{sb}(t), \left[\hat{H}_{sb}(t'), \hat{\rho}(t') \otimes \rho_B\right]\right] dt' \tag{2.14}$$

The expression under the integral takes the form $\lambda_{ik}\lambda_{jk'}\hat{L}_i(t)\hat{L}_j^\dagger(t')\rho(t')\mathrm{Tr}_B\{\hat{f}(t)\hat{f}_{k'}^\dagger(t')\hat{\rho}_b\} + \ldots$, where $\mathrm{Tr}_B\{\hat{f}(t)\hat{f}_{k'}(t')\hat{\rho}_b\}$ are nothing but the bath correlation functions. If the bath is in thermal equilibrium, we can assume that its correlation time τ_B is much shorter than other timescales of the problem related to the dynamics of the system. Saying that the system does not distinguish timescales of the bath (**Markov approximation**), the integrand of (2.14) gives a non-zero contribution only when $t \approx t'$. It allows us to push the upper integration limit to infinity.

$$\dot{\hat{\rho}}(t) = -\frac{1}{\hbar^2}\int_0^\infty \mathrm{Tr}_b \left[\hat{H}_{sb}(t), \left[\hat{H}_{sb}(t-\tau), \hat{\rho}(t-\tau \approx t) \otimes \rho_B\right]\right] d\tau \tag{2.15}$$

Operators $\hat{L}_i$ can be expressed as a linear combination of the eigenmodes of $\hat{H}_s$. In the simplest case, we consider $[\hat{H}_s, \hat{L}_i] = -\hbar\omega_i\hat{L}_i$. Then, in the interaction picture, the terms in (2.15) have a form

$$-\int_0^\infty d\tau \sum_{m,n} \hat{L}_m^\dagger \mathrm{e}^{i\omega_m t}\hat{L}_n^- \mathrm{e}^{-i\omega_n t}\rho\,(t-\tau)\,\mathrm{Tr_B}\left\{\mathrm{e}^{i\omega_n\tau}\sum_k \lambda_{m,k}^*\hat{f}_k(t)\sum_{k'}\lambda_{n,k'}\hat{f}_{k'}^\dagger\,(t-\tau)\,\hat{\rho}_b\right\} \tag{2.16}$$

In the atomic, molecular and optical physics (AMO) platform, ω_n are set by the external drive and are, as a rule, much faster than the dynamics of the system. The non-diagonal terms in the expression above ($m \neq n$) exhibit fast oscillations with the frequencies multiple of $(\omega_{n+1} - \omega_n)$, and, for evolution over timescale $t \gg 1/(\omega_{n+1} - \omega_n)$, average out. The diagonal terms with $m = n$, instead, do not have an oscillatory phase and give finite contributions at relevant timescales. As such, we apply **Rotating Wave Approximation (RWA)** and keep only terms with $\omega_n = \omega_m$. Finally, the integrals read

$$-\sum_m \hat{L}_m^\dagger\hat{L}_m^-\rho\,(t)\int_0^\infty d\tau\,\mathrm{Tr_B}\left\{\mathrm{e}^{\mathrm{i}\omega_m\tau}\sum_k \lambda_{m,k}^*\hat{f}_k(t)\sum_{k'}\lambda_{m,k'}\hat{f}_{k'}^\dagger\,(t-\tau)\,\hat{\rho}_b\right\} \tag{2.17}$$

The expression $\int_0^\infty d\tau\,\mathrm{Tr_B}\left\{\mathrm{e}^{\mathrm{i}\omega_m\tau}\sum_k \lambda_{m,k}^*\hat{f}_k(t)\sum_{k'}\lambda_{m,k'}\hat{f}_{k'}^\dagger\,(t-\tau)\,\hat{\rho}_b\right\}$ is nothing but the Fourier transform of the bath correlation functions, which contain imaginary part,

which results in the energy shifts [the effect which is, as a rule, hidden into the renormalization of the energy scales], and real part, which induces the dissipation. After combining all terms and some math, the resulting master equation reads

$$\begin{aligned}\dot{\hat{\rho}}(t) =& \sum_m \frac{1}{2}\gamma_m \left(2\hat{L}_m\hat{\rho}\hat{L}_m^\dagger - \{\hat{L}_m^\dagger\hat{L}_m, \hat{\rho}\}\right) \\ &+ \sum_m \frac{1}{2}\delta_m \left(2\hat{L}_m^\dagger\hat{\rho}\hat{L}_m - \{\hat{L}_m\hat{L}_m^\dagger, \hat{\rho}\}\right) \\ &- i\sum_m \left(A_m\hat{L}_m^\dagger\hat{L}_m + B_m\hat{L}_m\hat{L}_m^\dagger\right)\end{aligned} \tag{2.18}$$

The coefficients are given by the bath correlation functions and read

$$\begin{aligned}\int_0^\infty d\tau\, \mathrm{Tr_B}\left\{\mathrm{e}^{\mathrm{i}\omega_m\tau}\sum_k \lambda^*_{m,k}\hat{f}_k(\tau)\sum_{k'}\lambda_{m,k'}\hat{f}^\dagger_{k'}(0)\,\hat{\rho}_b\right\} =& \frac{1}{2}\gamma_m + iA_m \\ \int_0^\infty d\tau\, \mathrm{Tr_B}\left\{\mathrm{e}^{\mathrm{i}\omega_m\tau}\sum_k \lambda_{m,k}\hat{f}^\dagger_k(\tau)\sum_{k'}\lambda^*_{m,k'}\hat{f}_{k'}(0)\,\hat{\rho}_b\right\} =& \frac{1}{2}\delta_m + iB_m\end{aligned} \tag{2.19}$$

Note that the second line is non-zero only if the bath is not empty. It means that if the reservoir is at zero temperature, the master equation will contain only a first line of (2.18). Here, we include the energy shift A_m into the level splitting of the system.

2.2. Dicke model as a phenomenological tool to describe phase transition

In this Section, we consider the concept of superradiance and then study particular examples of the model, where it appears, and the underlying mechanism. We explore properties of the Dicke model: collective model with the discrete $\mathbb{Z}_2$ symmetry, spontaneous breaking of which results in the normal phase to the superradiance phase transition.

2.2.1. *Formulation of the problem*

The Dicke model was introduced in 1954 in the seminal work by R.H. Dicke[2] to describe the interaction of emitters – gas of molecules – with the quantized photon field. The

[2]The seminal work by Dicke was originally introduced in 1954 to describe the collective radiation of indistinguishable atoms with non-degenerate energy levels [65]. It studies the spontaneous emission of N inverted atoms and claims that if the spacing between atoms is a fraction of wavelength (negligible), the emission of light by different atoms is non-distinguishable, which results in the scaling of the emitted light intensity with the N^2 (when the half of the atoms are excited); for independent emitters, the intensity is rather $\propto N$.

corresponding Hamiltonian is given by

$$\hat{H} = \sum_{i=1}^{M} \omega_{c_i} \hat{a}_i^\dagger \hat{a}_i + \sum_{n=1}^{N} \omega_z \hat{\sigma}_n^z + \sum_{n,i} \frac{g_{in}}{\sqrt{N}} (\hat{a}_i \hat{\sigma}_n^+ + \hat{a}_i^\dagger \hat{\sigma}_n^-) + \sum_{n,i} \frac{g'_{in}}{\sqrt{N}} (\hat{a}_i \hat{\sigma}_n^- + \hat{a}_i^\dagger \hat{\sigma}_n^+). \quad (2.20)$$

Here, $\hat{a}_i$ is the annihilation operator of the photon with frequency ω_{ci}, ω_z is the level splitting of atoms, g_{in}, g'_{in} – are the photon-matter couplings, and σ_n^μ with $\mu = \{x, y, z\}$ are Pauli matrices with which we model two-level atoms. The commutation relations are $[\hat{\sigma}_i^\mu, \hat{\sigma}_j^\nu] = 2i\delta_{ij}\epsilon_{\mu\nu\lambda}\hat{\sigma}_i^\lambda$, $[\hat{a}_i, \hat{a}_j^\dagger] = \delta_{ij}$, $[\hat{a}_i, \hat{a}_j] = 0$, and we set the Plank constant equal to one for simplicity. In Ref. [65], such a model (with $g'_{in} = 0$) was used to describe the effect of emitting a single photon on a state of the atomic gas.

Later on [66, 67], the model (2.20) has been shown to feature a phase transition. For small couplings, the atoms are in the ground state and do not emit light. But the critical coupling exists, above which the cavity mode develops an occupation, which scales with the number of atoms. Such transition signals the establishment of coherences in the system, and as such, the phase adopted the name SR[3]. Such transition has been shown to exist for both $g'_{im} = 0$ and $g'_{im} = g^*_{im}$ with the only difference that in the former case, the critical coupling g_{im} is two times larger than in latter. Note that in this thesis, we concentrate on the scenario where spins interact with the single cavity mode, $M = 1$, and the coupling constant is homogeneous, $g_{in} = g'_{in} = g$, which gives the following model

$$\hat{H} = \omega_c \hat{a}^\dagger \hat{a} + \sum_{n=1}^{N} \omega_z \hat{\sigma}_n^z + \sum_{n} \frac{g}{\sqrt{N}} (\hat{a} + \hat{a}^\dagger) \hat{\sigma}_n^x \quad (2.21)$$

2.2.2. *Phase transition of the Dicke model*

2.2.2.1. *Closed system.* The transition reflects the spontaneous breaking of $\mathbb{Z}_2$ symmetry of the Hamiltonian (2.21) when the coupling g increases above the critical value g_c. The Dicke Hamiltonian is invariant under the transformation

$$(\hat{a}, \hat{\sigma}_n^x) \leftrightarrow (-\hat{a}, -\hat{\sigma}_n^x). \quad (2.22)$$

Above the critical point, two equilibrium solutions appear, and the system picks up one of them as a result of spontaneous symmetry breaking.

The critical point and the population of the cavity mode/spin magnetization can be evaluated in the thermodynamic limit by solving equations of motion. The equations

[3]According to R. H. Dicke, "*. . . a gas which is radiating strongly because of coherence will be called 'superradiant'*" [65]. Such definition resulted in some ambiguity, as by 'superradiance,' one can assume a correlated emission of indistinguishable atoms as well as the stationary state of the Dicke model.

of motion for arbitrary operator $\hat{A}$ are given by

$$\dot{\hat{A}} = i\left[\hat{H}, \hat{A}\right]. \tag{2.23}$$

We write dynamics for the photon field $\hat{a}$ and the spins $\hat{\sigma}_n$

$$\begin{aligned}
\dot{\hat{a}} &= -i\omega_c \hat{a} - i\sum_m \frac{g}{\sqrt{N}}\hat{\sigma}_m^x \\
\dot{\hat{\sigma}}_n^x &= 2i\omega_z \hat{\sigma}_n^y \\
\dot{\hat{\sigma}}_n^y &= -2i\omega_z \hat{\sigma}_n^x + \frac{2ig}{\sqrt{N}}(\hat{a} + \hat{a}^\dagger)\hat{\sigma}_n^z \\
\dot{\hat{\sigma}}_n^z &= -\frac{2ig}{\sqrt{N}}(\hat{a} + \hat{a}^\dagger)\hat{\sigma}_n^y.
\end{aligned} \tag{2.24}$$

The equilibrium solution can be obtained by setting time derivatives to zero and calculating expectation values, determined as $\langle \hat{O} \rangle = \mathrm{Tr}(\hat{O}\hat{\rho})$. The left-hand side of equations (2.24) is linear in spin and photon operators, but the right side contains a product of two operators, such as $\hat{a}\hat{\sigma}_n^z$. Taking the expectation values in these equations connects one and two-point correlation functions. Similarly, the equations for two-point correlations contain higher-order corrections. In order to solve the problem self-consistently, one needs to break this Bogoliubov-Born-Green-Kirkwood-Yvon (BBGKY) hierarchy by factorizing higher-order correlations, for instance, by neglecting connected part of the two-point correlations, $\langle \hat{a}\hat{\sigma}_n^z \rangle \approx \langle \hat{a} \rangle \langle \hat{\sigma}_n^z \rangle$. Neglecting two-point correlations, the description of the problem becomes mean field (MF), disregarding quantum fluctuations.

The mean-field limit for the Dicke model gives a reasonable solution when the number of atoms increases. The Dicke model is a collective model with the permutation symmetry of individual spins. The model can be formulated in terms of collective spins

$$\begin{aligned}
\hat{S}^x &= \frac{1}{2}\sum_{n=1}^{N} \hat{\sigma}_n^x \\
\hat{S}^y &= \frac{1}{2}\sum_{n=1}^{N} \hat{\sigma}_n^y \\
\hat{S}^x &= \frac{1}{2}\sum_{n=1}^{N} \hat{\sigma}_n^z
\end{aligned} \tag{2.25}$$

for which the following commutation relations hold holds

$$[\hat{S}^\mu, \hat{S}^\nu] = i\epsilon_{\mu\nu\lambda}\hat{S}^\lambda. \tag{2.26}$$

The magnitude of collective spins scales linearly with N, so in order to get rid of this parameter, it is worth studying the commutation relation for the normalized spins,

$\hat{s} = \hat{S}/N$. Dividing equation(2.26) by N^2 one gets

$$[\hat{s}^\mu, \hat{s}^\nu] = i\epsilon_{\mu\nu\lambda}\frac{1}{N}\hat{s}^\lambda. \tag{2.27}$$

and the factor $1/N$ is nothing but the effective Plank constant of the problem. In the thermodynamic limit, $N \to \infty$, the effective Plank constant becomes zero, and thus, the mean-field description is exact. In this thesis, we mostly solve numerically mean-field dynamics, including semi-classical description, via cumulants or phase-space methods to check the validity of the mean-field at different stages of the evolution.

We proceed with the MF solution of the Dicke model. Below, we denote one-point observables by the same letters without the ' ^ ' symbol. We also use permutation invariance of the spins, omitting the spin position indices. A non-trivial SR equilibrium solution is given by

$$\begin{aligned} a &= \mp\frac{g\sqrt{N}}{\omega_c}\sqrt{1-\frac{g_c^4}{g^4}} \\ \sigma^x &= \pm\sqrt{1-\frac{g_c^4}{g^4}} \\ \sigma^y &= 0 \\ \sigma^z &= -\frac{g_c^2}{g^2}, \end{aligned} \tag{2.28}$$

when the coupling is above the critical

$$g_c = \sqrt{\frac{\omega_z\omega_c}{2}}. \tag{2.29}$$

The alternating signs $\pm$ in (2.28) correspond to two degenerate solutions, mimicking the original $\mathbb{Z}_2$ symmetry of the Dicke model.

The novel experimental implementations operate with $N = 10^4 - 10^5$ particles, guaranteeing that, at least at short times, the dynamics remain mean-field as long as initial spins are prepared in a spin coherent state. A common initial state in the experiment is when all atoms are in the normal (spin-down) state.

2.2.2.2. *Open system.* In this work, we concentrate on the AMO platform and the implementation of the model via cavity QED setup, where spins model atomic degrees of freedom and the photon is a photon mode of the Fabry-Perot cavity. The cavity mode has a finite linewidth due to the non-zero transparency of the mirrors. This finite linewidth results in the dissipation of the cavity mode. The steady state of the Dicke model in the presence of the various sources of dissipation has been carefully revised in the Refs. [68–71].

The analysis is simple to the previous case, with the only difference that the dynamics not is given by the Lindblad master equation (2.1), modifying the dynamics of the cavity

field accordingly and read

$$\dot{\hat{a}} = -i\omega_c \hat{a} - i \sum_m \frac{g}{\sqrt{N}} \hat{\sigma}_m^x - \frac{\kappa}{2} \hat{a}. \tag{2.30}$$

The mean-field stationary state then

$$\begin{aligned} a &= \mp \frac{g\sqrt{N}}{\omega_c - i\kappa/2} \sqrt{1 - \frac{g_c^4}{g^4}} \\ \sigma^x &= \pm \sqrt{1 - \frac{g_c^4}{g^4}} \\ \sigma^y &= 0 \\ \sigma^z &= -\frac{g_c^2}{g^2}, \end{aligned} \tag{2.31}$$

with the critical coupling

$$g_c = \sqrt{\frac{\omega_z(\omega_c^2 + \kappa^2/4)}{2\omega_c}} \tag{2.32}$$

which converges to the equilibrium solution when the decay rate κ goes to zero.

As one can see, by adding dissipation to the system, the SR phase still exists, but for higher critical couplings. The SR phase is stabilized by the balance of driving and losses. Another important aspect is that adding cavity loss makes the cavity field acquire complex phase $\arg(a) = \arctan(\kappa/\omega_c)$. This effect was utilized in [72, 73] to trigger the periodic oscillation of the photon phase in the self-organization dissipative process.

When studying quench dynamics, preparing the system in the ground state and abruptly turning on the coupling $g > g_c$, the systems exhibit non-equilibrium early-time behavior, with the dynamical instability at the beginning (cavity field starts grove exponentially up to the value $\propto \sqrt{N}$), oscillatory behavior, and then relaxation towards the steady state as the excess of energy can be released through the cavity decay.

The different aspects of phase transitions in the open Dicke model have been summarized in the review [71], including the properties in thermal equilibrium, response to different dissipation channels (spin loss, which preserves the phase transition and spin dephasing, which washes it out), and scaling behavior.

2.3. Phase transition in the driven-dissipative Tavis-Cummings model

In this section, we discuss the phase transition in the Tavis-Cummings model for closed and open systems. The model possesses $U(1)$ symmetry and is commonly used to describe the lasing transition. These preliminaries are used in publication [1].

For completeness, here we consider a dissipative transition generated by the breaking of the continuous $U(1)$ symmetry. The corresponding model can be derived from the Dicke model via RWA, disregarding co-rotating terms in the interaction, $(\hat{a}\hat{\sigma}_n^- + \hat{a}^\dagger\hat{\sigma}_n^+)$. The Hamiltonian reads

$$\hat{H} = \omega_c \hat{a}^\dagger \hat{a} + \sum_{n=1}^{N} \omega_z \hat{\sigma}_n^z + \sum_n \frac{g}{\sqrt{N}}(\hat{a}\hat{\sigma}_n^+ + \hat{a}^\dagger\hat{\sigma}_n^-) \tag{2.33}$$

In equilibrium, for small couplings, the system remains in the normal state. If the coupling is strong enough, another solution of the form $\sigma^\pm = e^{\pm i\omega t}\sigma_0^\pm$, $a = a_0 e^{-i\omega t}$ arises, when couplings $g \geq \sqrt{2(\omega_c - \omega)(\omega_z - \omega)}$. The formal lasing solution reads $\sigma^z = -2(\omega_z - \omega)(\omega_c - \omega)/g^2$, $\sigma_0^- = \sqrt{1 - \sigma_z^2}/2$ and $a_0 = -g\sqrt{N}/(\omega_c - \omega)\sigma_0^-$. However, this solution becomes unstable at finite temperature $T \neq 0$, and any practical realizations of lasing require a pump to induce population inversion.

The $U(1)$ symmetry results in the conservation of the excitation number in the model, and when dissipations are added, the loss of the excitation to the environment cannot be balanced by the interaction. The non-trivial solution can be stabilized by adding external driving. In this thesis (cf. Ref. [1]), we study dynamics given by the Lindblad master equation [74, 75]

$$\dot{\hat{\rho}} = -i[\hat{H}, \hat{\rho}] + \kappa\mathcal{D}[\hat{a}] + \gamma_\downarrow \sum_{i=1}^{N} \mathcal{D}[\hat{\sigma}_i^-] + \gamma_\uparrow \sum_{i=1}^{N} \mathcal{D}[\hat{\sigma}_i^+] \tag{2.34}$$

where we accounted for cavity loss, incoherent loss, and pump with the rates κ, $\gamma_\downarrow$, $\gamma_\uparrow$ respectively. To find the lasing solution, we again switch to the rotating frame, using the same ansatz $\sigma^\pm = e^{\pm i\omega t}\sigma_0^\pm$, $a = a_0 e^{-i\omega t}$. The equations of motion read

$$\begin{aligned}
\dot{a}_0 &= -i(\omega_c - \omega)a_0 - ig\sqrt{N}\sigma_0^- - \frac{\kappa}{2}a_0 \\
\dot{\sigma}_0^- &= -i(2\omega_z - \omega)\sigma_0^- + i\frac{g}{\sqrt{N}}a_0\sigma_z - \frac{\gamma_\uparrow + \gamma_\downarrow}{2}\sigma_0^- \\
\dot{\sigma}^z &= (\gamma_\uparrow - \gamma_\downarrow) - (\gamma_\uparrow + \gamma_\downarrow)\sigma^z + \frac{2ig}{\sqrt{N}}(-a\sigma_0^+ + a_0^*\sigma_0^-).
\end{aligned} \tag{2.35}$$

We find the stationary solution by setting the right-hand side equal to zero. The non-trivial solution reads $\omega = \frac{2\omega_z\kappa + \omega_c\gamma_t}{\kappa + \gamma_t}$, where $\gamma_t = \gamma_\uparrow + \gamma_\downarrow$, $\sigma^z = \frac{\gamma_t[(\omega_c - \omega)^2 + \kappa^2/4]}{g^2\kappa}$, $\sigma_0^- = \sqrt{\frac{\gamma_t[(\omega_c - \omega)^2 + \kappa^2/4]}{2g^2}(\sigma^z - \sigma_0^z)}$, where we denote the magnetization for non-interacting

system $\sigma_0^z = \frac{\gamma_\uparrow - \gamma_\downarrow}{\gamma_t}$, and $a_0 = -\frac{g\sqrt{N}}{(\omega_c - \omega) - i\kappa/2}\sigma_0^-$. The lasing solution appears when the system is pumped into a population inverted state with $\gamma_\uparrow > \gamma_\downarrow$ for small photon decay rates.

2.4. Essentials of implementation of the Dicke model in laser-driven BEC in a high-finesse cavity

In this section, we briefly discuss the main idea behind the implementation of the Dicke model in the cavity QED platform, such as the main advantages and principles behind the the coupling of light and matter. And the same time, here I omit the technical derivation and refer to the Appendix of publication [2] instead.

In this thesis, we study models relevant to the light-matter interfaces, where photons strongly interact with the matter, which can be represented by atoms, quantum dots, nitrogen-vacancy (NV) defects in solids, etc. We are particularly concentrated on a cavity QED platform, which describes atoms trapped in the cavity [30, 75, 76]. The development of the cavity QED field takes its origin in the work by Purcell on the cavity-enhanced spontaneous emission of a spin in magnetic resonance [77][4]. Further development includes the realization of the Rabi oscillations via coherent coupling of the excited and ground atomic states [75] and the illustration of the photon-matter coupling with the level repulsion [75, 78]. With the realization of the BEC [79, 80], enabling the creation of a coherent state of a large number of atoms, an important direction nowadays is to use cavity QED as an analogous quantum simulator for the implementation of different models featuring emergent self-organization transitions. By changing geometry, pumping scheme, number of atoms, applying magnetic fields, etc., the cavity QED platform allows the simulation of such models as a Dicke model [33, 72, 81, 82]; generalized Hubbard models [43, 83, 84], emulate spatial disorder of couplings in the Dicke model [30, 85–87]. It also serves as a platform for realizing a supersolid state [44, 45], different magnetic structures [88, 89], etc. The main ingredients there are atoms, whose degrees of freedom mimic two-level systems, and a cavity field, which mediates the interaction between them.

There are two main challenges to realizing emergent self-organization transition like in the Dicke model [90]. The first one is to realize a regime when coupling overcomes the spontaneous decay of two-level atoms. This can be achieved by working far from resonances with the excited states, following a three (four) level scheme. In this case, the transition occurs between two stable low-energy states, and one can neglect spontaneous

[4]The decay rate can change both ways, increase or degrees, depending on the photon-matter coupling and the finesse of the cavity [75].

emission. The second challenge is the strong photon-matter coupling [75]. In the non-relativistic regime, the light-matter interaction originates from the kinetic term [46]

$$\hat{H}_{ca} = \frac{1}{2m}\left(\hat{\mathbf{p}} - e\hat{\mathbf{A}}\right)^2,$$

with $\mathbf{p}$, e m being momentum, charge, and mass of the atom, and $\mathbf{A}$ vector potential of the electromagnetic field. Neglecting multi-photon processes and using dipole approximation (neglecting the size of the atom compared to the photon wavelength), the interaction reeds $\hat{H}_{ca} = -\frac{e}{m}\hat{\mathbf{A}}\hat{\mathbf{p}} \approx -\hat{\mathbf{d}}\hat{\mathbf{E}}$, where $\hat{\mathbf{d}}$ is the dipole operator. This dipole coupling in the free space is much lower than the level splitting and cavity frequency, and thus, for the Dicke model, the coupling is well below the critical value. Loading atoms in a cavity one, first, enhances photon-matter coupling, $\mathbf{A} \propto 1/\sqrt{V}$ with V – volume, and also, if the mirrors of the cavity have very low transparency (high-finesse cavities) the photon, emitted by one atom, travels through the cavity many times increasing the possibility to be reabsorbed by another atom (another leaver here is the number of atoms N: the more atoms, the more scattering centers and the higher the probability to be reabsorbed). When the photon-matter coupling is above the critical value, the cavity mode induces coherent interaction between atoms, leading to the self-organization SR transition.

The experimental implementation of the Dicke model has been done in [33] and [81, 82] by applying Bragg or Raman[5] driving schemes. In the Brag scheme, one considers a combination of the classical laser and cavity mode such that they induce internal-spin preserving atomic transition, and the effective two-level system is built from motional states of the atoms, the ground state $|0\rangle = |k_x = 0, k_z = 0\rangle$, and the excited $|1\rangle = |k_x = \pm k, k_z = \pm k\rangle$ (the internal state of the atom is not altered). The second implementation acquires a spin-changing process, in which the two-level system is built from combined spin and motional states, $|0\rangle = |k_x = 0, k_z = 0\rangle \otimes |\downarrow\rangle$, $|1\rangle = |k_x = \pm k, k_z = \pm k\rangle \otimes |\uparrow\rangle$. These two implementations are effectively described by the same Hamiltonians, although on the macroscopic level, transitions manifest differently: in the first case, the population of the excited momentum state corresponds to the spatial modulation of the condensate density (formation of the so-called checkerboard lattices), while in the second case, the system simultaneously acquires the density modulation dressed with the spin checkerboard lattice (as we show in this thesis, interesting observable effects appear when both these implementations are combined, since through the interdependence of the different degrees of freedom the non-stationary phases appear, extending the available dynamical regimes of the Dicke models). Both implementations have a dissipation of the photons because of the non-zero transparency

[5]The theoretical proposal of the experimental implementation by Dimer et al. [90] also dealt with Raman driving scheme.

of the cavity mirrors and coupling to the environment. The detailed experimental implementation of the Dicke model in both cases is given in the appendix of publication [2].

2.5. Atom-only description

Here, we briefly discuss the adiabatic elimination of the cavity field, which simplifies the description. The procedure results in the dissipative spin model, lowering the number of relevant degrees of freedom.

The cavity QED implementation of the Dicke model usually operates with the cavity mode detuning ω_c and decay rate κ, which are at least two orders of magnitude larger than the effective photon-matter coupling and atomic level splitting. It results in a significant difference between atomic and photon timescales. In practice, it means that when the system is driven from the normal state to the SR, there is a longer timescale associated with the relaxation of atoms and a much shorter timescale over which the photon number oscillates around some time-averaged value. These oscillations do not bring much information and are irrelevant for the steady state properties, yet numerically, they limit computation ability, setting an upper bound on a time step (which must be much smaller than $2\pi\omega_c$). Fortunately, one can eliminate the fast oscillating mode and solve the atom-only model, which contains only low-energy (long times) eigenstates of the Liuvillian [91–93].

With the adiabatic elimination technique, we do not distinguish fast processes that appear on the timescales $\propto 1/\omega_c$, but we study coarse-grained dynamics with the larger timescale. The slowest modes govern the equilibrium, so this assumption generates fewer errors for longer timescales.

Lets consider a formal procedure of the adiabatic elimination on the example of the dissipative Dicke model. The dynamics of the cavity photon are given by[6]

$$\dot{a} = (-i\omega_c - \kappa)a - ig\sqrt{N}\sigma^x. \tag{2.36}$$

With the Laplace transformation, the formal solution reads

$$a(t) = a(0)e^{-(\kappa+i\omega_c)t} - ig\sqrt{N}\int_0^t d\tau e^{-(\kappa+i\omega_c)\tau}\sigma^x(t-\tau) \tag{2.37}$$

Expanding $\sigma^x(t-\tau)$ in Taylor series around t gives

$$a(t) = -ig\sqrt{N}\left[\frac{\sigma^x(t)}{\kappa+i\omega_c} - \frac{\dot{\sigma}^x(t)}{(\kappa+i\omega_c)^2} + \dots\right] + \dots \tag{2.38}$$

[6]Here, we substitute the photon decay rate equal to 2κ to avoid the extra factor 2 in the following denominators.

The last ... include terms $\propto t^n e^{-(\kappa+i\omega_c)t}$, $n = 0, \ldots, \infty$, which are zero for time scales $t \gg \omega_c, \kappa$. Neglecting time derivative contributions, one obtains

$$a(t) = -ig\sqrt{N}\frac{\sigma^x(t)}{\kappa + i\omega_c}. \tag{2.39}$$

First, this expression shows the connection between photon and matter observables in a cavity QED, and it is at the heart of the indirect measurement techniques for this platform. Second, the expression becomes exact in the steady state.

However, this expression does not describe the relaxation towards equilibrium of the Dicke model. To show that, we recall the result on the operator level,

$$\hat{a} = \frac{-ig}{\sqrt{N}}\sum_n \frac{\hat{\sigma}_n^- + \hat{\sigma}_n^+}{\kappa + i\omega_c} + \ldots \tag{2.40}$$

where we also substitute $\hat{\sigma}_n^x = \hat{\sigma}_n^- + \hat{\sigma}_n^+$. Then one can consider the change of the energy of the system, $\frac{\partial E}{\partial t} = \frac{\kappa}{2}\left(2\hat{a}^\dagger \hat{H} a - \left\{\hat{a}^\dagger a, \hat{H}\right\}\right)$. Substitution expression for $\hat{a}$ into the Hamiltonian and jump operator in the dissipator, one can find that contribution from σ_n^- and σ_n^+ cancel each other, and the energy is conserved in the leading order. Thus, higher-order corrections are needed to obtain relaxation toward the steady state. The next order correction results from substituting the expression for $\dot{\sigma}^x$ from (2.30)

$$\hat{a} = -i\frac{g}{\sqrt{N}}\sum_n \left[\frac{\hat{\sigma}_n^x}{\kappa + i\omega_c} - \frac{2i\omega_z \hat{\sigma}_n^y}{(\kappa + i\omega_c)^2} + \ldots\right] + \ldots \tag{2.41}$$

The second term above encounters corrections (in $\omega_z/(\omega_c - i\kappa)$) that are responsible for emitting energy to the environment and relaxing towards the correct steady state.

The elimination of the fast modes can also be done in different ways. In [91], authors describe the elimination of boson modes through the Schrieffer-Wolf approximation (cf. Ref. [94] for a quick tutorial). According to a method, one determines the transformation that allows the decoupling of spin and boson modes, and then one switches to the rotating frame of the bosons, neglecting self-consistently time-dependent terms in the effective Hamiltonian. This formalism (and also one in [92]) can be easier to derive and apply in practice. Also, in [91], authors verify that their adiabatic elimination preserves the positivity of the Lindbladian (i.e., it is trace-preserving, and no non-physical solutions are generated during dynamics), a statement not obvious from the naive integration out of fast oscillating exponents above.

In this thesis, we take advantage of the adiabatic elimination in some discussion of paper I and when evaluating long-time dynamics in work II. It also encourages us to consider dissipative spin models in Chapter 5

CHAPTER 3

Bridging quantum optics and spintronics: driven-dissipative Dicke phase transition in the presence of spintronics pumping

In this chapter, I present publication I [1] in which we have studied dynamical phase transitions in the driven-dissipative model featuring the main properties of magnet-metal heterostructure in spintronics or driven cold atoms in a cavity. Precisely, we consider a minimal model that contains ingredients based on symmetry and driving terms of the former.

This project has been motivated by the theory and experimental works on the realization of magnon condensation in spintronics. Precisely, we consider a setup in which the condensation of the magnons is triggered through the electric current in the adjacent metal layer [95]. The idea behind this is that electrons, driven by the electromagnetic potential, scatter against the boundary of the metal via spin flip, and the spin difference is transferred to the magnet in the form of a magnon. As such, there is a spin density transfer to the magnet sample. When the spin transfer is sufficient and overcomes Gilbert damping, the magnon condensate can be formed.

The essential ingredients of the setup are the following. The magnons in the magnet part of the heterostructure are described via the two-fluid theory, namely, distinguishing thermal short-wavelength magnons and magnon condensate [96]. Both thermal and condensed magnons interact with the spins accumulated on the boundary of the metallic sample. The spin accumulation is externally driven by an electric current through the metal sample by the spin Hall effect. Such a process can be modeled by adding two kinds of terms to the Lindblad master equation: spin pump and spin loss, and the strength of these processes is controlled by chemical potential and temperature. We consider the interaction of the magnons and accumulated spins to be $U(1)$ symmetric. Additionally, thermal and condensed magnons also can interact with each other. We model such interaction with the $\mathbb{Z}_2$ symmetric term, mimicking the anisotropy within the magnetic sample. Finally, we include the dissipation to the magnon condensate, featuring Gilbert damping.

Such a minimal model finds implementation in the cavity QED platform. Precisely, one can consider a Dicke model, describing the interaction of the different kinds of 'magnons', where cavity field a and spin $\mathcal{S}$ mimic the magnon condensate and thermal magnons, respectively. Both of them are coupled to another spin species $\mathcal{T}$, which is

Parameters	Thesis	Publication I
Dicke Coupling	g	λ
Tavis-Cummings coupling	g	η
Spin operator	Pauli matrix	Half of the Pauli matrix
Collective spin	$\hat{S}$	$\mathcal{S}$, $\mathcal{T}$
Observable	O	$\langle O \rangle$

TABLE 3.1. Notation difference between this thesis and publication I.

subjected to the 'reservoir' which induces spin pump and loss (such mechanism of spin pumping in the cavity QED setup has been considered in [74]). In the cavity QED setup, most of the parameters can be tuned sufficiently easily (as a rule, by varying the intensity of the external driving fields or by changing the detunings), which allows a high degree of control and explore different dynamical regimes of the model.

We show that such a model exhibits a rich phase diagram that originates from the breaking of corresponding symmetries of the model. In particular, it contains a stationary superradiant state, which mimics the formation of the magnon condensate, and a non-stationary phase, which we call lasing (or swasing from the solid-state physics perspective.)

Publication I also concludes the observation of the polaritons due to the coupling between atoms and photons (magnon condensate and thermal magnons) with different relaxation rates. First, this result confirms the hybridization of atom-cavity modes due to the interaction; second, the different lifetimes of these modes allow us to describe the dynamics at early and late time scales, from the dynamical instabilities at the beginning of the dynamics to the relaxation towards the attractor at late times.

Status of the publication: This article was published in September 2023 in Physical Review B as a regular article.

Note: Due to a mismatch between the notation used in different publications and this thesis, I would like to improve the readability of the publication by listing the notation changes in table 3.1.

Intertwining of lasing and superradiance under spintronic pumping

Oksana Chelpanova,[1] Alessio Lerose,[2] Shu Zhang,[3,4] Iacopo Carusotto,[5] Yaroslav Tserkovnyak,[4] and Jamir Marino[1,6]

[1]*Institut für Physik, Johannes Gutenberg Universität Mainz, D-55099 Mainz, Germany*
[2]*Department of Theoretical Physics, University of Geneva, Quai Ernest-Ansermet 30, 1205 Geneva, Switzerland*
[3]*Max-Planck-Institut für Physik komplexer Systeme, 01187 Dresden, Germany*
[4]*Department of Physics and Astronomy and Bhaumik Institute for Theoretical Physics, University of California, Los Angeles, California 90095, USA*
[5]*INO-CNR BEC Center and Dipartimento di Fisica, Università di Trento, 38123 Trento, Italy*
[6]*Kavli Institute for Theoretical Physics, University of California, Santa Barbara, California 93106, USA*

(Received 22 December 2021; revised 12 April 2022; accepted 26 July 2023; published 5 September 2023)

We introduce a quantum optics platform featuring the minimal ingredients for the description of a spintronically pumped magnon condensate, which we use to promote driven-dissipative phase transitions in the context of spintronics. We consider a Dicke model weakly coupled to an out-of-equilibrium bath with a tunable spin accumulation. The latter is pumped incoherently in a fashion reminiscent of experiments with magnet-metal heterostructures. The core of our analysis is the emergence of a hybrid lasing-superradiant regime that does not take place in an ordinary pumped Dicke spin ensemble, and which can be traced back to the spintronics pumping scheme. We interpret the resulting nonequilibrium phase diagram from both a quantum optics and a spintronics standpoint, supplying a conceptual bridge between the two fields. The outreach of our results concern dynamical control in magnon condensates and frequency-dependent gain media in quantum optics.

DOI: 10.1103/PhysRevB.108.104302

I. INTRODUCTION

The theme of dynamical phase transitions enabled by the interplay of interactions, drive, and dissipation permeates different branches of quantum many-body physics, such as quantum optics [1,2], cold atoms [3,4], and nonequilibrium solid-state physics [5–7]. The interest in them ranges from practical applications in dynamical control to the fundamentals of statistical mechanics. The exploration and understanding of nonequilibrium phases would benefit from a unifying language, which, however, remains elusive due to the diversity of microscopic ingredients, relevant scales, and engineering capabilities across the various platforms.

In this paper, we take the first step in filling this gap by studying a bare-bones model that offers complementary interpretations pertinent to both spintronics and driven-dissipative quantum optics, as illustrated in Fig. 1(a). The model is inspired by typical considerations in spintronics and cavity quantum electrodynamics (QED) systems and contains the ingredients that can be implemented in both platforms. We construct the model by coupling a coherent subsystem to an incoherent one through weak $U(1)$ symmetric interactions—the former is a Dicke model featuring a $\mathbb{Z}_2$ symmetric interaction between a spin ensemble and a boson mode, while the latter is a spin ensemble that can be externally driven into a given population state. The coherent subsystem is thus indirectly pumped.

As we will show, the interplay between the spin pumping and the Dicke coupling opens a parameter space where the lasing phase, which corresponds to the breaking of $U(1)$ symmetry, and the superradiant (SR) phase, which corresponds to breaking of $\mathbb{Z}_2$ symmetry, intertwine and lead to dynamical regimes exhibiting features of both. From the spintronics point of view, this implies the possibility of magnon lasing in a system with strongly broken $U(1)$ symmetry. From the quantum optics perspective, the model proposes an indirect pumping scheme which can lead to unconventional dynamical phases. In particular, a dynamical phase emerges with intertwined lasing and superradiance features, which results from a pumping scheme inspired by spintronics while also realizable in a quantum many-body optics platform. We argue that the nontrivial implications of our model in both fields can provide a conceptual bridge between the two communities.

A. Structure of the paper

The paper is organized as follows. First, we motivate this study from the separate cavity QED and spintronics backgrounds. We highlight the additional ingredients and briefly examine their effects on the conventionally expected dynamics in both setups. In Sec. II, we discuss the minimal model that captures these ingredients and draw parallels between implementations in the two setups. We also discuss the known limits of the resulting model. In Sec. III, we solve the dynamics of the model in the mean-field approximation and discuss the dynamical phase diagram, remarking on the symmetry breaking in different dynamical phases of the model. Finally, in Sec. IV we discuss the mechanism to generate unique dynamical phases and how they can be controlled via external drive. We conclude in Sec. V by discussing further developments of the model in light of recent advancements in the control of the cavity QED and spintronics platforms.

B. Cavity QED background and context

Cavity QED is a field of study that focuses on the interaction between light and matter at the quantum level. Over

 ©2023 American Physical Society

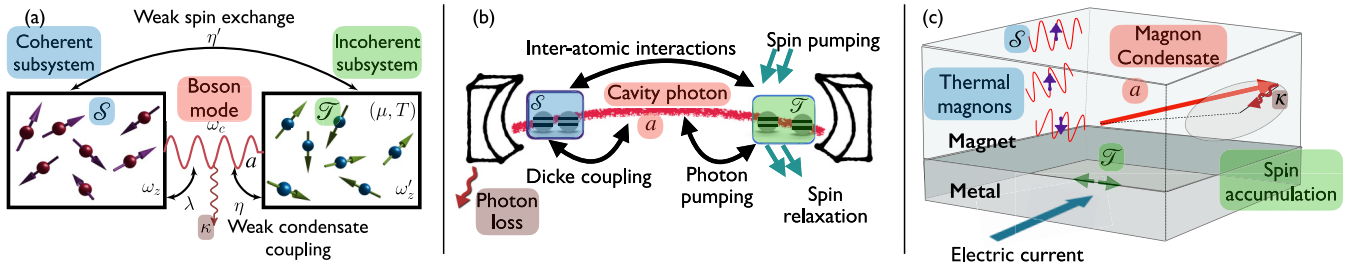

FIG. 1. (a) An ensemble of spins-1/2 $\mathcal{S}$ (in blue) is coupled to a boson mode (in red) which models a magnon condensate or a cavity boson which can become macroscopically occupied for large values of the Dicke coupling, λ. It is also coupled to a spin-1/2 subsystem $\mathcal{T}$ (in green) under incoherent spin relaxation and pumping controlled by the spin accumulation μ and temperature T. The population inversion of $\mathcal{T}$ can induce a coherent dynamical response in $\mathcal{S}$, which is the central mechanism explored in this paper. Dissipation with strength κ (in brown) acts on the boson mode and is shown by a red wiggle line. The model contains the essential ingredients of both quantum optics (b) and spintronics (c) platforms, as detailed in the main text. Corresponding elements in different setups are highlighted in the same color.

the years, multiple platforms have been proposed and realized as quantum simulators for exploring exotic models and developing desired phases of matter [8–11]. Specifically, by combining multiple driving fields, few cavity modes, and separating particles in a cavity via tweezers, exotic spin-spin interactions can be realized in cavity QED experiments [10,12] as well as nonlocal dissipation that leads to more efficient control over quantum correlations [13–15]. Furthermore, different experiments have varying system sizes, ranging from a few atoms per cavity, which require a complete quantum mechanical treatment, to hundreds of thousands of particles per cavity, which can be treated classically [16–18]. All these factors make cavity QED setups highly flexible and promising candidates for realizing various driven-dissipative models.

In this paper, we introduce a schematic model that well captures the dynamical features of the setup depicted in Fig. 1(b). We consider an optical cavity where two species of two-level atoms, $\mathcal{S}$ and $\mathcal{T}$, are coupled to each other as well as to a common lossy cavity mode. The ensemble $\mathcal{S}$ collectively couples to the cavity photon via a $\mathbb{Z}_2$ symmetric term as in the Dicke model, while the ensemble $\mathcal{T}$ is incoherently pumped and couples to the same photon mode via a spin-boson interconversion $U(1)$ symmetric term as in a Tavis-Cummings model. Combining these two models together brings us to the dynamical phase which hybridly inherits properties of both stationary and nonstationary phases.

Experimentally engineering photon-matter interaction with one spin species and one cavity mode is nowadays at its state of the art [9]. While combining two spin species may be challenging, the first steps have been taken, such as considering multicomponent BECs in a cavity [19–21] or building an effective spin representation based on different degrees of freedom, for example, momentum spin states and internal spin states [22,23].

C. Spintronics background and context

Our motivation to separate the coherent ($\mathcal{S}$) and incoherent ($\mathcal{T}$) spin subsystems stems from a solid-state viewpoint, to allow quantum correlations to settle in without much disruption from direct pumping processes. Considering magnet-metal heterostructures [24–32] as a primary example, the magnet layer has a stiff order parameter accompanied by coherent excitations [33], while itinerant electrons carrying incoherent spins in the metal layer are more amenable to external control [34]. One of the consequences of the magnet being a strongly interacting system is the propensity of a long-wavelength magnon to undergo (Bose-Einstein) condensation [35–37], which is mimicked by the boson mode in our model. In a magnet, such condensation can manifest as a static phase transition [38] or a dynamical one with the magnetic order parameter precessing spontaneously [39–41], bearing analogy to the SR and lasing transitions, respectively. As shown in Fig. 1(c), a magnon condensation can be triggered by electrically pumping the heterostructure [42–46]. A spin accumulation is induced via the spin Hall effect in the metal [47–52] and exerts a spin torque [53–55] on the magnetic dynamics by interfacial magnon-electron scatterings. Such a torque can overcome the intrinsic magnon decay and maintain a quasiequilibrium condensate of magnons. In addition, the magnon condensate and the thermally occupied short-wavelength magnons undergo coupled dynamics, previously described by a two-fluid theory [56]. Our model, though much simplified from this practical scenario, allows for a full treatment of the interplay of spin pumping, coupling between the interacting magnetic excitations and the pumped reservoir, and dissipative effects.

We remark that the model considered in this paper should not be regarded as an *ab initio* description of the spintronic setup depicted in Fig. 1(c), rather it captures the key conceptual elements, especially from a symmetry point of view. To give more details, the interactions between long-wavelength a and short-wavelength $\mathcal{S}$ magnons in magnets are likely to involve higher-order terms in the spin operators, while here it is set to be a $\mathbb{Z}_2$ symmetric interaction, which can be an oversimplification. On the other hand, from the symmetries point of view, $\mathbb{Z}_2$-type of $U(1)$ breaking commonly exists in magnetic materials, for example, due to crystalline anisotropy, and a Dicke term gives the desired symmetry. This induces ellipticity in magnon lasing, where the spontaneous precession of the magnon condensate is noncircular due to an oscillating magnitude. As we will show, a interesting form of magnon lasing, more dramatic than ellipticity, may arise when the $U(1)$ breaking term is sufficiently strong.

II. MODEL

The minimal model that captures the cavity QED setup in Fig. 1(b) and metal-magnet heterostructure in Fig. 1(c) is given in Fig. 1(a). Here we consider a Dicke sample [57–61], which consists of an ensemble $\mathcal{S}$ of N spin-1/2's collectively coupled to a boson mode a of frequency ω_c, weakly interacting with an ensemble $\mathcal{T}$ of an additional set of N spins. The level splitting of spins in subsystem $\mathcal{S}$ ($\mathcal{T}$) is ω_z (ω_z'). The full Hamiltonian reads

$$H = \omega_c a^\dagger a + \omega_z \mathcal{S}^z + \omega_z' \mathcal{T}^z + \frac{\lambda}{\sqrt{N}}(a + a^\dagger)(\mathcal{S}^+ + \mathcal{S}^-) + \frac{\eta}{\sqrt{N}}(a\mathcal{T}^+ + a^\dagger \mathcal{T}^-) + \frac{\eta'}{N}(\mathcal{S}^+\mathcal{T}^- + \mathcal{S}^-\mathcal{T}^+), \quad (1)$$

where a and $a^\dagger$ are boson annihilation and creation operators mimicking the magnon condensate or the cavity photon, while the collective spin operators $\mathcal{S}^- = \sum_{i=1}^N \sigma_i^-$ and $\mathcal{T}^- = \sum_{i=1}^N \tau_i^-$ describe two various spin species in a cavity QED setup or thermal magnons and spins of conducting electrons in magnet-metal heterostructure. Here σ_i^α and τ_i^α with $\alpha = x, y, z$ are spin-1/2 operators and $\sigma^\pm = (\sigma^x \pm i\sigma^y)$. Here, we have introduced the Dicke coupling λ, a small boson-spin interconversion term η, and a small spin exchange coupling η', the latter two quantifying the strength of $U(1)$ symmetric interactions between the spin ensemble $\mathcal{T}$ with the boson mode a and spin ensemble $\mathcal{S}$, respectively. All couplings are normalized such that every term in the Hamiltonian Eq. (1) scales linearly with the system size N.

The pumping and dissipative effects are described by the following Lindblad master equation [62] for the joint density matrix of the total system:

$$\frac{d\rho}{dt} = -i[H, \rho] + \kappa \mathcal{D}[a] + \gamma_\uparrow \sum_{i=1}^N \mathcal{D}[\tau_i^+] + \gamma_\downarrow \sum_{i=1}^N \mathcal{D}[\tau_i^-]. \quad (2)$$

Here, the dissipators $\mathcal{D}[x] \equiv x\rho x^\dagger - 1/2\{x^\dagger x, \rho\}$ are defined as usual. The ensemble $\mathcal{T}$ is driven incoherently and, in the steady state of the Lindblad, reaches a grand canonical state parameterized by temperature T and spin accumulation μ as a result of the spin pump and loss rates $\gamma_\uparrow = \gamma_t/[1 + e^{\beta(\omega_z' - \mu)}]$ and $\gamma_\downarrow = \gamma_t/[1 + e^{-\beta(\omega_z' - \mu)}]$, where $\beta = T^{-1} > 0$ and $\gamma_t = \gamma_\uparrow + \gamma_\downarrow \geqslant 0$. In Eq. (2), we have neglected spin dephasing effects [57]. In cavity QED, the Lindbladian (2) models spin pumping, used to induce the lasing phase [60,63], while in spintronics it mimics the fact that the spin accumulation between metal and magnet layers in Fig. 1(c) results from the spin Hall effect and, thus, can be controlled by changing the current in the metal layer [47–52]. When $\mu > \omega_z'$, the incoherent subsystem $\mathcal{T}$ experiences a population inversion which can be transferred to the rest of the system via η and η' and triggers a lasing instability.

In the dissipative dynamics of Eq. (2), we have also considered photon loss with rate κ to model finite linewidth of the cavity photon. The relaxation of the collective bosonic mode in a magnet, on the other hand, depends self-consistently on its dynamics [64]. We therefore consider, as an alternative, a viscous damping of the magnon condensate whenever the direct applications to spintronics are pertinent. In terms of magnetic dynamics, the phenomenological Gilbert damping [65] slows down the coherent precession of the order parameter and brings it towards the global equilibrium state [54,66]. Interestingly, our results remain qualitatively unaltered under dissipation through photon loss or Gilbert damping, see Appendix C.

Since our model (1) describes collective all-to-all interaction between spins, all quantum effects come from the noncommutativity of collective spins $[\mathcal{S}^\alpha/N, \mathcal{S}^\beta/N] = i\epsilon_{\alpha\beta\gamma}\mathcal{S}^\gamma/N^2 \propto 1/N$, which sets the effective Planck's constant of the model $h_{\text{eff}} \propto 1/N$ [67,68], (identical commutation relations hold for $\mathcal{T}$ spins). Thus, in the thermodynamic limit, $N \to \infty$, the mean-field treatment becomes exact [59,69,70]. From now on, we use the normalized variables $a \propto a/\sqrt{N}$, $\mathcal{S} \propto \mathcal{S}/N$, $\mathcal{T} \propto \mathcal{T}/N$, as is customary in the treatment of systems with collective light-matter interactions [57–59]. See Appendix A for the mean-field equations of motion of the normalized variables.

We start analyzing the model by revisiting some established dynamical regimes of the Hamiltonian in Eq. (1). The detailed solutions in the following two limits are discussed in Appendix B.

A. Dicke model

For $\eta = \eta' = 0$, we recover the Dicke model [59,71], which models photon-matter interaction in cavity QED. This model has been studied extensively theoretically [58,60,71,72] and implemented in few experimental platforms [18,73,74]. In the $N \to \infty$ limit, the Dicke model describes a second-order phase transition from the normal state (NS), in which $\langle \mathcal{S}^z \rangle = \pm 1/2$ and $\langle a^\dagger a \rangle = 0$ to a SR phase, which is associated with the spontaneous breaking of $\mathbb{Z}_2$ symmetry of the Hamiltonian and corresponds to $\langle \mathcal{S}^x \rangle \neq 0$ and $\langle a^\dagger a \rangle \neq 0$. Here $\langle . \rangle$ stands for the ensemble-averaged value of an observable. This picture remains qualitatively valid when small couplings η and η' are switched on while the spin pumping is weak, namely, $\gamma_\uparrow < \gamma_t/2$ [cf. Fig. 2(a)].

B. Tavis-Cummings model

The limit $\eta' = \lambda = 0$ corresponds to the incoherently pumped Tavis-Cummings model [57,59,63,75–77]. The system in this case is endowed with a $U(1)$ symmetry, corresponding to conservation of the total number of excitations of the spins and the boson.

For $\gamma_t \gg \eta, \eta'$, the system quickly relaxes towards a steady state with $\langle \mathcal{T}^z \rangle \approx (\gamma_\uparrow - \gamma_\downarrow)/(2\gamma_t) \equiv \tau_0^z$ and $\langle \mathcal{T}^\pm \rangle \approx 0$. For $\gamma_\uparrow/\gamma_t \geqslant 1/2 + \kappa\gamma_t/(8\eta^2) + \kappa\gamma_t(\omega_c - \omega_z')^2/(2\eta^2(\kappa + \gamma_t)^2)$, the nontrivial solution arises, where the symmetry is dynamically broken with $\langle a \rangle$ and $\langle \mathcal{T}^{x,y} \rangle$ undergoing oscillations. At long times, both $\langle \mathcal{T}^z \rangle$ and the photon number n approach the steady values set by the pumping rates $\gamma_{\uparrow/\downarrow}$; see Appendix B for more details. To acquire some intuitive insights, we take a look at the $\omega_c \approx \omega_z' \equiv \omega$ limit. In this case, the lasing solution is only possible when the photon loss rate is below a critical value, $\kappa < \kappa_c = 4\eta^2/\gamma_t$. In other words, given a finite photon loss rate, the lasing will be suppressed in the fast-relaxing ($\gamma_t \to \infty$) limit.

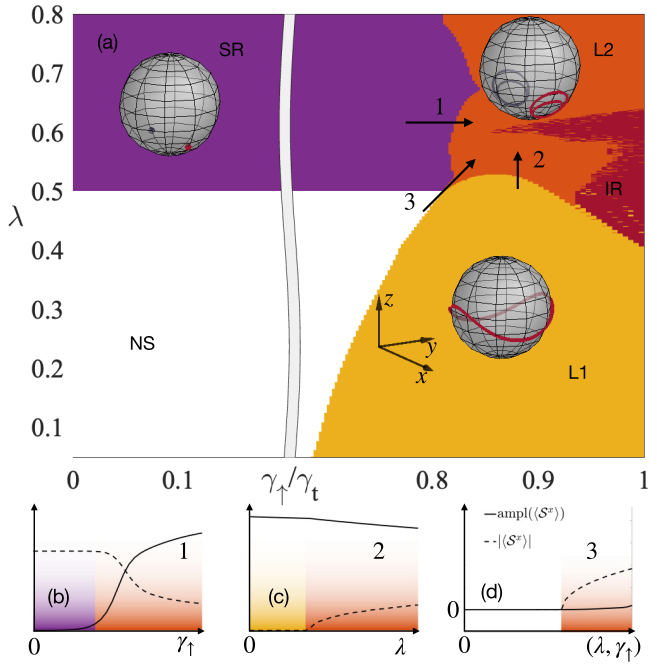

FIG. 2. Dynamical phases resulting from the interplay of spin pumping and Dicke coupling. (a) For $\gamma_\uparrow < \gamma_t/2$, the usual critical coupling ($\lambda_c \simeq 0.5$) associated to the Dicke transition separates the normal (NS) from the superradiant (SR) phase. For $\gamma_\uparrow > \gamma_t/2$, the normal state becomes unstable, and observables in the ensemble $\mathcal{S}$ oscillate with zero average value of $\mathcal{S}^x$ in region L1, and around one of the minima of the SR phase in region L2, as shown in the Bloch spheres. Inside the irregular (IR) region the motion of the collective spin covers uniformly a large part of the Bloch sphere without any structured pattern and is suggestive of chaotic behavior. (b)–(d) The absolute value of time-averaged $\langle \mathcal{S}^x \rangle$ (dashed line) and amplitude of its oscillations (solid line) along transition lines 1–3 in the main inset (a). Here we have chosen $\omega_c = \omega_z = \omega_z' = 1,\ \gamma_t = 1,$ $\eta = \eta' = 0.1,\ \kappa = 0.06$.

III. DYNAMICAL PHASE DIAGRAM

By turning on the Dicke coupling λ together with sizable spin pumping in the weakly coupling limit ($\eta,\ \eta' \to 0^+$), we generate the diagram of dynamical responses [cf. Fig. 2(a)] in mean-field treatment. In Appendix A, we present the associated equations of motion; we also analyze the breakdown of the mean field from finite N corrections in Appendix E.

For strong pumping ($\gamma_\uparrow > \gamma_t/2$), the spins in the ensemble $\mathcal{S}$ display long-lived oscillatory dynamics [see trajectories on the Bloch sphere in Fig. 2(a)]. Region L1 in Fig. 2(a) resembles the regular lasing [63] discussed above, while L2 features SR oscillations. The transition from L1 to L2 occurs around values of the Dicke coupling $\sim\lambda_c$, with a nonvanishing time average of $\langle \mathcal{S}^x \rangle$ in L2. In this phase, we observe persistent oscillatory dynamics reminiscent of lasing around one of the symmetry-broken states of the Dicke model. Such SR oscillations would not arise by direct pumping the Dicke model through the Lindblad channels in Eq. (2) but rather a result of the pumping scheme in Fig. 1 inspired by spintronic scenarios. In return, the emergence of this dynamical phase is also implicative for further possibilities of dynamical phenomena in spintronics. In this regard, the dynamical phase L2 is a conceptual bridge between the quantum optics and spintronics communities which we are aiming to lay out in this work. Notice that despite the pumped subsystem experiencing population inversion, the spin ensemble $\mathcal{S}$ remains in a state with negative $\langle \mathcal{S}^z \rangle$ in both phases L1 and L2.

We now discuss the role of symmetries in the oscillatory dynamics displayed in L1 and L2, and in the transitions between these two different regimes. For $\lambda = 0$, the photon number n does not oscillate. A nonzero value of λ breaks the $U(1)$ symmetry and oscillations in n can be attributed to ellipticity [78] in the spontaneous procession in the absence of $\mathcal{S}^z$ conservation. In fact, the dynamics are instead governed by a $\mathbb{Z}_2$ symmetry, reflected in the observation that the oscillatory frequency of n and $\langle \mathcal{S}^z \rangle$ is twice that of $\langle \mathcal{S}^x \rangle$. The time-averaged value of $\langle \mathcal{S}^x \rangle$ becomes nonzero at the transition from L1 to L2, which can be explained by the spontaneous breaking of the $\mathbb{Z}_2$ symmetry upon increasing the Dicke coupling λ [cf. Fig. 2(c)]. The transition from the SR region to the L2 region appears as a crossover in finite-time numerical data, as the damping of the oscillations of $\langle \mathcal{S}^x \rangle$ critically slows down upon approaching the transition point from the SR side, hence the time-averaged amplitude of the oscillations in long but finite time windows smoothly grows, blurring the expected singular behavior at the phase boundary [cf. Fig. 2(b)] associated to the dynamical spontaneous symmetry breaking of the $U(1)$ symmetry. Finally, in the transition from NS to L2, the absolute value of the time average of $\langle \mathcal{S}^x \rangle$, as well as its amplitude, build up [cf. Fig. 2(d)].

This dynamical phase diagram with competing stationary (NS, SR) and oscillatory (L1, L2, IR) phases is of great interest to spintronics, since it emerges from the interplay of incoherent spin pumping and ellipticity. We now briefly discuss some possible implications of our results. In previous studies, magnon conservation is taken to be an important ingredient in the study of coherent spin-wave lasing or magnon Bose-Einstein condensation in pumped magnetic systems [42,43]. The magnon lasing [39] features a convergence to a steady condensate density and a circular precession [42,43]. In our model, however, we explicitly induce a Dicke term that breaks $U(1)$ symmetry. For a small Dicke coupling, the spin trajectory in the L1 lasing phase becomes elliptical instead of perfectly circular. It is similarly expected that for a magnon condensate, an explicit $U(1)$ breaking induces an ellipticity in the spontaneous precession [79], accompanied by an oscillation of the condensate density. On the other hand, the emergence of the L2 phase is a much more dramatic effect, as the spin oscillation spontaneously breaks into two separate pockets, which cannot be described by any quasiequilibrium treatment. This behavior suggests that in the spintronic setup, an exotic form of lasing can be induced in the strongly $U(1)$ breaking regime lacking magnon conservation. This opens the possibility to study spin-wave lasing phenomena in a regime where both the $\mathbb{Z}_2$ interaction and spin pumping are sizable, and suggests richer phenomena accompanying nonequilibrium phase transitions in spintronic devices.

We also remark that during the electrical pumping, angular momentum transfers reciprocally between the magnet and metal [55]: As the itinerant electrons exert a spin torque to establish the magnon lasing, the coherent magnetic precession simultaneously pumps a spin current back into the metal [80],

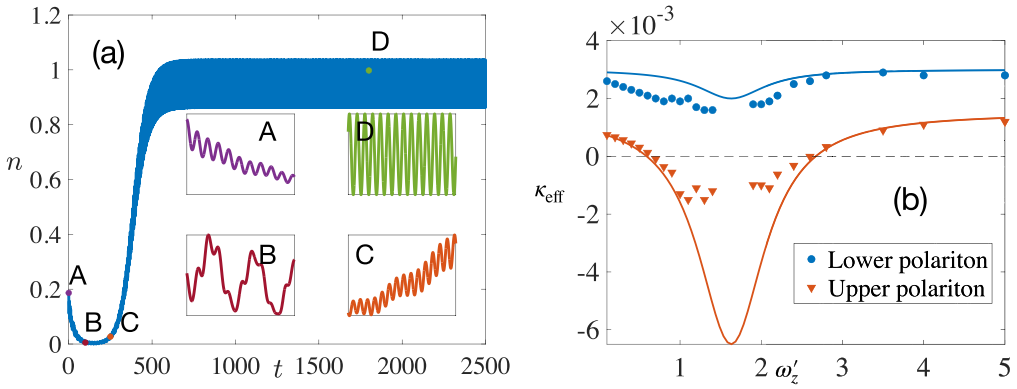

FIG. 3. (a) Dynamics of the photon number n with parameters as in Fig. 2, with the exception of ω_z', which is chosen in resonance with the upper polariton frequency ($\omega_z' \simeq \Omega_{\rm U}$). Insets show a stretched time axis. The system is prepared in the SR state and evolves with system parameters $\gamma_\uparrow$ and λ inside region L1. The initial stage of dynamics is governed by the decaying lower polariton mode, while at stage C the upper polariton mode undergoes the dynamical instability triggered by the resonance with the incoherent subsystem; accordingly, the photon number starts to grow until it saturates around times $t \simeq 500$. At long times, n oscillates at the upper polariton frequency, see stage *D*. This is illustrative of the spin ensemble $\mathcal{T}$ acting as a frequency-dependent gain medium. (b) The effective decay rate for the photon number $n \propto \exp(-\kappa_{\rm eff} t)$ extracted in stage A (blue circles) and stage C (red triangles) of dynamics in (a), as a function of the frequency of the incoherent subsystem ω_z'. Close to the resonant frequency of the upper polariton, $\Omega_{\rm U} = 1.63$, the effective damping $\kappa_{\rm eff} = 2\kappa_{\rm U}$ can change signs, indicating a dynamical instability, which results in the polariton lasing. Solid lines show analytical dependence according to Eq. (4).

triggering transverse spin dynamics. Therefore, suppressing the transverse spin dynamics in the metal can be detrimental to magnon lasing, as consistent with the consequence of a fast-relaxing incoherent subsystem in the Tavis-Cumming model, cf. Sec. II B. Also see below Eq. (5) for related discussion.

IV. POLARITON LASING

Observables in the L1 and L2 phases show signatures of upper (U) and lower (L) polariton modes [58], which are symmetric (U) and antisymmetric (L) linear superpositions of spin and boson fields, describing light-matter hybridization via the Dicke coupling λ. To appreciate this point, we rewrite the interaction term in Eq. (1) as $H_{\rm int} = (\eta a + \eta' \mathcal{S}^-)\mathcal{T}^+ + \text{H.c.}$, which is suggestive that pumping the $\mathcal{T}$ ensemble can excite a superposition of light and matter in the $\mathcal{S}$ system. Thus, upper or lower polaritons can be excited in the system, depending on whether the two couplings have the same or opposite signs, jointly with the resonance condition, $\omega_z' \simeq \Omega_{\rm U/L}$, where within NS the eigenfrequencies read [58]

$$\Omega_{\rm U/L} = \sqrt{\left(\omega_c^2 + \omega_z^2 \pm \sqrt{\left(\omega_c^2 - \omega_z^2\right)^2 + 16\lambda^2\omega_z\omega_c}\right)/2}. \quad (3)$$

The effective decay rates of the two polariton modes $\psi_{\rm U,L}$ depend on the frequency of the incoherent subsystem ω_z' and, in particular, for $\eta = \eta'$, it can be analytically estimated as

$$\kappa_{\rm U} = \kappa/4 - \eta^2(\gamma_\uparrow - \gamma_\downarrow)/\left[(\omega_z' - \Omega_{\rm U})^2 + \gamma_t^2/4\right]. \quad (4)$$

By tuning ω_z' close to $\Omega_{\rm U}$, it is possible to obtain a negative effective decay rate ($\kappa_{\rm U} < 0$) for $\gamma_\uparrow > \gamma_\downarrow$ that induced dynamical instabilities into the system.

The boson annihilation operator a can be written as the sum of upper and lower polaritons, and thus both modes contribute to the dynamics of photon number $n = \langle a^\dagger a\rangle$. However, their effective decay rates are different, giving rise to different short- and long-time behaviors of the dynamics of n. This can be seen explicitly by considering a quench from the stationary SR phase to the nonstationary lasing phase, as shown in Fig. 3(a). Here, we initialize the system in the SR steady state of the Dicke model with photon losses ($\lambda = 0.6$ and $\kappa = 0.06$) and let it evolve with parameters characteristic of the L1 phase ($\lambda = 0.2$, $\gamma_\uparrow = 0.9$) while keeping $\omega_z' \approx \Omega_{\rm U}$. We now discuss the multistage dynamics [as marked by A–D in Fig. 3(a)] associated with this protocol. Inside the SR phase, the difference between the amplitudes of upper and lower modes can be estimated using the Holstein-Primakoff analysis [58] as

$$\frac{|\psi_{\rm U}|}{|\psi_{\rm L}|} = \left|\frac{1 - 2\lambda(\omega_c + i\kappa/2)/\left(\omega_c^2 + \kappa^2/4\right)}{1 + 2\lambda(\omega_c + i\kappa/2)/\left(\omega_c^2 + \kappa^2/4\right)}\right| \approx \left|\frac{1 - 2\lambda/\omega_c}{1 + 2\lambda/\omega_c}\right|,$$

which is much smaller than 1 close to λ_c. Thus, initializing a system in the SR phase corresponds to setting it into a lower polariton mode. As we fix $\omega_z' \approx \Omega_{\rm U}$ and set the rest of the parameters to be such that $\kappa_{\rm U} < 0$, the upper polariton in this scenario is exponentially enhanced at the beginning of the dynamics, while the lower polariton has $\kappa_{\rm L} > 0$ and thus decays. Therefore, immediately after the quench (A), the photon field has a sizable overlap with the lower polariton mode. Since in the initial SR steady state the boson is enslaved to matter [$\langle a\rangle = -2\lambda/(\omega_c - i\kappa/2)\langle\mathcal{S}^-\rangle$], the amplitude of the lower mode is larger than the amplitude of the upper one. However, as the lower mode starts to decay and the upper one is enhanced, their amplitudes become comparable (B) and we observe beating at their two frequencies. At stage (C), the photon number increases while the lower mode is largely suppressed. As a result, for long times (D), the oscillatory dynamics of the system is solely governed by $\Omega_{\rm U}$. Such circumstances cannot occur in a more conventional driven-dissipative Dicke model [75] since, in that case, both upper and lower modes would be enhanced and survive at long times.

Finally, we verify the dependence in Eq. (4) numerically by studying the relaxation of the system after quenching from the SR phase to the nonstationary lasing phase. We extract the effective decay rate of the photon mode, which is given by $n = \langle a^\dagger a\rangle \propto \exp(-\kappa_{\rm eff} t)$, in different parametric regimes. Depending on the level splitting of the $\mathcal{T}$ spins, ω_z', $\kappa_{\rm eff}$ can be varied. Figure 3(b) shows the effective damping $\kappa_{\rm eff}$ of the photon mode as a function of ω_z'. The effective damping coefficients $\kappa_{\rm U/L}$ of the lower and upper modes are extracted from the dynamics of n at short [stage (A) in Fig. 3(a)] and long [stage (C) in Fig. 3(a)] timescales, respectively. As one can see from Fig. 3(b), both damping coefficients have a minimum close to the resonance upper polariton frequency. Also, for all frequencies ω_z', the damping of the lower mode is faster than that of the upper polariton, which is why we observe oscillations at long times with frequency $\Omega_{\rm U}$ only. The upper mode is long-lived and can even be enhanced via pumping when ω_z' is close enough to the upper polariton frequency $\Omega_{\rm U}$, resulting in lasing.

If the system is pumped resonantly with the upper polariton frequency $\omega_z' \simeq \Omega_{\rm U}$, the critical value of $\gamma_\uparrow$ at which the lasing region occurs can be estimated as

$$\frac{\gamma_\uparrow}{\gamma_t} \geqslant \frac{1}{2}\left(\frac{\kappa\gamma_t}{16\eta^2}+1\right), \tag{5}$$

following a calculation similar to the one in Sec. II B. This also constrains the condition between pumping/relaxation rates and coherent coupling η under which non-stationary phases can be observed, i.e., the right-hand side of Eq. (5) cannot exceed 1. Otherwise, the typical relaxation time of the incoherent subsystem $\mathcal{T} \propto 1/\gamma_t$ is faster than growing time of the coherent subsystem [59,60], which means that mutual dynamics of the coherent and incoherent parts does not have time to establish itself. For the polariton mode, lasing is obtained at a pumping frequency smaller than the conventional threshold for lasing $\omega_z' \leqslant \Omega_U + \sqrt{4\eta^2(\gamma_\uparrow - \gamma_\downarrow)/\kappa - \gamma_t^2/4}$. Similarly, the lower polariton mode can be resonantly pumped when $\eta = -\eta'$. In this case, the effective damping for both modes have a minimum at the lower polariton frequency $\Omega_{\rm L}$.

V. CONCLUSION AND OUTLOOK

In this paper, we bridge cavity QED and spintronics communities by suggesting the model that could find the implementation in both areas. We have captured the essential overlapping ingredients with a particular focus on the symmetry properties and shown that our approach can promote discovery of new dynamical phases with nontrivial interpretation from both standpoints. A further development of our model (1) and the accessibility of different parametric regimes in different platforms can be inspiring for the study of emergent dynamical phenomena in general.

A natural next step forward would consist of studying collective spin squeezing in the lasing regime [81–83], with the perspective of entanglement manipulation in spintronics platforms. This can be addressed, for instance, by simulating numerically exact dynamics at finite N [84,85].

Recent studies have shown the usefulness of nonlocal dissipation in generating entanglement between distant qubits in both fields of quantum optics and spintronics, by investigating spins immersed in an optical cavity [14,15,86] and nitrogen-vacancy qubits in proximity to a magnetic medium [87]. For the latter, dynamical phase transitions in the magnet controlled by electrical pumping may provide an efficient tunability of nonlocal dissipation, which could be studied along the lines of this paper.

Finally, we did not include here the effect of short-range spin interactions breaking permutational symmetry. This is, in general, a challenging task since it requires a full many-body treatment of dynamics. However, we expect that, deep inside the various phases, the dynamical phenomena discussed here will still hold in analogy with the character of other nonequilibrium phases in spin systems with competing short- and all-to-all interactions [68,88,89].

Our results can be considered as a roadmap to build a generation of spintronics experiments inspired by quantum optics, with a focus on dynamical phase transitions in heterolayer structures. Scaling up our proof of concept to more concrete platforms appears to be an exciting future direction.

ACKNOWLEDGMENTS

J.M. and O.C. are indebted to P. Kirton for enlightening discussions. O.C. thanks S. Kelly and R. J. Valencia-Tortora for helpful comments on this paper. This project has been supported by the Deutsche Forschungsgemeinschaft (DFG, German Research Foundation) through the Project ID 429529648—TRR 306 ("QuCoLiMa Quantum Cooperativity of Light and Matter"), by the Dynamics and Topology Centre funded by the State of Rhineland Palatinate, and in part by the National Science Foundation under Grant No. NSF PHY-1748958 (KITP program Non-Equilibrium Universality: From Classical to Quantum and Back). J.M. and O.C. acknowledge support by the Dynamics and Topology Centre funded by the State of Rhineland Palatinate. A.L. acknowledges support by the Swiss National Science Foundation. S.Z. and Y.T. are supported by the U.S. Department of Energy, Office of Basic Energy Sciences under Grant No. DE-SC0012190. The Alexander von Humboldt Foundation is acknowledged for supporting Y.T.'s stay at Mainz, where this work was initiated. I.C. acknowledges financial support from the H2020-FETFLAG-2018-2020 project PhoQuS (No. 820392) and from the Provincia Autonoma di Trento.

APPENDIX A: STABILITY ANALYSIS

The mean-field equations of motion used to derive the phase diagram in Fig. 2(a) read

$$\frac{d\langle a\rangle}{dt} = -i\eta\langle\mathcal{T}^-\rangle - (i\omega_c + \kappa/2)\langle a\rangle - i\lambda(\langle\mathcal{S}^+\rangle + \langle\mathcal{S}^-\rangle)$$

$$\frac{d\langle\mathcal{S}^z\rangle}{dt} = i\lambda(\langle a\rangle + \langle a^\dagger\rangle)(\langle\mathcal{S}^-\rangle - \langle\mathcal{S}^+\rangle) + i\eta'(\langle\mathcal{T}^+\rangle\langle\mathcal{S}^-\rangle - \langle\mathcal{T}^-\rangle\langle\mathcal{S}^+\rangle)$$

$$\frac{d\langle\mathcal{S}^-\rangle}{dt} = -i\omega_z\langle\mathcal{S}^-\rangle + 2i\lambda(\langle a\rangle + \langle a^\dagger\rangle)\langle\mathcal{S}^z\rangle + 2i\eta'\langle\mathcal{T}^-\rangle\langle\mathcal{S}^z\rangle$$

$$\frac{d\langle\mathcal{T}^z\rangle}{dt} = i\eta(\langle a^\dagger\rangle\langle\mathcal{T}^-\rangle - \langle a\rangle\langle\mathcal{T}^+\rangle) - i\eta'(\langle\mathcal{T}^+\rangle\langle\mathcal{S}^-\rangle - \langle\mathcal{T}^-\rangle\langle\mathcal{S}^+\rangle) + \frac{\gamma_\uparrow - \gamma_\downarrow}{2} - \gamma_t\langle\mathcal{T}^z\rangle$$
$$\frac{d\langle\mathcal{T}^-\rangle}{dt} = -(i\omega_z' + \gamma_t/2)\langle\mathcal{T}^-\rangle + 2i\eta\langle a\rangle\langle\mathcal{T}^z\rangle + 2i\eta'\langle\mathcal{T}^z\rangle\langle\mathcal{S}^-\rangle, \tag{A1}$$

where $\langle . \rangle$ stands for the ensemble-averaged value of an observable. Here we neglected higher order correlations which are all suppressed as $1/N$, approximating $\langle AB\rangle \approx \langle A\rangle\langle B\rangle$. This approximation is exact in the $N \to \infty$ limit [57]. All variables in Eqs. (A1) are intensive, since they are normalized in such a way that they are independent of the number of spins N as $N \to \infty$.

From the equation above, we study the instabilities of the NS. By perturbing with small fluctuations around the NS expectation values $\langle a\rangle = \langle a\rangle_0 + \delta a$, $\langle\mathcal{S}^-\rangle = \langle\mathcal{S}^-\rangle_0 + \delta\mathcal{S}^-$, $\langle\mathcal{T}^-\rangle = \langle\mathcal{T}^-\rangle_0 + \delta\mathcal{T}^-$, (with $\langle a\rangle_0 = \langle\mathcal{S}^-\rangle_0 = \langle\mathcal{T}^-\rangle_0 = 0$, $\langle\mathcal{S}^z\rangle = -1/2$ and $\langle\mathcal{T}^z\rangle = (\gamma_\uparrow - \gamma_\downarrow)/(2\gamma_t)$), we can find a linear system of equations for these deviations from the NS, which can be written in the form $\dot{x} = Ax$, where $x = (\delta a, \delta a^*, \delta\mathcal{S}^-, \delta\mathcal{S}^+, \delta\mathcal{T}^-, \delta\mathcal{T}^+)^T$. This matrix reads

$$A = \begin{bmatrix} -i\omega_c - \frac{\kappa}{2} & 0 & -i\lambda & -i\lambda & -i\eta & 0 \\ 0 & i\omega_c - \frac{\kappa}{2} & i\lambda & i\lambda & 0 & i\eta \\ -i\lambda & -i\lambda & -i\omega_z & 0 & -i\eta' & 0 \\ i\lambda & i\lambda & 0 & i\omega_z & 0 & i\eta' \\ 2i\eta\langle\mathcal{T}^z\rangle & 0 & 2i\eta'\langle\mathcal{T}^z\rangle & 0 & -i\omega_z' - \frac{\gamma_t}{2} & 0 \\ 0 & -2i\eta\langle\mathcal{T}^z\rangle & 0 & -2i\eta'\langle\mathcal{T}^z\rangle & 0 & i\omega_z' - \frac{\gamma_t}{2} \end{bmatrix}. \tag{A2}$$

By performing a stability analysis [75], one can distinguish the set of parameters for which the NS is stable (cf. Fig. 4). The white region with all negative eigenvalues corresponds to the stable normal phase. The purple region with one real positive eigenvalue matches the boundary of the SR phase in Fig. 2(a). The yellow region with two positive complex conjugate eigenvalues corresponds to lasing. The parameters in the orange region corresponds to the three positive eigenvalues of the matrix Eq. (A2). The boundary between the SR and NS is well approximated by the λ_c of the Dicke model [58,75]. However, this simple stability analysis does not capture the difference between dynamical phases such as L1, L2, and IR in Fig. 2(a), which require a through evaluation of the far-from-equilibrium dynamics encoded in Eqs. (A1).

When we pump the system at a frequency resonant with the upper polariton frequency, $\omega_z' \approx \Omega_U$, the boundary of the lasing region can undergo drastic changes. As shown in Fig. 5, in this case the boundary between the NS and lasing phase is solely set by the critical value of pumping rate $\gamma_\uparrow/\gamma_t$ and does not depend on λ.

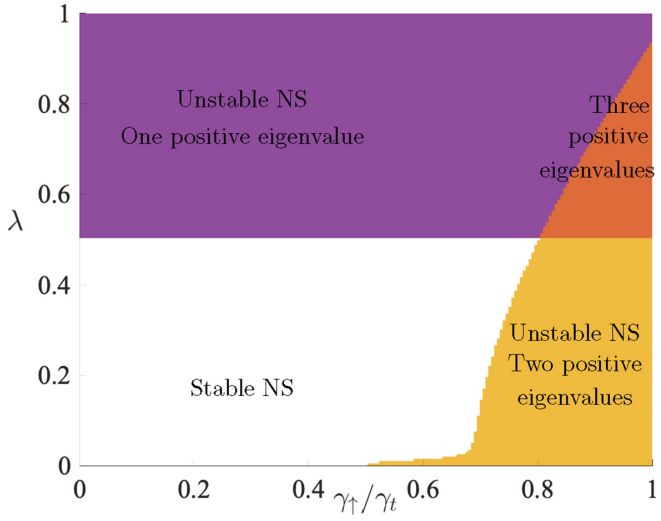

FIG. 4. Stability analysis of the normal state. The parameters are the same as in Fig. 2(a). The stable normal state is indicated in white. The purple color corresponds to one real positive eigenvalue of the matrix A and it indicates superradiance. The yellow region corresponds to two complex conjugated eigenvalues with positive real part and it corresponds to the lasing region. The orange region corresponds to the three positive eigenvalues. Here $\omega = \omega_z'$.

APPENDIX B: DICKE AND TAVIS-CUMMINGS MODELS

In this Appendix, we examine two known limits of the model (1) and their mean-field solutions.

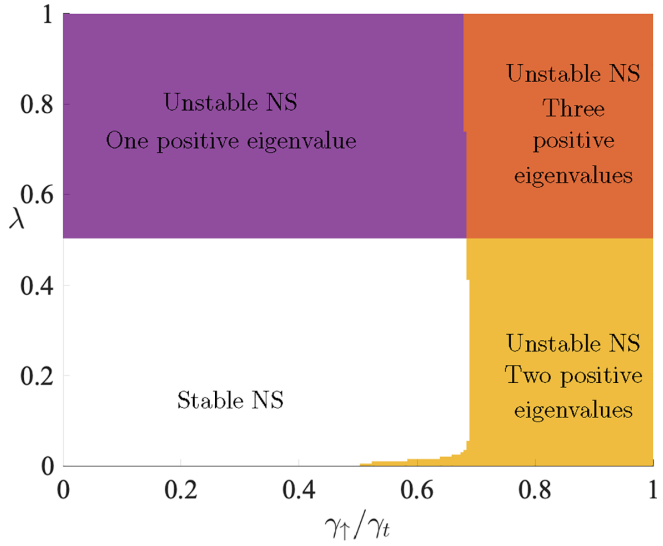

FIG. 5. Stability analysis with the resonance condition $\omega_z' = \Omega_U$. The rest of the parameters are the same as in Fig. 2(a). The vertical boundary between normal state (white) and lasing (yellow) is given by the critical pumping rate $\gamma_\uparrow^c \approx 0.7\gamma_t$ [see Eq. (5)].

In the limit of $\eta = \eta' = 0$, our model is reduced to the Dicke model with a spontaneous $\mathbb{Z}_2$-breaking transition. For $\lambda < \lambda_c = \sqrt{\omega_z(\omega_c^2 + \kappa^2/4)/(4\omega_c)}$, the stationary state of Eq. (A1) is $\langle a\rangle = \langle \mathcal{S}^{x,y}\rangle = 0$ and $\langle \mathcal{S}^z\rangle = \pm 1/2$. For $\lambda \geqslant \lambda_c$, a pair of nontrivial solutions breaking the $\mathbb{Z}_2$ symmetry appear, such that $\langle \mathcal{S}^z\rangle = -(1 - \lambda_c^2/\lambda^2)/2$, $\langle \mathcal{S}^x\rangle = \pm\sqrt{1/4 - \langle \mathcal{S}^z\rangle^2}$, $\langle a\rangle = -2\lambda\langle \mathcal{S}^x\rangle/(\omega_c + i\kappa/2)$.

The other limit $\eta' = \lambda = 0$ corresponds to the incoherently pumped Tavis-Cummings model. For $\gamma_t \gg \eta, \eta'$, the last line of the mean-field equations of motion in Eq. (A1) shows a quick relaxation towards a steady state with $\langle \mathcal{T}^z\rangle \approx (\gamma_\uparrow - \gamma_\downarrow)/(2\gamma_t) \equiv \tau_0^z$ and $\langle \mathcal{T}^\pm\rangle \approx 0$. The system is driven into a mixed state with a relative population of up and down spins controlled by the ratio $\gamma_\uparrow/\gamma_t$. Nontrivial solutions of the mean-field equations of motion (A1) that break dynamically the symmetry can be expressed in the form (see, for instance, Refs. [76,77])

$$\langle a\rangle \to a_0 e^{-i\Delta t}, \quad \langle \mathcal{T}^\pm\rangle \to \mathcal{T}_0^\pm e^{\pm i\Delta t}, \tag{B1}$$

where Δ is a characteristic frequency to be self-consistently determined. Substituting Eqs. (B1) into Eqs. (A1), one obtains

$$\begin{aligned}
\Delta &= \frac{\kappa\omega_z' + \gamma_t\omega_c}{\kappa + \gamma_t}\\
\langle \mathcal{T}^z\rangle &= \frac{\gamma_t\kappa}{2\eta^2}\left(\frac{(\omega_c - \omega_z')^2}{(\kappa + \gamma_t)^2} + \frac{1}{4}\right)\\
\mathcal{T}_0^\pm &= \sqrt{\frac{\gamma_t\tau_0^z\kappa}{\eta^2}\left(\frac{(\omega_c - \omega_z')^2}{(\kappa + \gamma_t)^2} + \frac{1}{4}\right) - \frac{\gamma_t^2\kappa^2}{2\eta^4}\left(\frac{(\omega_c - \omega_z')^2}{(\kappa + \gamma_t)^2} + \frac{1}{4}\right)^2}.
\end{aligned} \tag{B2}$$

Further simplification is possible in the $\omega_c \approx \omega_z' \equiv \omega$ limit,

$$\begin{aligned}
\Delta &= \omega\\
\langle \mathcal{T}^z\rangle &= \frac{\gamma_t\kappa}{8\eta^2}\\
\langle \mathcal{T}^\pm\rangle &= \sqrt{\frac{\gamma_t\tau_0^z\kappa}{4\eta^2} - \frac{\gamma_t^2\kappa^2}{32\eta^4}}\, e^{\pm i\omega t}\\
n &= \frac{\gamma_t}{\kappa}\left(\tau_0^z - \langle \mathcal{T}^z\rangle\right),
\end{aligned} \tag{B3}$$

from which it is clear that the lasing solution exists only if the photon loss rate is below a critical value $\kappa < \kappa_c = 4\eta^2/\gamma_t$.

APPENDIX C: GILBERT DAMPING

For the magnon condensate mode, dissipation in the form of Gilbert damping slows down the spontaneous precession of the magnetic order parameter like a viscous drag [54]. It is particularly suitable in the weak-damping scenario to describe the relaxation of the precessional motion back to the equilibrium state (in the absence of external pumping) along a spiral trajectory without losing coherence. The semiclassical Landau-Lifshitz-Gilbert equation [65,90,91] of a spin $\mathbf{s}$ reads $d\mathbf{s}/dt = \mathbf{s} \times \mathbf{h}_{\rm eff} - \alpha_G \mathbf{s} \times d\mathbf{s}/dt$, where $\mathbf{h}_{\rm eff}$ is an effective Zeeman field fixing the equilibrium spin orientation and α_G is the Gilbert damping. A small-angle spin precession can be mapped to the motion of a harmonic oscillator with creation and annihilation operators [92] $a^\dagger$ and a, where $s_z = s - a^\dagger a \approx s$ with s being the spin length. The Landau-Lifshitz-Gilbert equation in the lowest order thus becomes $(1 + is\alpha_G)d\langle a\rangle/dt = -i\omega_c\langle a\rangle$, where $\omega_c = |\mathbf{h}_{\rm eff}|$. Such a form of the viscous drag can also be derived by coupling the bosonic mode a to an Ohmic bath and eliminating the bath degrees of freedom following a standard Caldeira-Leggett derivation [62].

For the model (1), the Gilbert damping modifies the mean-field equation of motion for the expectation value of the bosonic mode into

$$\begin{aligned}
(1 + i\kappa/2)\frac{d\langle a\rangle}{dt} &= -i(\omega_c - \tilde{\Delta})\langle a\rangle - i\eta\langle \mathcal{T}^-\rangle\\
&\quad - i\lambda(\langle \mathcal{S}^+\rangle + \langle \mathcal{S}^-\rangle) + \frac{B(t)}{\sqrt{N}}.
\end{aligned} \tag{C1}$$

Here $\tilde{\Delta}$ is a Lamb shift and $B(t)$ is the noise term that results from the bath [62]. This term is suppressed as $1/\sqrt{N}$ for large N, therefore vanishing in the mean-field limit. The dynamical phase diagram with this type of dissipation is plotted in Fig. 6. Here we fixed $\tilde{\omega}_c = \omega_c - \tilde{\Delta} = 1$ and $\kappa = 0.04$. Qualitatively, the diagram remains the same as if we used photon losses;

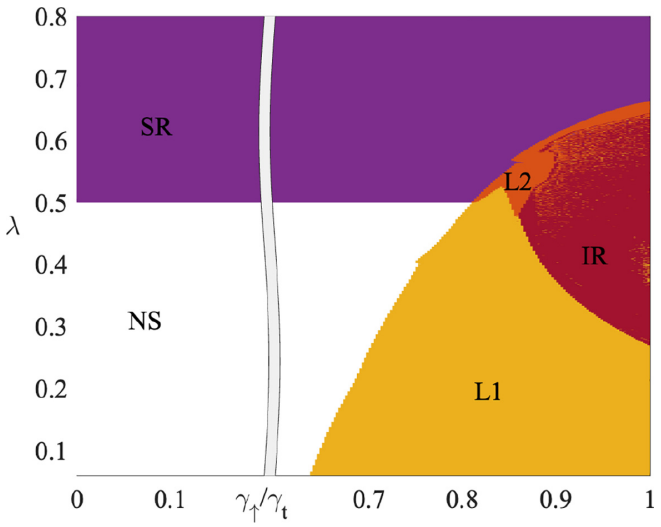

FIG. 6. Dynamical phase diagram with Gilbert damping [see Eq. (C1)]. All parameters are as in Fig. 7 and the color code follows Fig. 2(a).

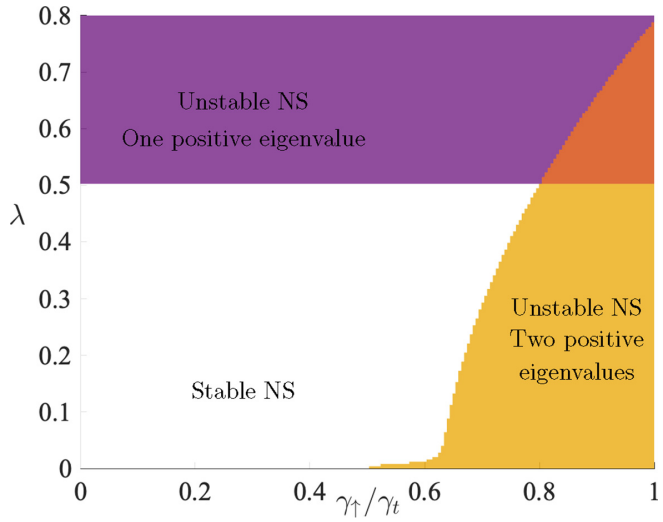

FIG. 7. Stability analysis for model with Gilbert damping. All parameters are as in Fig. 2(a), $\kappa = 0.04$, and the color code follows Fig. 4.

we still recognize five different dynamical responses as superradiance, NS, and lasing and SR persistent oscillations (L1 and L2), as well as irregular dynamics (IR), although the boundaries between phases are quantitatively modified. Results are in a good agreement with predictions obtained from the stability analysis (cf. Fig. 7).

APPENDIX D: INSTABILITIES FROM ADIABATIC ELIMINATION

We now work out analytically some dynamical properties of our system in the limit of a fast relaxing bath [93], known as adiabatic elimination of the bath in quantum optics. We choose γ_t large enough compared to η and η' to induce relaxation of the incoherent subsystem $\mathcal{T}$ much faster than the dynamics of the coherent one $\mathcal{S}$. Following Refs. [94,95], we can enslave the spins of the incoherent ensembles to those of the Dicke system by setting the time derivatives of the former to zero:

$$\begin{aligned}\langle \mathcal{T}^-\rangle &\simeq \frac{2\langle \mathcal{T}^z\rangle(\omega_z' + i\gamma_t/2)}{\omega_z'^2+\gamma_t^2/4}(\eta\langle a\rangle + \eta'\langle \mathcal{S}^-\rangle) + ...,\\ \langle \mathcal{T}^+\rangle &\simeq \frac{2\langle \mathcal{T}^z\rangle(\omega_z' - i\gamma_t/2)}{\omega_z'^2+\gamma_t^2/4}(\eta\langle a^\dagger\rangle + \eta'\langle \mathcal{S}^+\rangle) + ...\\ \langle \mathcal{T}^z\rangle &\simeq (\gamma_\uparrow - \gamma_\downarrow)/2\gamma_t + ...,\end{aligned} \tag{D1}$$

where we neglect terms in higher orders of $1/\gamma_t$. This is equivalent to assuming that spins in the $\mathcal{T}$ ensemble have already reached their steady state. When substituting Eq. (D1) into the equations of motion for the normalized cavity mode and for the spins of the coherent subsystem $\mathcal{S}$, we find

$$\begin{aligned}\langle \dot a\rangle = &-\left(i\omega_c + \frac{\kappa}{2}\right)\langle a\rangle - i\eta\left(\frac{2\eta\langle \mathcal{T}^z\rangle}{\omega_z' - i\gamma_t/2}\langle a\rangle\right.\\ &\left.+\frac{2\eta'\langle \mathcal{T}^z\rangle}{\omega_z' - i\gamma_t/2}\langle \mathcal{S}^-\rangle\right) - i\lambda(\langle \mathcal{S}^+\rangle + \langle \mathcal{S}^-\rangle).\end{aligned} \tag{D2}$$

The dissipative dynamics of the subsystem $\mathcal{S}$ and the photon mode can now be described with Lindblad terms with effective jump operators $L_1 = \sqrt{\gamma_\uparrow}\tau_i^+$ and $L_2 = \sqrt{\gamma_\downarrow}\tau_i^-$, given in terms of a and $\mathcal{S}^-$ through Eqs. (D1). From Eq. (D2), we find

$$\langle \dot a\rangle = (-i\tilde\omega - \tilde\kappa)\langle a\rangle - i\lambda(\langle \mathcal{S}^+\rangle + \langle \mathcal{S}^-\rangle) - \frac{2i\eta\eta'\langle \mathcal{T}^z\rangle}{\omega_z' - i\gamma_t/2}\langle \mathcal{S}^-\rangle, \tag{D3}$$

where

$$\tilde\omega = \omega_c - \frac{2\eta^2\omega_z'\langle \mathcal{T}^z\rangle}{\omega_z'^2+\gamma_t^2/4}, \quad \tilde\kappa = \frac{\kappa}{2} - \frac{\gamma_\uparrow - \gamma_\downarrow}{2}\frac{\eta^2}{\omega_z'^2+\gamma_t^2/4}. \tag{D4}$$

According to the last formula in Eqs. (D4), when the incoherent ensemble is in the population inverted state, the photon mode becomes effectively pumped due to the weak interaction with $\mathcal{T}$. If this pumping overcomes the photon decay κ, the photon number starts to grow and dynamical instabilities are triggered.

The equation that effectively governs the dynamics of the coherent subsystem can be derived in the same way and reads

$$\begin{aligned}\langle \dot{\mathcal{S}}^-\rangle = &-i\omega_z\langle \mathcal{S}^-\rangle + 2i\lambda(\langle a\rangle + \langle a^\dagger\rangle)\langle \mathcal{S}^z\rangle\\ &+\frac{2i\eta'(\omega_z' + i\gamma_t/2)(\gamma_\uparrow - \gamma_\downarrow)\langle \mathcal{S}^z\rangle}{\gamma_t\left(\omega_z'^2+\gamma_t^2/4\right)}(\eta\langle a\rangle + \eta'\langle \mathcal{S}^-\rangle).\end{aligned}$$

Here the effective contribution from the dissipator has the form

$$\langle \dot{\mathcal{S}}^-\rangle \propto \frac{\eta'(\gamma_\uparrow - \gamma_\downarrow)(-\langle \mathcal{S}^z\rangle)}{\omega_z'^2+\gamma_t^2/4}(\eta\langle a\rangle + \eta'\langle \mathcal{S}^-\rangle).$$

Therefore, for regions with $\gamma_\uparrow > \gamma_\downarrow$, spins in the system are effectively pumped by a rate proportional to the magnetization along $\hat z$, provided $\langle \mathcal{S}^z\rangle$ is negative (as it occurs in the NS or in the SR phase).

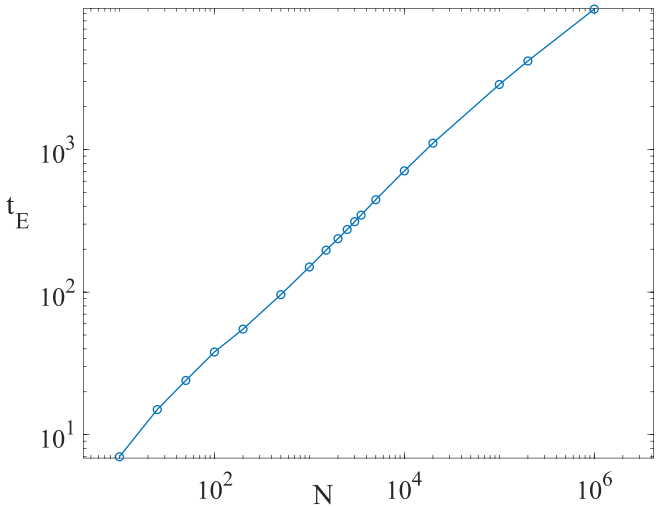

FIG. 8. Fit of the timescale $t_E \propto N^\delta$ with $\delta \simeq 0.5$ as a function of number of spins in the system, N, within the lasing region. We extract t_E as the time when the ratio between second cumulants and mean-field expectation values becomes of order ∼0.1.

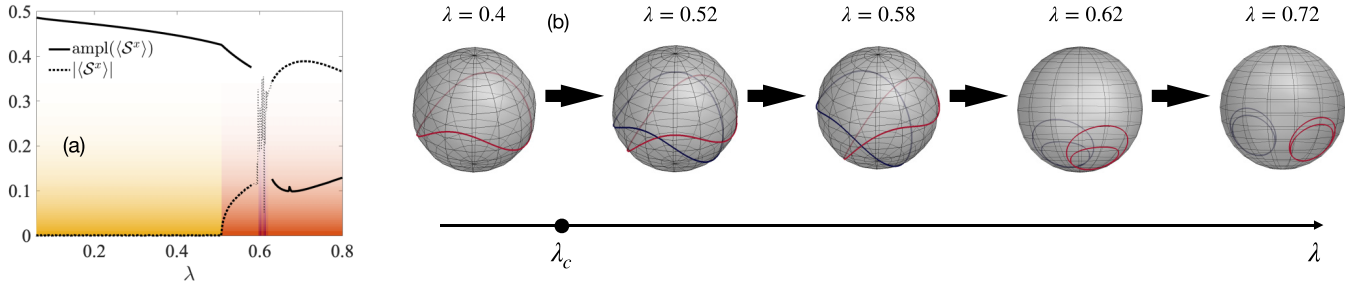

FIG. 9. (a) Amplitude of the oscillations of the $\langle \mathcal{S}^x \rangle$ (solid line) and absolute value of the time-averaged $\langle \mathcal{S}^x \rangle$ (dashed line) as a function of λ. We choose all parameters as in Fig. 2 and fixed $\gamma_\uparrow = 0.9\gamma_t$. The colors are the same as in Fig. 2. Yellow, orange, and red colors correspond to L1, L2, and IR phases, respectively. (b) Dynamics of the spin $\langle \mathcal{S} \rangle$ on the Bloch sphere inside L1 and L2 regions for different values of λ. Note that inside the L2 region, depending on the initial conditions, one of two trajectories is possible with opposite time-averaged values of $\langle \mathcal{S}^x \rangle_t = \pm s_0^x$.

Adiabatic elimination of the incoherent subsystem gives correct predictions for $\lambda = 0$. For $\lambda \neq 0$, light and matter hybridize and a separate analysis is required, see Sec. IV.

APPENDIX E: SEMICLASSICAL ANALYSIS

In models with collective, permutation-symmetric interactions, one can consider the leading effect of $1/N$ corrections beyond mean field by including second-order connected correlation functions [96,97]. In general, for finite values of N, all higher order connected correlations are relevant for dynamics; however, their effect is expected to be parametrically small in increasing powers of $1/N$ (if N is large). This is at the root of the solvability of models with all-to-all interactions mediated by a common bosonic mode, as in our system: the BBGKY hierarchy [98,99] closes when large system sizes are considered, allowing for nonperturbative solutions in the couplings governing both unitary or dissipative dynamics.

We include two-point connected correlation functions which couple to mean-field motion, neglecting third and higher order cumulants by approximating three point functions by their disconnected component

$$\langle ABC \rangle \simeq \langle AB \rangle \langle C \rangle + \langle AC \rangle \langle B \rangle + \langle BC \rangle \langle A \rangle - 2\langle A \rangle \langle B \rangle \langle C \rangle.$$

We simulate the dynamics and compare them with the mean-field solution to estimate the timescale, t_E, where cumulants have sufficiently grown to invalidate the mean-field description. We find that inside the L1 phase, t_E scales as the square root of the number of spins (cf. Fig. 8). After t_E, one would have to take into account higher order correlations to correctly predict the dynamics. At times $t \sim O(N)$, the dynamics of correlations undergo phase diffusion [100,101].

APPENDIX F: DIFFERENCE BETWEEN L1 AND L2 REGIONS

In this section, we consider how the transition between phases L1 and L2 is captured in dynamics of observables. As we pointed out in Sec. III, inside the L1 region the dynamics have unbroken $\mathbb{Z}_2$ symmetry. Spins components oscillate in time; the frequency of oscillations of $\langle \mathcal{S}^z \rangle$ is twice the frequency of oscillations of $\langle \mathcal{S}^x \rangle$ and $\langle \mathcal{S}^y \rangle$. These latter two observables have zero time average. By increasing λ above λ_c, the time-averaged value of $\langle \mathcal{S}^x \rangle$ becomes finite $\langle \mathcal{S}^x \rangle_t = \pm s_0^x$ while the amplitude of oscillations decreases. In Fig. 9(a), the amplitude of oscillations (solid line) and absolute value of the time-averaged $\langle \mathcal{S}^x \rangle$ (dashed line) are plotted as functions of λ. In Fig. 9(b), trajectories of $\langle \mathcal{S} \rangle$ for different values of λ are shown. Note that for $\lambda > \lambda_c$, depending on initial conditions, one of two trajectories (red or blue lines) is possible with time-averaged $\langle \mathcal{S}^x \rangle_t = \pm s_0^x$, respectively.

[1] I. Carusotto and C. Ciuti, Quantum fluids of light, Rev. Mod. Phys. **85**, 299 (2013).

[2] K. C. Stitely, A. Giraldo, B. Krauskopf, and S. Parkins, Nonlinear semiclassical dynamics of the unbalanced, open Dicke model, Phys. Rev. Res. **2**, 033131 (2020).

[3] H. Ritsch, P. Domokos, F. Brennecke, and T. Esslinger, Cold atoms in cavity–generated dynamical optical potentials, Rev. Mod. Phys. **85**, 553 (2013).

[4] J. Marino, M. Eckstein, M. Foster, and A.-M. Rey, Dynamical phase transitions in the collisionless pre-thermal states of isolated quantum systems: Theory and experiments, Rep. Prog. Phys. **85**, 116001 (2022).

[5] A. A. Houck, H. E. Türeci, and J. Koch, On-chip quantum simulation with superconducting circuits, Nat. Phys. **8**, 292 (2012).

[6] A. Kirilyuk, A. V. Kimel, and T. Rasing, Ultrafast optical manipulation of magnetic order, Rev. Mod. Phys. **82**, 2731 (2010).

[7] E. M. Kessler, G. Giedke, A. Imamoglu, S. F. Yelin, M. D. Lukin, and J. I. Cirac, Dissipative phase transition in a central spin system, Phys. Rev. A **86**, 012116 (2012).

[8] E. Janitz, M. K. Bhaskar, and L. Childress, Cavity quantum electrodynamics with color centers in diamond, Optica **7**, 1232 (2020).

[9] F. Mivehvar, F. Piazza, T. Donner, and H. Ritsch, Cavity qed with quantum gases: New paradigms in many-body physics, Adv. Phys. **70**, 1 (2021).

[10] R. Rosa-Medina, F. Ferri, F. Finger, N. Dogra, K. Kroeger, R. Lin, R. Chitra, T. Donner, and T. Esslinger, Observing

Dynamical Currents in a Non-Hermitian Momentum Lattice, Phys. Rev. Lett. **128**, 143602 (2022).

[11] S. P. Kelly, A. M. Rey, and J. Marino, Effect of Active Photons on Dynamical Frustration in Cavity QED, Phys. Rev. Lett. **126**, 133603 (2021).

[12] M. A. Perlin, D. Barberena, M. Mamaev, B. Sundar, R. J. Lewis-Swan, and A. M. Rey, Engineering infinite-range SU(n) interactions with spin-orbit-coupled fermions in an optical lattice, Phys. Rev. A **105**, 023326 (2022).

[13] R. Lin, R. Rosa-Medina, F. Ferri, F. Finger, K. Kroeger, T. Donner, T. Esslinger, and R. Chitra, Dissipation-Engineered Family of Nearly Dark States in Many-Body Cavity-Atom Systems, Phys. Rev. Lett. **128**, 153601 (2022).

[14] K. Seetharam, A. Lerose, R. Fazio, and J. Marino, Correlation engineering via nonlocal dissipation, Phys. Rev. Res. **4**, 013089 (2022).

[15] K. Seetharam, A. Lerose, R. Fazio, and J. Marino, Dynamical scaling of correlations generated by short- and long-range dissipation, Phys. Rev. B **105**, 184305 (2022).

[16] A. Rauschenbeutel, P. Bertet, S. Osnaghi, G. Nogues, M. Brune, J.-M. Raimond, and S. Haroche, Controlled entanglement of two field modes in a cavity quantum electrodynamics experiment, Phys. Rev. A **64**, 050301(R) (2001).

[17] M. J. Kastoryano, F. Reiter, and A. S. Sørensen, Dissipative Preparation of Entanglement in Optical Cavities, Phys. Rev. Lett. **106**, 090502 (2011).

[18] K. Baumann, C. Guerlin, F. Brennecke, and T. Esslinger, Dicke quantum phase transition with a superfluid gas in an optical cavity, Nature (London) **464**, 1301 (2010).

[19] F. Mivehvar, F. Piazza, and H. Ritsch, Disorder-Driven Density and Spin Self-Ordering of a Bose-Einstein Condensate in a Cavity, Phys. Rev. Lett. **119**, 063602 (2017).

[20] N. Dogra, M. Landini, K. Kroeger, L. Hruby, T. Donner, and T. Esslinger, Dissipation-induced structural instability and chiral dynamics in a quantum gas, Science **366**, 1496 (2019).

[21] F. Ferri, R. Rosa-Medina, F. Finger, N. Dogra, M. Soriente, O. Zilberberg, T. Donner, and T. Esslinger, Emerging Dissipative Phases in a Superradiant Quantum Gas with Tunable Decay, Phys. Rev. X **11**, 041046 (2021).

[22] F. Finger, R. Rosa-Medina, N. Reiter, P. Christodoulou, T. Donner, and T. Esslinger, Spin- and momentum-correlated atom pairs mediated by photon exchange, arXiv:2303.11326.

[23] J. D. Wilson, S. B. Jäger, J. T. Reilly, A. Shankar, M. L. Chiofalo, and M. J. Holland, Beyond one-axis twisting: Simultaneous spin-momentum squeezing, Phys. Rev. A **106**, 043711 (2022).

[24] J. J. Hauser, Magnetic proximity effect, Phys. Rev. **187**, 580 (1969).

[25] E. Saitoh, M. Ueda, H. Miyajima, and G. Tatara, Conversion of spin current into charge current at room temperature: Inverse spin–Hall effect, Appl. Phys. Lett. **88**, 182509 (2006).

[26] K. Uchida, J. Xiao, H. Adachi, J. Ohe, S. Takahashi, J. Ieda, T. Ota, Y. Kajiwara, H. Umezawa, H. Kawai, G. E. Bauer, S. Maekawa, and E. Saitoh, Spin Seebeck insulator, Nat. Mater. **9**, 894 (2010).

[27] Y. Kajiwara, K. Harii, S. Takahashi, J. Ohe, K. Uchida, M. Mizuguchi, H. Umezawa, H. Kawai, K. Ando, K. Takanashi *et al.*, Transmission of electrical signals by spin–wave interconversion in a magnetic insulator, Nature (London) **464**, 262 (2010).

[28] F. D. Czeschka, L. Dreher, M. S. Brandt, M. Weiler, M. Althammer, I.-M. Imort, G. Reiss, A. Thomas, W. Schoch, W. Limmer, H. Huebl, R. Gross, and S. T. B. Goennenwein, Scaling Behavior of the Spin Pumping Effect in Ferromagnet–Platinum Bilayers, Phys. Rev. Lett. **107**, 046601 (2011).

[29] S. Y. Huang, X. Fan, D. Qu, Y. P. Chen, W. G. Wang, J. Wu, T. Y. Chen, J. Q. Xiao, and C. L. Chien, Transport Magnetic Proximity Effects in Platinum, Phys. Rev. Lett. **109**, 107204 (2012).

[30] M. Althammer, S. Meyer, H. Nakayama, M. Schreier, S. Altmannshofer, M. Weiler, H. Huebl, S. Geprägs, M. Opel, R. Gross, D. Meier, C. Klewe, T. Kuschel, J.-M. Schmalhorst, G. Reiss, L. Shen, A. Gupta, Y.-T. Chen, G. E. W. Bauer, E. Saitoh *et al.*, Quantitative study of the spin Hall magnetoresistance in ferromagnetic insulator/normal metal hybrids, Phys. Rev. B **87**, 224401 (2013).

[31] T. Lin, C. Tang, and J. Shi, Induced magneto–transport properties at palladium/yttrium iron garnet interface, Appl. Phys. Lett. **103**, 132407 (2013).

[32] C. Hahn, G. de Loubens, O. Klein, M. Viret, V. V. Naletov, and J. Ben Youssef, Comparative measurements of inverse spin Hall effects and magnetoresistance in YIG/Pt and YIG/Ta, Phys. Rev. B **87**, 174417 (2013).

[33] C. Kittel and C. Y. Fong, *Quantum Theory of Solids* (Wiley, New York, 1963), Vol. 5.

[34] M. I. Dyakonov and V. Perel, Current–induced spin orientation of electrons in semiconductors, Phys. Lett. A **35**, 459 (1971).

[35] S. O. Demokritov, V. E. Demidov, O. Dzyapko, G. A. Melkov, A. A. Serga, B. Hillebrands, and A. N. Slavin, Bose–Einstein condensation of quasi–equilibrium magnons at room temperature under pumping, Nature (London) **443**, 430 (2006).

[36] V. E. Demidov, O. Dzyapko, S. O. Demokritov, G. A. Melkov, and A. N. Slavin, Observation of Spontaneous Coherence in Bose–Einstein Condensate of Magnons, Phys. Rev. Lett. **100**, 047205 (2008).

[37] R. A. Duine, A. Brataas, S. A. Bender, and Y. Tserkovnyak, Spintronics and magnon Bose–Einstein condensation, in *Universal Themes of Bose–Einstein Condensation*, edited by N. P. Proukakis, D. W. Snoke, and P. B. Littlewood (Cambridge University Press, Cambridge, 2017), p. 505-524.

[38] T. Giamarchi, C. Rüegg, and O. Tchernyshyov, Bose–Einstein condensation in magnetic insulators, Nat. Phys. **4**, 198 (2008).

[39] L. Berger, Emission of spin waves by a magnetic multilayer traversed by a current, Phys. Rev. B **54**, 9353 (1996).

[40] Y. M. Bunkov and G. E. Volovik, Magnon Condensation into a Q Ball in ^{3}He -B, Phys. Rev. Lett. **98**, 265302 (2007).

[41] Y. M. Bunkov and G. E. Volovik, Bose–Einstein condensation of magnons in superfluid ^{3}He, J Low. Temp. Phys. **150**, 135 (2008).

[42] S. A. Bender, R. A. Duine, and Y. Tserkovnyak, Electronic Pumping of Quasiequilibrium Bose–Einstein–Condensed Magnons, Phys. Rev. Lett. **108**, 246601 (2012).

[43] S. A. Bender, R. A. Duine, A. Brataas, and Y. Tserkovnyak, Dynamic phase diagram of dc–pumped magnon condensates, Phys. Rev. B **90**, 094409 (2014).

[44] E. L. Fjærbu, N. Rohling, and A. Brataas, Electrically driven Bose–Einstein condensation of magnons in antiferromagnets, Phys. Rev. B **95**, 144408 (2017).

[45] S. Takei, Spin transport in an electrically driven magnon gas near Bose-Einstein condensation: Hartree–Fock–Keldysh theory, Phys. Rev. B **100**, 134440 (2019).
[46] T. Wimmer, M. Althammer, L. Liensberger, N. Vlietstra, S. Geprägs, M. Weiler, R. Gross, and H. Huebl, Spin Transport in a Magnetic Insulator with Zero Effective Damping, Phys. Rev. Lett. **123**, 257201 (2019).
[47] C. Hurd, *The Hall Effect in Metals and Alloys* (Springer Science & Business Media, New York, NY, 2012).
[48] J. E. Hirsch, Spin Hall Effect, Phys. Rev. Lett. **83**, 1834 (1999).
[49] Y. K. Kato, R. C. Myers, A. C. Gossard, and D. D. Awschalom, Observation of the spin Hall effect in semiconductors, Science **306**, 1910 (2004).
[50] V. Sih, R. Myers, Y. Kato, W. Lau, A. Gossard, and D. Awschalom, Spatial imaging of the spin Hall effect and current–induced polarization in two–dimensional electron gases, Nat. Phys. **1**, 31 (2005).
[51] J. Wunderlich, B. Kaestner, J. Sinova, and T. Jungwirth, Experimental Observation of the Spin–Hall Effect in a Two–Dimensional Spin–Orbit Coupled Semiconductor System, Phys. Rev. Lett. **94**, 047204 (2005).
[52] S. O. Valenzuela and M. Tinkham, Direct electronic measurement of the spin Hall effect, Nature (London) **442**, 176 (2006).
[53] J. C. Slonczewski, Current-driven excitation of magnetic multilayers, J. Magn. Magn. Mater. **159**, L1 (1996).
[54] D. C. Ralph and M. D. Stiles, Spin transfer torques, J. Magn. Magn. Mater. **320**, 1190 (2008).
[55] Y. Tserkovnyak and S. A. Bender, Spin Hall phenomenology of magnetic dynamics, Phys. Rev. B **90**, 014428 (2014).
[56] B. Flebus, S. A. Bender, Y. Tserkovnyak, and R. A. Duine, Two-Fluid Theory for Spin Superfluidity in Magnetic Insulators, Phys. Rev. Lett. **116**, 117201 (2016).
[57] P. Kirton, M. M. Roses, J. Keeling, and E. G. Dalla Torre, Introduction to the Dicke model: From equilibrium to nonequilibrium, and vice versa, Adv. Quantum Technol. **2**, 1800043 (2019).
[58] C. Emary and T. Brandes, Chaos and the quantum phase transition in the Dicke model, Phys. Rev. E **67**, 066203 (2003).
[59] M. J. Bhaseen, J. Mayoh, B. D. Simons, and J. Keeling, Dynamics of nonequilibrium Dicke models, Phys. Rev. A **85**, 013817 (2012).
[60] J. Keeling, M. J. Bhaseen, and B. D. Simons, Collective Dynamics of Bose-Einstein Condensates in Optical Cavities, Phys. Rev. Lett. **105**, 043001 (2010).
[61] F. Reiter, T. L. Nguyen, J. P. Home, and S. F. Yelin, Cooperative Breakdown of the Oscillator Blockade in the Dicke Model, Phys. Rev. Lett. **125**, 233602 (2020).
[62] H.-P. Breuer and F. Petruccione, *The Theory of Open Quantum Systems* (Oxford University Press on Demand, 2007).
[63] P. Kirton and J. Keeling, Suppressing and Restoring the Dicke Superradiance Transition by Dephasing and Decay, Phys. Rev. Lett. **118**, 123602 (2017).
[64] I. D. Mayergoyz, G. Bertotti, and C. Serpico, *Nonlinear Magnetization Dynamics in Nanosystems* (Elsevier, Oxford, 2009).
[65] T. L. Gilbert, A phenomenological theory of damping in ferromagnetic materials, IEEE Trans. Magn. **40**, 3443 (2004).
[66] N. Bode, S. V. Kusminskiy, R. Egger, and F. von Oppen, Scattering Theory of Current–Induced Forces in Mesoscopic Systems, Phys. Rev. Lett. **107**, 036804 (2011).
[67] A. Lerose, J. Marino, B. Žunkovič, A. Gambassi, and A. Silva, Chaotic Dynamical Ferromagnetic Phase Induced by Nonequilibrium Quantum Fluctuations, Phys. Rev. Lett. **120**, 130603 (2018).
[68] A. Lerose, B. Žunkovič, J. Marino, A. Gambassi, and A. Silva, Impact of nonequilibrium fluctuations on prethermal dynamical phase transitions in long-range interacting spin chains, Phys. Rev. B **99**, 045128 (2019).
[69] Emanuele G. Dalla Torre, S. Diehl, M. D. Lukin, S. Sachdev, and P. Strack, Keldysh approach for nonequilibrium phase transitions in quantum optics: Beyond the Dicke model in optical cavities, Phys. Rev. A **87**, 023831 (2013).
[70] J. Lang and F. Piazza, Critical relaxation with overdamped quasiparticles in open quantum systems, Phys. Rev. A **94**, 033628 (2016).
[71] R. H. Dicke, Coherence in spontaneous radiation processes, Phys. Rev. **93**, 99 (1954).
[72] B. M. Garraway, The Dicke model in quantum optics: Dicke model revisited, Philos. Trans. R. Soc. A **369**, 1137 (2011).
[73] A. Safavi-Naini, R. J. Lewis-Swan, J. G. Bohnet, M. Gärttner, K. A. Gilmore, J. E. Jordan, J. Cohn, J. K. Freericks, A. M. Rey, and J. J. Bollinger, Verification of a Many-Ion Simulator of the Dicke Model Through Slow Quenches Across a Phase Transition, Phys. Rev. Lett. **121**, 040503 (2018).
[74] M. A. Quiroz-Juárez, J. Chávez-Carlos, J. L. Aragón, J. G. Hirsch, and R. d. J. León-Montiel, Experimental realization of the classical Dicke model, Phys. Rev. Res. **2**, 033169 (2020).
[75] P. Kirton and J. Keeling, Superradiant and lasing states in driven–dissipative Dicke models, New J. Phys. **20**, 015009 (2018).
[76] D. Tieri, M. Xu, D. Meiser, J. Cooper, and M. Holland, Theory of the crossover from lasing to steady state superradiance, arXiv:1702.04830.
[77] W. Kopylov, M. Radonjić, T. Brandes, A. Balaž, and A. Pelster, Dissipative two–mode Tavis–Cummings model with time–delayed feedback control, Phys. Rev. A **92**, 063832 (2015).
[78] Different amplitudes of oscillations of $\langle \mathcal{S} \rangle$ spin components along the x and y directions in the presence of the Dicke-like interaction term.
[79] A. A. Serga, C. W. Sandweg, V. I. Vasyuchka, M. B. Jungfleisch, B. Hillebrands, A. Kreisel, P. Kopietz, and M. P. Kostylev, Brillouin light scattering spectroscopy of parametrically excited dipole–exchange magnons, Phys. Rev. B **86**, 134403 (2012).
[80] Y. Tserkovnyak, A. Brataas, and G. E. W. Bauer, Enhanced Gilbert Damping in Thin Ferromagnetic Films, Phys. Rev. Lett. **88**, 117601 (2002).
[81] J. Ma, X. Wang, C. P. Sun, and F. Nori, Quantum spin squeezing, Phys. Rep. **509**, 89 (2011).
[82] L. Pezze, A. Smerzi, M. K. Oberthaler, R. Schmied, and P. Treutlein, Quantum metrology with nonclassical states of atomic ensembles, Rev. Mod. Phys. **90**, 035005 (2018).
[83] M. Koppenhöfer, P. Groszkowski, H.-K. Lau, and A. A. Clerk, Dissipative superradiant spin amplifier for enhanced quantum sensing, PRX Quantum **3**, 030330 (2022).
[84] N. Shammah, S. Ahmed, N. Lambert, S. De Liberato, and F. Nori, Open quantum systems with local and collective incoherent processes: Efficient numerical simulations

using permutational invariance, Phys. Rev. A **98**, 063815 (2018).

[85] A. Lerose and S. Pappalardi, Bridging Entanglement Dynamics and Chaos in Semiclassical Systems, Phys. Rev. A **102**, 032404 (2020).

[86] J. Marino, Universality Class of Ising Critical States with Long-Range Losses, Phys. Rev. Lett. **129**, 050603 (2022).

[87] J. Zou, S. Zhang, and Y. Tserkovnyak, Bell-state generation for spin qubits via dissipative coupling, Phys. Rev. B **106**, L180406 (2022).

[88] B. Zhu, J. Marino, N. Y. Yao, M. D. Lukin, and E. A. Demler, Dicke time crystals in driven–dissipative quantum many–body systems, New J. Phys. **21**, 073028 (2019).

[89] S. P. Kelly, R. Nandkishore, and J. Marino, Exploring many-body localization in quantum systems coupled to an environment via Wegner-Wilson flows, Nucl. Phys. B **951**, 114886 (2020).

[90] L. Landau and E. Lifshitz, On the theory of the dispersion of magnetic permeability in ferromagnetic bodies, in *Perspectives in Theoretical Physics* (Pergamon, Amsterdam, 1992), pp. 51–65.

[91] T. L. Gilbert, A lagrangian formulation of the gyromagnetic equation of the magnetization field, Phys. Rev. **100**, 1243 (1955).

[92] T. Holstein and H. Primakoff, Field dependence of the intrinsic domain magnetization of a ferromagnet, Phys. Rev. **58**, 1098 (1940).

[93] G. S. Agarwal, R. R. Puri, and R. P. Singh, Atomic Schrödinger cat states, Phys. Rev. A **56**, 2249 (1997).

[94] M. Xu, Theory of steady–state superradiance, Ph.D. thesis, University of Colorado at Boulder, 2016.

[95] M. A. Norcia, R. J. Lewis-Swan, J. R. Cline, B. Zhu, A. M. Rey, and J. K. Thompson, Cavity–mediated collective spin–exchange interactions in a strontium superradiant laser, Science **361**, 259 (2018).

[96] H. Haken, Cooperative phenomena in systems far from thermal equilibrium and in nonphysical systems, Rev. Mod. Phys. **47**, 67 (1975).

[97] H. Haken, The semiclassical approach and its applications, in *Laser Theory* (Springer, Berlin, Heidelberg, 1984), pp. 173–248.

[98] J. W. Negele and H. Orland, *Quantum Many-Particle Systems* (CRC Press, Boca Raton, 2018).

[99] K. Huang, *Introduction to Statistical Physics* (Chapman and Hall/CRC, Boca Raton, FL, 2009).

[100] M. Lewenstein and L. You, Quantum Phase Diffusion of a Bose-Einstein Condensate, Phys. Rev. Lett. **77**, 3489 (1996).

[101] I. Amelio and I. Carusotto, Theory of the Coherence of Topological Lasers, Phys. Rev. X **10**, 041060 (2020).

CHAPTER 4

Exploiting spin and momentum of atoms for harnessing driven-dissipative phase transitions

In this chapter, I present publication II [2] in which we have studied dynamical phase transitions in the driven-dissipative model comprising two Dicke models with two species of spins constructed from different degrees of freedom of the same atoms. The work was inspired by the experimental realization of the driven dissipative model in the cavity QED setup, as in [33, 81]. There, two different realizations are considered, where spins are built from the momentum or hybrid spin-momentum states of atoms. Our model comprises these two implementations, resulting in a combination of two Dicke models with dependent spins. As we have shown in the paper, such dependence has a non-trivial effect when phase transition, spontaneous symmetry breaking in one model results in explicit symmetry breaking in another. Such explicit symmetry breaking results in non-stationary behaviors of particular observables, which are time-independent with the standard implementation in [33, 81].

As we conclude in the paper, there are a few more interesting features. First, there is a parameter region, in which, in the SR phase, the collective spin and momentum of atoms are entangled, and such entanglement can be time-dependent, persistently oscillating over typical timescales of the experiment. The cavity losses do not destroy entanglement in this case but rather induce a decay of high energy modes and allow the system to reach a steady state, in other words, lending the system to the state with the targeted entanglement properties. Second, cavity loss mimics the finite lifetime of the cavity photons since cavity mirrors are not perfect, and photons can escape from the cavity. Such photons can be detected through the heterodyne detection. Since the dynamics of spin and photons in the Dicke model are interdependent, such measurement gives indirect access to the dynamics of the system. As we show in the paper, it can even be a proxy of the entanglement. The great advantage of this method is that it allows for non-destructive measurement, i.e., one can trace properties of the system during the course of the dynamics without the need to reinitialize the system.

Status of the publication: This article was published in Physics. Rev. Research on August 2024 as a regular article.

Parameters	Thesis	Publication II
Dicke Coupling	g	2η, $2\eta_s$
Cavity field operator	$\hat{a}$	a_y, a_z
Cavity detuning	ω_c	ω_y, ω_z
Dissipation rates	γ_i	$2\gamma_i$
Observable	O	$\langle O \rangle$

TABLE 4.1. Notation difference between this thesis and publication II.

Note: Due to a mismatch between the notation used in different publications and this thesis, I would like to improve the readability of the publication by listing the notation changes in table 4.1.

Dynamics of spin-momentum entanglement from superradiant phase transitions

Oksana Chelpanova [1,*] Kushal Seetharam [2,3] Rodrigo Rosa-Medina [4] Nicola Reiter [4] Fabian Finger [4] Tobias Donner [4] and Jamir Marino [1]

[1]*Institut für Physik, Johannes Gutenberg-Universität Mainz, D-55099 Mainz, Germany*
[2]*Department of Electrical Engineering, Massachusetts Institute of Technologies, Cambridge, Massachusetts 02139, USA*
[3]*Department of Physics, Harvard University, Cambridge, Massachusetts 02138, USA*
[4]*Institute for Quantum Electronics, ETH Zürich, 8093 Zürich, Switzerland*

(Received 14 December 2023; accepted 26 June 2024; published 20 August 2024)

Exploring operational regimes of many-body cavity QED with multilevel atoms remains an exciting research frontier for their enhanced storage capabilities of intralevel quantum correlations. In this work, we consider an experimentally feasible many-body cavity QED model describing a four-level system, where each of those levels is formed from a combination of different spin and momentum states of ultracold atoms in a cavity. The resulting model comprises a pair of Dicke Hamiltonians constructed from pseudospin operators, effectively capturing two intertwined superradiant phase transitions. The phase diagram reveals regions featuring weak and strong entangled states of spin and momentum atomic degrees of freedom. These states exhibit different dynamical responses, ranging from slow to fast relaxation, with the added option of persistent entanglement temporal oscillations. We discuss the role of cavity losses in steering the system's dynamics into such entangled states and propose a readout scheme that leverages different light polarizations within the cavity. Our work paves the way to connect the rich variety of non-equilibrium phase transitions that occur in many-body cavity QED to the buildup of quantum correlations in systems with multilevel atom descriptions.

DOI: 10.1103/PhysRevResearch.6.033193

I. INTRODUCTION

The coupling between spin and motional degrees of freedom lies at the root of several rich phenomena in quantum physics, including fine structure splitting of atoms [1] and the spin Hall effect [2], which, in turn, allow the realization of topological phases of matter [3,4] and open the possibility of topological quantum computing [5,6]. Spin-momentum entanglement resulting from such coupling has increasingly become relevant in a variety of research areas, ranging from materials science to photonics and atomic systems [7–9]. In this work, we propose a protocol for engineering entanglement between the spin and momentum degrees of freedom of ultracold atoms coupled to an optical cavity. Our approach exploits a nonequilibrium superradiant phase transition in the system realized by coupling four atomic modes, which comprise two internal (spin) and external (momentum) states of the atom.

Many-body cavity QED experiments with ultracold atoms are among the most versatile quantum simulators of driven-dissipative phases of matter [10]. The combination of tunable photon-mediated long-range interatomic interactions, along with strong cooperative effects and control on cavity losses, offers a wide range of possibilities, encompassing nonequilibrium transitions [11–20], dynamical control of correlations [21–26], realization of dark states [27–29], and the exploration of collective phenomena purely driven by engineered dissipation [30–32]. Oftentimes, the effective atomic degrees of freedom in state-of-art experiments are a pair of momentum states or internal levels, optically addressed by external laser drives inducing cavity-assisted two-photon transitions [12,33–35]. Recently, a few cavity QED experiments and theory works have shown how to couple the momentum and internal spin degrees of freedom of ultracold atoms using intracavity light, demonstrating novel self-organized phases [11,36–39].

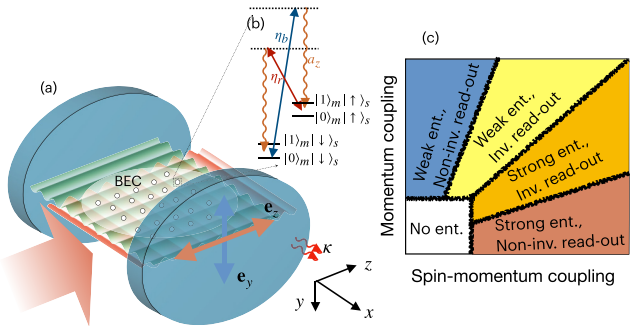

FIG. 1. (a) Sketch of the cavity QED setup and (b) of the atomic level scheme. (c) Cartoon of the dynamical phase diagram as a function of the couplings between spin and momentum degrees of freedom.

*Contact author: okchelpa@uni-mainz.de

Published by the American Physical Society under the terms of the Creative Commons Attribution 4.0 International license. Further distribution of this work must maintain attribution to the author(s) and the published article's title, journal citation, and DOI.

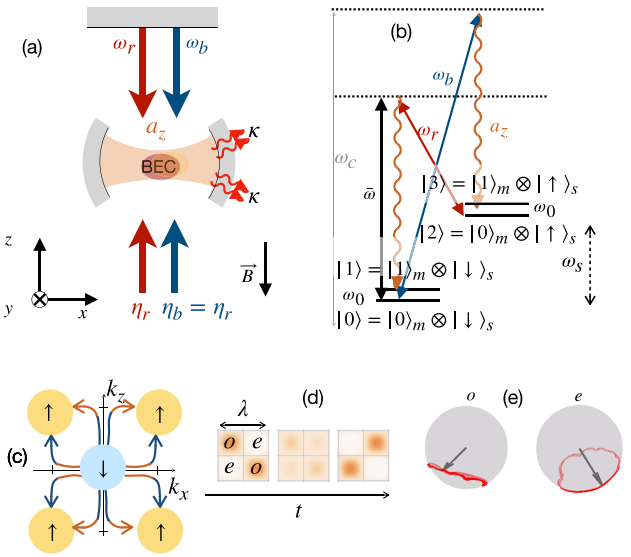

FIG. 2. (a) Schematics of the experimental setup and (b) corresponding level scheme for the model (2). (c) Momentum space cartoon for spin-flipping Raman process for a transition $|0\rangle \rightarrow |3\rangle$; (d) Snapshots of the real-space BEC density in the $|\uparrow\rangle_s$ manifold at different times; (e) dynamics in the superradiant phase of the spin components on even (e) and odd (o) lattice sites plotted on the Bloch spheres.

In this paper, we generalize such protocols to show that spin-momentum entanglement can be synthesized, controlled, and steered in experiments by coupling motional and internal degrees of freedom. We consider a cavity QED platform, cf. Fig. 1(a), which is described by a minimal model with two different spin states and two different momentum states, meaning that each atom can occupy one of these four hybrid spin-momentum states shown in Fig. 1(b). We demonstrate that this system exhibits superradiant phase transitions related to the self-organization of the atoms in the cavity, concomitantly with the dynamical buildup of spin-momentum entanglement. By varying the spin-momentum coupling, one can robustly tune the entanglement up to its maximum possible value.

The superradiant phase transitions within this model exhibit notable distinctions from the conventional phenomenology of self-organization in cavity QED [11,12,31–33,40–44]. While the hybrid spin-momentum order parameter in our system and the photon number approach stationary values, the spin and momentum separately can be nonstationary. This results in a time-dependent profile of the condensate density and the effective spin magnetization, which is unconventional for state-of-art cavity QED experiments [36,37]. Such oscillations persist beyond the operational time scales of these platforms, resulting in long-lived nonstationary dynamical responses. We show that such features can be continuously probed using an auxiliary cavity field, which is coupled to the momentum degree of freedom of atoms. The overall dynamics in such a model are conditioned by the intertwining of two cavity-mediated processes, controlled by two couplings between momentum states or hybrid momentum-spin states. The different dynamical responses of the system, summarized in Fig. 1(c), are characterized by weak or strong entanglement. In particular, despite the back-action and intrinsic decoherence of the read-out process, proxy of spin-momentum entanglement dynamics can be noninvasively accessed in an extended parameter regime [red region in Fig. 1(c)], making the system a possible candidate for quantum information applications [45].

Crucially, in our scheme, cavity losses have the beneficial role of steering dynamics towards target entangled states, thereby endowing robustness to the initial condition of the system. This feature is absent in protocols engineering spin-momentum entanglement in BECs using solely classical drive fields [8]. In such proposals, the degree of achievable spin-momentum entanglement is highly sensitive with respect to technical fluctuations of different experimental parameters (e.g., drive powers and frequencies). In contrast, protocols relying on cavity losses induce contractive dynamics which are insensitive to such issues and initial state preparation, therefore offering a more robust and reliable route for spin-momentum entanglement generation.

Outline

The paper is organized as follows. In Sec. II, we present an experimentally motivated effective model that governs the dynamics of the cavity QED setup in Fig. 1, where the spin and momentum of atoms are coupled to the cavity field. Section III is devoted to the superradiant phase transition and subsequent generation of entanglement between spin and momentum degrees of freedom. In Sec. IV, we extend the model by introducing an auxiliary cavity mode and show how it enables continuous read-out of the system dynamics. In Sec. V, we analyze the dynamical responses and read-out strategies. In Sec. VI, we revisit entanglement generation in the presence of the auxiliary cavity mode and discuss prospects for its noninvasive read-out. In the concluding Sec. VII, we summarize our findings and discuss follow-up directions.

II. MODEL

We consider a cavity QED configuration in which we can address both the spin and momentum states of ultracold atoms, enabling measurement and dynamic control (see also Ref. [36] for a related setup). Specifically, we consider Bose-Einstein condensate (BEC) of ^{87}Rb atoms in the $F = 1$ hyperfine ground state manifold confined in a high-finesse optical cavity. The atoms are coupled to a z-polarized cavity mode a_z with resonance frequency ω_c and decay rate κ, extending along x direction, as illustrated in Fig. 2(a). A bias magnetic field $\vec{B}$ along the z direction defines the quantization axis and induces Zeeman splitting between the sublevels of the $F = 1$ hyperfine manifold. We focus on two internal atomic sublevels $|m_F = 1\rangle = |\downarrow\rangle_s$ and $|m_F = 0\rangle = |\uparrow\rangle_s$ and describe the condensate with the spinor wave function $\Psi = (\psi_\uparrow, \psi_\downarrow)^T$.

The condensate is illuminated with transverse standing-wave laser fields far-detuned from the electronic transitions of the atoms. These detunings allow us to effectively eliminate the contribution of excited electronic states and to focus on the near-resonant cavity-assisted two-photon transitions between an atomic momentum state $|0\rangle_m = |k_x = 0, k_z = 0\rangle$

and an excited one, which reads as a coherent superposition $|1\rangle_m = \sum_{s,s'=\pm} |k_x = sk, k_z = s'k\rangle/2$. Here, $\hbar k = 2\pi\hbar/\lambda$ indicates the recoil momentum, with $\lambda/2 = 784.7/2$ nm representing the period of the standing-wave potential along the drive direction.

We introduce the following definitions of relevant combinations of momentum and spin states [cf. Fig. 2(b)]

$$\begin{aligned} |0\rangle &= |0\rangle_m \otimes |\downarrow\rangle_s, \\ |1\rangle &= |1\rangle_m \otimes |\downarrow\rangle_s, \\ |2\rangle &= |0\rangle_m \otimes |\uparrow\rangle_s, \\ |3\rangle &= |1\rangle_m \otimes |\uparrow\rangle_s, \end{aligned} \tag{1}$$

limiting our consideration to a four-level model of the system, which will be further justified in the following. In this notation, even states $|0\rangle$ and $|2\rangle$ are momentum ground states that correspond to the homogeneous condensate density in real space, while odd states $|1\rangle$ and $|3\rangle$ are excited momentum states and correspond to a modulation of the atomic density in real space: $|1\rangle_m \propto \cos kx \cos kz$ (see also Ref. [12]). We also introduce boson annihilation and creation operators $c_{0,\ldots,3}$, $c^\dagger_{0,\ldots,3}$, $[c_i, c_j^\dagger] = \delta_{i,j}$, which describe the annihilation and creation of a particle in these four state manifold of Eqs. (1).

We consider Raman processes that simultaneously couple internal (spin) and external (momentum) atomic degrees of freedom [36,37,46]. These processes are mediated by the interaction of the cavity mode a_z and two classical driving fields with coupling strength $\eta_b = \eta_r = \eta$ and frequencies ω_b, ω_r, with $2\bar{\omega} = \omega_b + \omega_r$, $\delta = \omega_b - \omega_r$. In this context, the laser at frequency ω_b facilitates the transition between states $|0\rangle$ and $|3\rangle$, from the ground momentum state $|0\rangle_m$ to the excited momentum state $|1\rangle_m$, accompanied by a spin flip from $|\downarrow\rangle_s$ to $|\uparrow\rangle_s$ and vise versa. Conversely, the laser at frequency ω_r induces a similar transition, $|2\rangle \leftrightarrow |1\rangle$, accompanied by a spin flip from $|\uparrow\rangle_s$ to $|\downarrow\rangle_s$, cf. Figs. 2(b) and 2(c). These two cavity-assisted Raman processes mediate an interaction of the form $\eta(a_z + a_z^\dagger)\cos kx \cos kz(F^+ + F^-)$, where the spin operators $F^\pm$ couple neighboring spin levels [cf. momentum cartoon in Fig. 2(c) and Appendix A for the model details]. After integrating over the spatial extent of the condensate, the Hamiltonian of the effective model reads

$$\begin{aligned} H =& \omega_z a_z^\dagger a_z + (\omega_0 - \omega_s)S^z_{12} + (\omega_0 + \omega_s)S^z_{03} \\ &+ 2\eta(a_z + a_z^\dagger)\big(S^x_{12} + S^x_{03}\big), \end{aligned} \tag{2}$$

where ω_z is the cavity detuning (cf. Appendix A), ω_0 is the double recoil energy $\omega_{\rm rec} = k^2/(2M)$, which atoms acquire in the two-photon process, and ω_s is the effective splitting between the two spin manifolds. We set $\hbar = 1$ to keep the notation compact.

The cavity boson field a_z satisfies the commutation relations $[a_z, a_z] = 0$, $[a_z, a_z^\dagger] = 1$. The collective pseudospin operators S are built as projectors between the macroscopically occupied spin-momentum levels $S^-_{ij} = |i\rangle\langle j| = c_i^\dagger c_j$, $S^+_{ij} = (S^-_{ij})^\dagger$, $S^z_{ij} = (c_j^\dagger c_j - c_i^\dagger c_i)/2$, $S^x_{ij} = (S^-_{ij} + S^+_{ij})/2$with $(i, j) \in \{(0, 3), (1, 2)\}$ for $i = 0, \ldots, 3 < j$. Here, we already rescaled spin and photon operators via $S \to S/N$, $a_z \to a_z/\sqrt{N}$ (and also $c_i \to c_i/\sqrt{N}$) as it is convenient for collective spin models [44,47], where N is a number of atoms in the condensate. Similarly, one can introduce other pseudospin operators $\mathcal{T}$, that are built from different spin states of the same momentum: $\mathcal{T}^-_{ij} = c_i^\dagger c_j, \ldots$, where $(i, j) \in \{(0, 2), (1, 3)\}$, or when $(i, j) \in \{(0, 1), (2, 3)\}$ pseudospin operators $J^-_{ij} = c_i^\dagger c_j$ correspond to transitions between different momentum states of the same internal spin.

The dynamics of the system are described by the Lindblad master equation for the density matrix ρ

$$\begin{aligned} \frac{d}{dt}\rho &= -i[H, \rho] + \kappa\mathcal{D}(\rho), \\ \mathcal{D}(\rho) &= 2a_z\rho a_z^\dagger - \{a_z^\dagger a_z, \rho\}, \end{aligned} \tag{3}$$

where cavity losses account for the finite lifetime $\propto 1/\kappa$ of the cavity photon a_z.

Our proposal is inspired by the experiments reported in Refs. [11,36] that typically involve a substantial number of atoms, around $N \approx 10^4$–10^5, and deviations from mean-field behavior only become pronounced at extremely long timescales. The coupling between photons and atoms is collective [cf. Eq. (2)], and results in a suppression of light-matter correlations by a factor of $1/N$. The dynamics are thus well captured by mean-field equations of motion, which we report in Appendix B for completeness. However, correlations between the spin and momentum degrees of freedom within the condensate play a significant role in entanglement dynamics, as we show in detail in the following section.

The dynamics in Eq. (3) possess a $\mathbb{Z}_2$ symmetry characteristic of Dicke models [33,36,37,48,49]: it is invariant under the transformation $(a_z, S^x) \leftrightarrow (-a_z, -S^x)$, where $S^x = S^x_{03} + S^x_{12}$ [cf. Eq. (2)]. When this symmetry is spontaneously broken, the system undergoes a phase transition. In the thermodynamic limit, the transition can shift the system from the trivial normal state with the empty cavity mode $n_z = \langle a_z^\dagger a_z\rangle = |\langle a_z\rangle|^2 = 0$ and all spins polarized along the z direction to the superradiant (SR) phase with the nonzero occupation of the cavity mode and finite x component of the spin, namely $n_z \neq 0$ and $\langle S^x\rangle \neq 0$ (cf. Appendix D or Ref. [44] for more details). Throughout this paper, we employ $\langle\cdot\rangle$ to denote expectation values of observables.

When $\omega_s = 0$, the critical coupling at which the transition to the SR phase takes place read $\eta^c_{\omega_s=0} = [\omega_0(\omega_z^2 + \kappa^2)/(4\omega_z)]^{1/2}$ [48,50], while for $\omega_s \neq 0$ case, the critical coupling becomes sensitive to the initial conditions. This sensitivity is rooted in the different effective level splitting for pseudospins S_{03} and S_{12}, $\omega_0 \pm \omega_s$. The specific distribution of particles between the two pseudospins, S_{03} and S_{12}, gives rise to distinct effective level splittings between excited and ground momentum states and thus different critical couplings. A similar dependence on the initial state also emerges when there is disorder in the coupling constants, as discussed in Refs. [51,52].

To illustrate this dependence, consider initialization of the system in a mixture of the atoms in the ground momentum state, $|k_x, k_z\rangle = |0\rangle_m$, with two different magnetic numbers; namely, we prepare $N_0 = N\langle c_0^\dagger c_0\rangle = \mu N$ particles in level $|0\rangle$ and $N_2 = N\langle c_2^\dagger c_2\rangle = (1 - \mu)N$ particles in level $|2\rangle$, where $\mu \in [0, 1]$. This results in the critical coupling (see

Appendix D)

$$2\eta^c = \begin{cases} \sqrt{\frac{(\omega_0^2-\omega_s^2)(\omega_z^2+\kappa^2)/\omega_z}{(\omega_s+\omega_0)-2\mu\omega_s}}, & \omega_s < \omega_0, \\ \sqrt{\frac{(\omega_s^2-\omega_0^2)(\omega_z^2+\kappa^2)/\omega_z}{(\omega_s+\omega_0)-2\mu\omega_0}}, & \omega_s > \omega_0. \end{cases} \tag{4}$$

If the system is prepared in the spin-polarized state, the expression for the critical coupling simplifies to $2\eta_c = [(\omega_0 \pm \omega_s)(\omega_z^2+\kappa^2)/\omega_z]^{1/2}$ for $\mu = 0, 1$, coinciding with the critical coupling in Ref. [53].

In order to study, the onset of the SR phase on a microscopic level, we evaluate the condensate $|\psi_{\uparrow,\downarrow}|^2$ and the spin $\Psi^\dagger\sigma^i\Psi/2$ densities. Here, we use spin-1/2 Pauli matrices σ^i instead of spin operators F of the original problem to highlight the two-level internal spin structure of the effective model. The spinor $\Psi = (\psi_\uparrow, \psi_\downarrow)^T$ has components $\psi_\downarrow = \langle c_0\rangle + \langle c_1\rangle \cos kx \cos kz$, and $\psi_\uparrow = \langle c_2\rangle + \langle c_3\rangle \cos kx \cos kz$, cf. Appendix A.

When $\mu \in (0, 1)$, both spin and condensate density are time dependent. We show a few snapshots of the condensate density at different times in Fig. 2(d) along with the spin for even and odd sites [Fig. 2(e); spin components are evaluated in the center of lattice cells of the size $\lambda/2 \times \lambda/2$]. We explain such time-dependence from the fact that the correct order parameter that captures transition to the superradiant phase is the spin density integrated over the space, $\int d\mathbf{r}\Psi^\dagger\sigma^x\Psi \cos kx \cos kz$ (see derivation of the Hamiltonian in Appendix A). On the other hand, the x component of spatial spin profile (spin density) contains a time-independent contribution $\propto \mathrm{Re}(\langle c_0^\dagger c_3\rangle + \langle c_2^\dagger c_1\rangle) \cos kx \cos kz \propto (\langle S_{03}^x\rangle + \langle S_{12}^x\rangle) \cos kx \cos kz$, which exactly reflects spontaneous breaking of the $\mathbb{Z}_2$ symmetry, and a time-dependent contribution of the form $\propto \mathrm{Re}(\langle c_2^\dagger c_0\rangle + \langle c_3^\dagger c_1\rangle \cos^2 kx \cos^2 kz) \propto (\langle \mathcal{T}_{02}^x\rangle + \langle \mathcal{T}_{13}\rangle^x \cos^2 kx \cos^2 kz)$. Here, both $\langle \mathcal{T}^x(t)\rangle \propto \cos(\Omega t)$ [cf. expression for Ω in Appendix D] and are zero only if $\mu = 0$ or $\mu = 1$ (this particular case has been studied in Refs. [36,37]). Such precession of $\langle \mathcal{T}\rangle$ originates from the fact that pseudospin species S, $\mathcal{T}$ and J are built as bilinears of the same boson operators $c_0, \ldots, c_3$. Similarly, the total density $|\psi_\downarrow|^2 + |\psi_\uparrow|^2$ contains time-dependent contribution of the form $(\langle c_0^\dagger c_1\rangle + \langle c_2^\dagger c_3\rangle + \langle c_1^\dagger c_0\rangle + \langle c_3^\dagger c_2\rangle) \cos kx \cos kz \propto (\langle J_{01}^x\rangle + \langle J_{23}^x\rangle) \cos kx \cos kz$ which vanishes only if $\mu = 0, 1$. Otherwise, the spin and density distribution along the lattice are time-dependent. In the following section, we show the impact of such time dependence on the dynamics of entanglement between spin and momentum degrees of freedom.

Following experiments in Refs. [11,36], we maintain the key parameters $\omega_0/(2\pi) \approx 7.4$ kHz and $\kappa/(2\pi) = 1.25$ MHz fixed for all simulations. The remaining detunings and coupling strengths are tunable, allowing for the exploration of a broad spectrum of dynamical regimes.

III. SPIN-MOMENTUM ENTANGLEMENT AND SUPERRADIANT DYNAMICS

Although correlations among different atoms are negligible, our platform offers a route to engineer robust entanglement between spin and momentum degrees of freedom within the bosonic condensate trapped in the cavity. For instance, assume all atoms are initially prepared in the state $|0\rangle = |0\rangle_m \otimes |\downarrow\rangle_s$. Through the interaction with the cavity mode a_z, the atoms are coupled to the state $|3\rangle = |1\rangle_m \otimes |\uparrow\rangle_s$ as $2\eta(a_z + a_z^\dagger)S_{03}^x|0\rangle = \eta(a_z + a_z^\dagger)|3\rangle$. Thus, in the SR phase with the nonzero cavity field ($\langle a_z\rangle \neq 0$), the cavity-mediated interaction gives rise to a nonseparable spin-momentum state. The corresponding state of each atom reads

$$|\psi\rangle = \langle c_0\rangle|0\rangle_m \otimes |\downarrow\rangle_s + \langle c_3\rangle|1\rangle_m \otimes |\uparrow\rangle_s, \tag{5}$$

with $\langle c_0\rangle \neq 0$ and $\langle c_3\rangle \neq 0$, and $|\psi\rangle$ is a nonseparable entangled state of spin and momentum. Our results will revolve around the dynamical manipulation of this form of entanglement.

In order to quantify spin-momentum entanglement, we use the von Neumann entropy

$$S_{\mathrm{vN}} = -\mathrm{Tr}(\tilde{\rho}\log_2\tilde{\rho}) \tag{6}$$

with $\tilde{\rho}$ the reduced density matrix after tracing out spin or momentum states, cf. Appendix E. When the system is in a product state of spin and momentum, the entanglement vanishes and $S_{\mathrm{vN}} = 0$. With the definition in Eq. (6), a maximally entangled state has $S_{\mathrm{vN}} = 1$. We also compute negativity [54] and concurrence [55,56], which are more reliable witnesses of entanglement in open systems [57]. However, they show the same qualitative behavior as S_{vN} (cf. Appendix E), and thus we restrict our analysis to the von Neumann entropy for its simplicity.

By adjusting coupling η and the initial state of atoms, we compute a dynamical phase diagram, which captures maximal S_{vN} reached during evolution, see Fig. 3. The system is initially prepared in the normal state with $N_0 = \mu N$ atoms in the state $|0\rangle$, after which we rapidly increase the coupling η to a specified value. The equations of motion describing this process can be found in Appendices B and C. Note that the collective description of the model, adapted in this work, is valid only when the system is prepared in the permutation invariant state; otherwise, dynamics become more complicated as discussed in Refs. [58–61]. Below, we analyze the entanglement properties for both the degenerate case ($\omega_s = 0$) and the nondegenerate case ($\omega_s \neq 0$), showcasing the potential for achieving either a stationary or a time oscillating amount of entanglement, respectively.

1. Degenerate $\omega_s = 0$ case

The amount of S_{vN} reached during dynamics in the degenerate case is shown in Fig. 3(a). Depending on the initial configuration, the maximum amount of entanglement in the system can vary from $\max(S_{\mathrm{vN}}) = 0$ to $\max(S_{\mathrm{vN}}) = 1$. Specifically, when $\mu = 0.5$, the momentum configuration of each spin component reads exactly the same, and the state becomes separable. Conversely, when $\mu = 0$ or 1, one can reach a maximally entangled state; the dependence of the entanglement in the system as a function of μ is shown with blue lines in Fig. 3(c). On the other hand, the amount of entanglement in the SR phase depends on the coupling η, [cf. dependence of the entanglement entropy as a function of coupling for $\mu = 0$ in panel (d), blue lines]. Here, entanglement increases with the coupling which can be qualitatively understood as follows. When $\eta \approx \eta^c$, almost all atoms occupy the ground momentum state and $|\psi\rangle \propto |2\rangle$, which is separable in terms

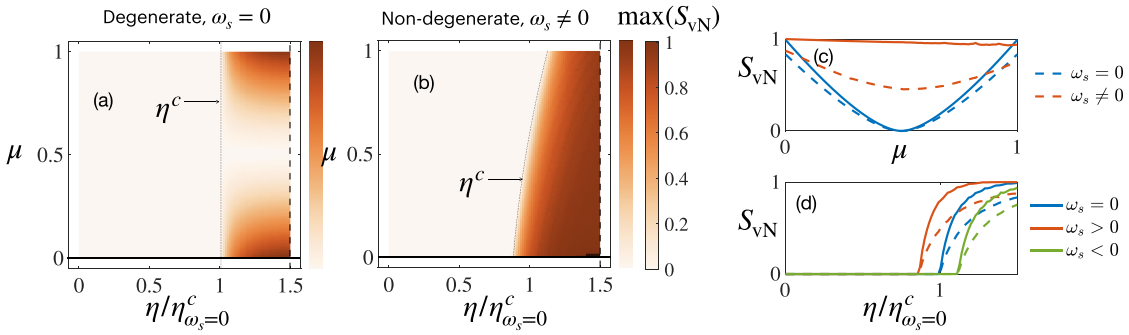

FIG. 3. [(a) and (b)] Maximum of spin-momentum entanglement $S_{\rm vN}$ as a function of $\eta/\eta^c_{\omega_s=0}$ and μ. Entanglement is built up as we enter the superradiant phase. Here (a) $\omega_s = 0$ and (b) $\omega_s = \omega_0/4$. (c) Maximal (solid lines) and time-averaged (dashed lines) entanglement entropy as a function of μ for different values of ω_s and $\eta/\eta^c_{\omega_s=0} = 1.5$. (d) Maximal (solid lines) and time-averaged (dashed lines) entanglement entropy as a function of photon-matter coupling η for $\mu = 0$. Different colors indicate different ω_s.

of spin and momentum. However, as we increase coupling, the population of the excited momentum level $|1\rangle$ increases and the spin-momentum state of the system becomes nonseparable, approaching a maximally entangled state deep in the SR phase. Importantly, by solving the dynamics of the system without cutting off the higher momentum state, we check that for large couplings, most of the atoms occupy momentum states $|0\rangle_m$, $|1\rangle_m$. The states $|0, 2k\rangle$ and $|2k, 0\rangle$ are significantly less populated during the dynamics, and we can neglect them. The corresponding equations of motion are given in Appendix B.

2. *Nondegenerate $\omega_s \neq 0$ case*

When $\omega_s \neq 0$, the dynamical behavior of the entanglement entropy changes compared to the degenerate case [see Fig. 3(b)]. First, the critical coupling depends on μ, cf. Eq. (4). Second, when $\mu = 0.5$, entanglement decreases but does not disappear completely [red lines in panel (c)]. Here, one can notice the difference between the maximal value of the entanglement (dashed line) and the period-averaged value (solid line), indicating an oscillatory behavior in time. The exceptional case are $\mu = 0, 1$ where the system evolves towards a stationary SR state. From the standpoint of spin-momentum correlations, these two states has maximum (nonoscillatory) entanglement when compared with occurrences at other values of μ.

Figure 4 depicts the dynamics of the entanglement entropy in the nondegenerate case after the quench during the period (a), along with the (b) occupation of the cavity field n_z and [(c) and (d)] spin (arrows) and density distributions of atoms. In panels (c) and (d) with arrows, we plot the projection of this spin density on the xz plane, evaluated in the center of each lattice cell of size $\lambda/2 \times \lambda/2$, which is formed by the interference of the laser and cavity fields.

In Fig. 4, maximally entangled configurations correspond to the case when the checkerboard lattice is formed by the spin degree of freedom (arrows), while the condensate density is periodically modulated with the period $\lambda/2$. On the contrary, in the configuration with vanishing entanglement, the sign of the spin projection $\Psi\sigma^x\Psi$ is fixed for all lattice cells, and the condensate density modulation occurs with a period λ. Such dynamics persist in time without any sign of relaxation (see Appendices B and D for more details).

Such dynamical behavior emerges from the time-dependent components of spin and condensate densities, if the system is initialized in the mixed internal spin state. While the total atom number $\int d\mathbf{r}|\Psi|^2 = N$, and transverse magnetization $\int d\mathbf{r}\Psi^\dagger\sigma^x\Psi/N \propto \langle S^x\rangle$, are conserved quantities in the steady state, their local distributions can exhibit complicated time dependence, driven by the precession of pseudospins $\langle J\rangle$ and $\langle \mathcal{T}\rangle$: when $\langle J^x\rangle$ and $\langle \mathcal{T}^x\rangle$ reach zero, the local distribution of spin and condensate densities are identical to the one obtained starting from the polarized spin state, and the entanglement entropy becomes maximal. When $\langle J^x\rangle$ and $\langle \mathcal{T}^x\rangle$ deviate from zero, the distribution of atoms among space and spin levels changes, decreasing the entanglement entropy. Thus the time dependence of spin and momentum states results in oscillations of the entanglement entropy. This is one of the striking features of our quench protocol: we can steer entanglement dynamics toward an oscillatory regime that persists up to the operational timescales of the experiment.

Notice that entanglement is generated during dynamics starting from product spin-momentum states, and thus, the cavity photon has an active role in building spin-momentum correlations via light-induced interactions. The nonzero cavity field $\langle a_z\rangle$ in the SR phase mediates an effective interaction among atoms, which is responsible for entangling them in a nonseparable spin-momentum state. At the same time, the role of cavity losses is essential. They steer dynamics towards the fixed point of the Lindbladian, with the remarkable consequence that all entanglement properties derived in the presence of photon losses are robust if compared with what would be achieved with a coherent drive [8,62,63]. For instance, by replacing the cavity field with a time-dependent drive in H [Eq. (2)], one could also entangle spin and momentum degrees of freedom of the condensate's atoms. However, the amount of final entanglement produced would depend on details of the driving protocol, such as its duration, frequency decomposition, and other specifics. More importantly, such entanglement would be highly sensitive to noise and imperfections in the drive realization [64–66]. In contrast, cavity losses induce relaxation of atomic entanglement towards a steady state that remains resilient even for moderate imperfections in the initial state preparation or in the parameters set to drive dynamics into superradiance. In other words, there

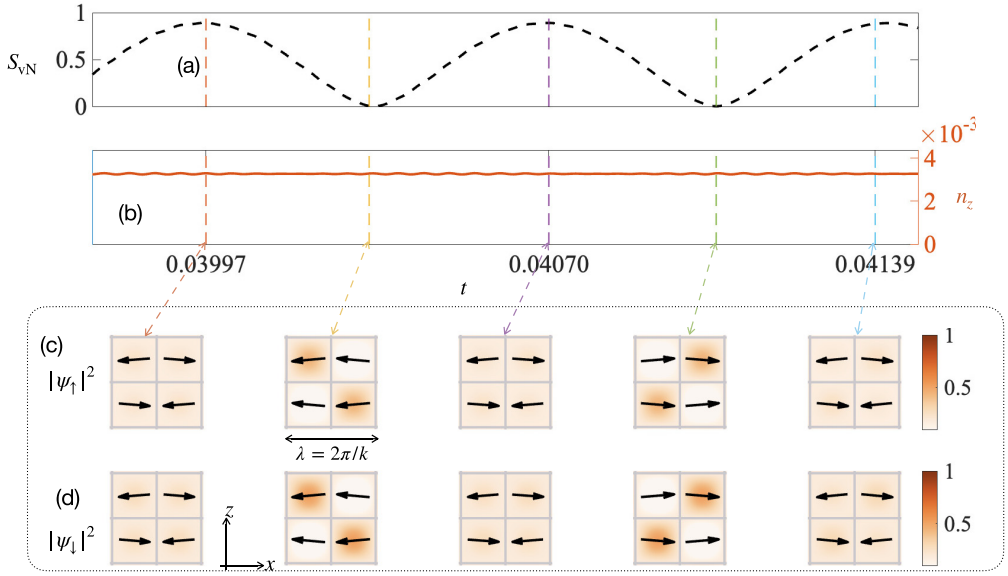

FIG. 4. (a) Dynamics of entanglement, (b) occupation of the cavity mode a_z, $n_z = \langle a_z^\dagger a_z \rangle$, density of the (c) upper $|\psi_\uparrow|^2$ and (d) lower $|\psi_\downarrow|^2$ spinor components. Black arrows in panels (c)-(d) indicate local spin texture $\Psi^\dagger \sigma^i \Psi/2$, evaluated in the centers of each cell and projected onto the xz plane. Dashed lines indicate time moments when the entropy takes extremum values and is added to guide the eye. Entropy is maximized when the state $|\psi\rangle$ is a nonseparable combination of two spin-momentum states, and SR manifests as a spin checkerboard lattice, i.e., projection of spin onto x axis takes opposite signs on even and odd lattice cells. When entanglement vanishes, both spinor components have similar density profiles and the sign of projection of the spin magnetization onto the x axis. Dynamics are simulated for $\mu = 0.5$, $\eta = 1.6\eta^c$, $\omega_s = \omega_0/4$, $\omega_z = \kappa$.

exists a broad basin of attraction towards prescribed values of entanglement given the system's initial conditions parameters.

IV. TWO CAVITY FIELDS SETUP AND PROBES OF MOMENTUM STATES

In the previous section, we have shown that cavity dissipation can be utilized to prepare the system in a steady state with desired entanglement properties. In the following sections, we show how, by using the auxiliary polarization mode a_y of the cavity field, one can get access to the collective momentum state of the system in a nondestructive fashion.

Inspired by the experimental demonstrations in Refs. [11,12], we consider a driving scheme that enables effective coupling of ground and excited atomic momentum states. We consider a cavity-assisted Bragg process involving the transverse driving field with amplitude η_s and frequency $\bar{\omega}$ and the cavity mode a_y with detuning ω_y, decay rate κ, and linear polarization along y [see Figs. 5(a) and 5(b)]. This process is reflected in the atom-cavity interaction term, $\propto \eta_s(a_y + a_y^\dagger)\cos kx \cos kz$ (cf. Appendix A). In this two-photon process, atoms initialized in the ground momentum state $|0\rangle_m$ can be excited to the momentum state $|1\rangle_m$, while the internal spin state ($|\downarrow\rangle_s$ or $|\uparrow\rangle_s$) remains unchanged [cf. Fig. 5(c)]. The schematics of this process are encoded in the Dicke Hamiltonian (see Appendix A)

$$H_s = \omega_y a_y^\dagger a_y + \omega_0\left(J_{01}^z + J_{23}^z\right) + 2\eta_s(a_y + a_y^\dagger)\left(J_{01}^x + J_{23}^x\right). \tag{7}$$

Depending on the coupling η_s, the system undergoes a phase transition associated with the spontaneous breaking of the $\mathbb{Z}_2$ symmetry of the Hamiltonian H_s, such that the Hamiltonian is invariant under the transformation $(a_y, J^x) \leftrightarrow (-a_y, -J^x)$. When the coupling is below the critical value $\eta_s < \eta_s^c = [(\omega_y^2 + \kappa^2)\omega_0^2/(4\omega_y)]^{1/2}$, the system is in the normal phase where only ground momentum states are occupied, and, respectively, $\langle J_{01}^z \rangle + \langle J_{23}^z \rangle = -1/2$, $\langle J_{01}^x \rangle = \langle J_{23}^x \rangle = 0$, and the cavity is empty, $n_y = \langle a_y^\dagger a_y \rangle = |\langle a_y \rangle|^2 = 0$ (see Appendix D for more details). In this phase, the condensate is homogeneously distributed within the trap without a checkerboardlike density modulation. When $\eta_s > \eta_s^c$, the system enters a $\mathbb{Z}_2$ symmetry-broken superradiant phase with $\langle J^x \rangle \neq 0$ and $n_y \neq 0$.

On a microscopic level, in the SR phase, the standing-wave driving field and the cavity field form an interference lattice potential $V \propto \cos kx \cos kz$, and the condensate density is modulated, forming the checkerboard lattice with the period $\lambda = 2\pi/k$, see Fig. 5(d). The density modulation originates from the condensate wave function in each spinor component. At the same time, as it is shown in Fig. 5(e), the internal spin $\Psi^\dagger \sigma^i \Psi/2$ also precesses according to the model (7) with the amplitude $\propto \sqrt{\mu(1-\mu)}$ and frequency $\propto 2\omega_s$ (see Appendix D).

The interaction term in Eq. (7) couples different atomic momentum states within the same spin manifold and does not generate entanglement between spin and momentum. Precisely, in the SR phase, the momentum configuration reads exactly the same for each spin manifold $|\uparrow\rangle_s$ and $|\downarrow\rangle_s$, and the state is separable. However, as we show below, competition between H and H_s results in a rich manifold of dynamical responses, which can be probed in a nondestructive way by analyzing the light that leaks out of the cavity [67]. As we report further in the text, by tuning η and η_s, it is possible to monitor the spin-momentum entanglement generated by η

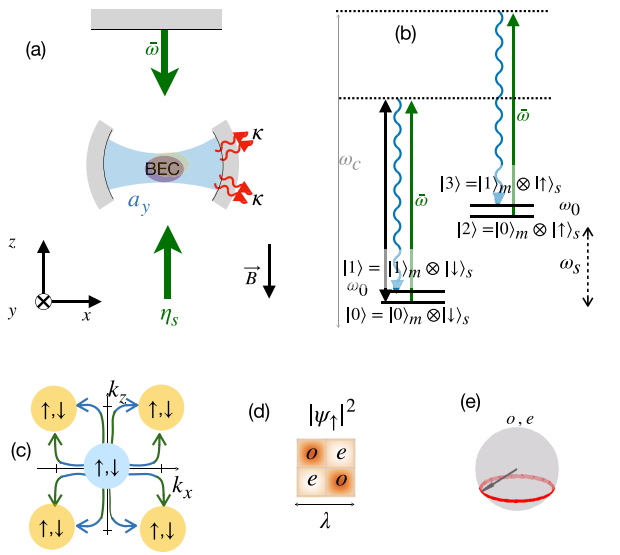

FIG. 5. (a) Schematics of the experimental setup and (b) corresponding level scheme for the model (7). (c) Momentum space cartoon for the spin-preserving Bragg process; (d) steady-state density of the condensate in the SR phase; and (e) internal spin precession described by the Hamiltonian H_s. Here, spontaneous symmetry breaking in H_s results in a density checkerboard modulation.

in a noninvasive manner. This means that such monitoring can be achieved without substantially altering the underlying dynamics of entanglement entropy.

Intertwined spin and momentum dynamics

The Hamiltonian describing the interaction of the two cavity modes with different polarizations and four spin-momentum levels reads

$$H_{\rm tot} = H + H_s - \omega_0\big(J^z_{01} + J^z_{23}\big), \tag{8}$$

where the term H_s [Eq. (7)] describes transitions in the momentum degrees of freedom, while H [Eq. (2)] describes transitions simultaneously in momentum and spin degrees of freedom. Here, we subtract the $\omega_0 J^z$ term since it is already included in both H and H_s, see derivation in Appendix A. The overall dynamics of this open system are governed by the Lindblad master equation

$$\begin{aligned}\frac{d}{dt}\rho &= -i[H_{\rm tot},\rho] + \kappa\mathcal{D}(\rho),\\ \mathcal{D}(\rho) &= 2a_y\rho a_y^\dagger - \{a_y^\dagger a_y,\rho\} + 2a_z\rho a_z^\dagger - \{a_z^\dagger a_z,\rho\}\end{aligned} \tag{9}$$

where we have also included a finite lifetime $\propto 1/\kappa$ for the cavity photons.

The key feature determining dynamics in this model is that the pseudospins J and S are built as bilinears of bosonic operators of the same Hilbert space and, therefore, in general, do not commute with each other. One can define the matrix

$$\Sigma_{ij} = c_i^+ c_j = \begin{pmatrix} \Sigma_{00} & J^-_{01} & \mathcal{T}^-_{02} & S^-_{03}\\ J^+_{01} & \Sigma_{11} & S^-_{12} & \mathcal{T}^-_{13}\\ \mathcal{T}^+_{02} & S^+_{12} & \Sigma_{22} & J^-_{23}\\ S^+_{03} & \mathcal{T}^+_{13} & J^+_{23} & \Sigma_{33}\end{pmatrix} \tag{10}$$

which contains all the possible spin raising and lowering operators coupling the four levels of our scheme. In Σ_{ij} the diagonal elements account for the occupation of the different atomic levels; the pseudospins J describe transitions between different momentum states within the same spin state; the pseudospins S describe transitions between different momentum states within neighboring spin levels, and finally, the pseudospins $\mathcal{T}$ describe transition between different spin levels but with same momentum quantum number. These operators obey a SU(4) algebra with the commutation relations

$$[\Sigma_{nm},\Sigma_{kl}] = \Sigma_{nl}\delta_{m,k} - \Sigma_{km}\delta_{n,l}. \tag{11}$$

The noncommutativity of different pseudospin species (and thus also $[H_s, H] \neq 0$) leads to rich dynamics [60,61]. In particular, symmetry breaking in the subsystem governed by H can induce explicit symmetry breaking in the Hamiltonian H_s, and vice versa, see Appendix F. For instance, the superradiant phase of Hamiltonian H [Eq. (2)] corresponds to the spontaneous breaking of the $\mathbb{Z}_2$ symmetry of the system, such that two alternating nonzero solutions appear with $(a_z, S^x) \leftrightarrow (-a_z, -S^x)$. In terms of the underlying bosonic operators, the symmetry implies

$$c_n \to c_n e^{-i\phi_n}, \quad a_z \to a_z e^{i\pi}. \tag{12}$$

The requirement $S^x \to -S^x$ sets two constraints for four phases of the atomic fields, namely (cf. also Appendix F)

$$\phi_0 - \phi_3 = \pi \pm 2\pi n, \quad \phi_2 - \phi_1 = \pi \pm 2\pi m. \tag{13}$$

As a result, if the coupling η_s is nonvanishing, the symmetry of the interacting term in the Hamiltonian H_s will be explicitly broken by the emergent phase $\pm(\phi_1 - \phi_3)$, $2J^x \to -(J^-_{01}e^{i(\phi_3-\phi_1)} + J^-_{23}e^{-i(\phi_3-\phi_1)} + \text{H.c.})$, which can not be compensated by the phase of a_y. This explicit symmetry breaking manifests in the onset of long-lived nonstationary dynamical responses, even though the Hamiltonian possesses a $\mathbb{Z}_2$ symmetry, and thus, it would be in general expected to relax into a time-independent steady state [68]. On the contrary, in the normal state, the emergent phase $\phi_1 - \phi_3$ can be immediately set to $2\pi n$ (both excited momentum states are unpopulated and $\langle c_1\rangle = \langle c_3\rangle = 0$) and the spontaneous symmetry breaking does not bring any observable effect to the dynamics. Finally, spontaneous symmetry breaking in H_s induces explicit symmetry breaking in H. For a detailed discussion, refer to Appendix F.

We want to emphasize that considering a four-level model is essential for obtaining the above-mentioned nonstationary phases. For instance, omitting the atomic level $|0\rangle$ in $H_{\rm tot}$ to get an effective three-level description relaxes the constraints of Eq. (13) and prevents dynamics arising from explicit symmetry breaking (see Appendix H for a comprehensive discussion).

V. PROBING DYNAMICS WITH THE TWO CAVITY FIELDS

We now discuss the different dynamical regimes arising from the interplay of H_s and H. We show how the auxiliary cavity field dynamics are directly linked with spin precession

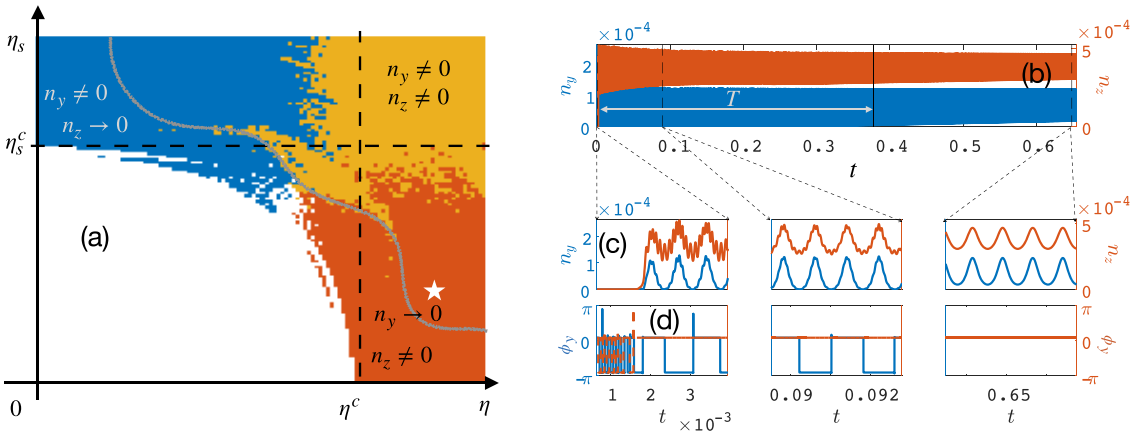

FIG. 6. (a) Dynamical phase diagram with three possible self-organized phases in blue, yellow, and orange. Different phases are distinguished from the dynamics of the two cavity fields $\langle a_y \rangle$ and $\langle a_z \rangle$. Gray line separates parameters for which the explicitly broken symmetry restores during finite (above the line) or infinite (below the line) time. (b) Time evolution of the occupation number for the two cavity modes, for parameters marked with a star in (a). (c) Zoom on the dynamics of the photon number and (d) phase at the beginning, middle, and end of time evolution in panel (b). Time is given in seconds, see main text. Here we fix $\omega_y = \omega_z = 5\kappa$, $\omega_s = \omega_0/4$, $\mu = 0.75$.

and entanglement entropy oscillations, facilitating continuous monitoring of the system's dynamics.

A. Dynamical phase diagram

By tuning the two couplings, η (spin-momentum) and η_s (momentum) below and above criticality, we generate the complete diagram of dynamical responses, reported in Fig. 6(a). We initialize the system in the normal state [69] and then fast ramp it at certain values of the couplings (cf. Appendix C).

As order parameters, we consider the mean field expectation values of two cavity fields, $\langle a_y \rangle$ and $\langle a_z \rangle$. The choice is convenient for two reasons. Firstly, typical experiments operate in a regime where cavity detunings, $\omega_{y,z}$, and decay rates, κ, are a few orders of magnitude larger than atomic energy scales [10–12,36]. Consequently, one can adiabatically eliminate the cavity modes since on timescales $\propto 1/\kappa$ they approach the steady state values $\langle a_y \rangle \approx -2\eta_s(\langle J^x_{01} \rangle + \langle J^x_{23} \rangle)/(\omega_y - i\kappa)$, $\langle a_z \rangle \approx -2\eta(\langle S^x_{03} \rangle + \langle S^x_{12} \rangle)/(\omega_z - i\kappa)$ [70]. Thus the cavity fields $\langle a_y \rangle$ and $\langle a_z \rangle$ offer direct information about momentum $\langle J^x \rangle$ and spin-momentum $\langle S^x \rangle$ coherences in the system. Notice that the naïve elimination of the cavity field at the level of the generator of dynamics would result in a lack of relaxation, which is an artifact (in the Dicke model, the decay appears at the higher order of perturbation theory; see Refs. [36,71,72] for a comprehensive discussion). Indeed, in order to extract the dynamical responses in Fig. 6, we adopt a Redfield master equation approach [70,71]; the corresponding equations of motion are reported in Appendices B and C.

The second reason to use cavity fields as order parameters is their experimental accessibility. Using heterodyne detection [67], which gives access to the magnitude and phase of the cavity fields, it is possible to conduct continuous nondestructive measurements of the system. In contrast, imaging the condensate's spin and density distribution constitutes a destructive measurement, requiring numerous experiment repetitions to reconstruct dynamics.

The system exhibits a variety of self-organization transitions, distinguishable by the dynamics of the cavity fields $\langle a_y \rangle$ and $\langle a_z \rangle$. Firstly, when both couplings are smaller than the critical ones [white region in Fig. 6(a)], the system remains in the normal state with zero occupation of the cavity fields. In terms of atomic degrees of freedom, the internal atomic pseudospin precesses with the frequency $2\omega_s$ and amplitude given by $\sqrt{1/4 - \langle \mathcal{T}^z \rangle^2} = \sqrt{\mu(1-\mu)}$.

By increasing η above the critical value and keeping $\eta_s < \eta_s^c$, the system undergoes a phase transition to the SR phase, associated with breaking of the $\mathbb{Z}_2$ symmetry of H [cf. Eq. (2)]. The occupation of the cavity mode $\langle a_z \rangle$, together with the pseudospin $\langle S^x \rangle$ become nonzero [see red region in Fig. 6(a)]. On the other hand, according to the transformation (12), this spontaneous symmetry breaking also induces explicit symmetry breaking in H_s [Eq. (7)], namely, the interaction term gains a phase $\pm(\phi_1 - \phi_3)$. As a consequence, the pseudospin $\langle J^x \rangle$ starts precessing with a zero time average, resulting in periodic development of $\langle a_y \rangle \propto \langle J^x \rangle$. In this way, subsystem (7) experiences superradiance from the interaction with the subsystem (2); otherwise, since $\eta_s < \eta_s^c$, the pseudospin $\langle J^x \rangle$ together with the cavity field $\langle a_y \rangle$ remain in the normal state.

In the experiment, this dynamical phase can be discerned by measuring both the photon number and phase of the two cavity fields, as illustrated in Figs. 6(b)–6(d). Following the fast ramp at $t = 0$, the observable $n_z = \langle a_z^\dagger a_z \rangle$ approaches a nonzero value. Simultaneously, the photon number of the second mode, denoted as $n_y = \langle a_y^\dagger a_y \rangle$, undergoes oscillations, transitioning from zero to a finite value. At each instance when n_y returns to zero, the phase $\phi_y = \arg(\langle a_y \rangle)$ experiences a discrete shift of π, signifying that $\langle a_y \rangle$ undergoes a sign reversal, as shown in Figs. 6(c) and 6(d). Note that depending on parameters, such a regime with the zero-averaged $\langle a_y \rangle$ and periodic jumps of ϕ_y can take finite time, which we denote T in Fig. 6(b). This time is linked to the propensity of the system to restore explicitly broken symmetry and, as we show in the following section, the finiteness of T can be related to

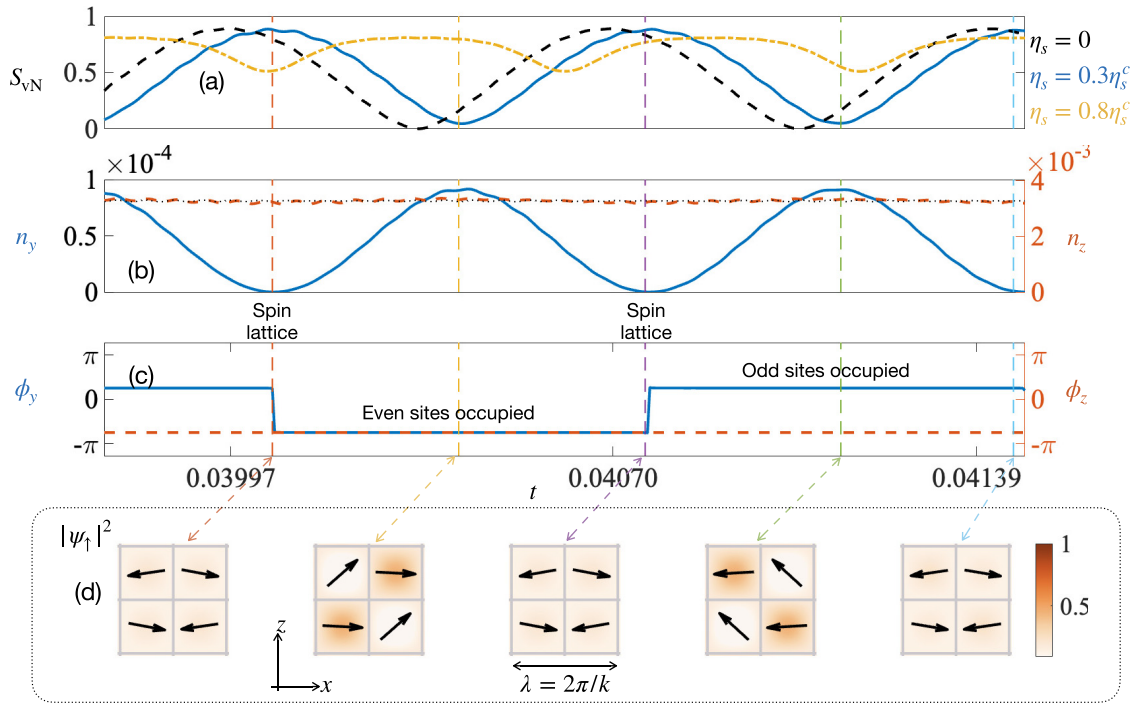

FIG. 7. (a) Dynamics of the entanglement entropy, (b) occupation of the cavity modes, (c) phases of the cavity modes, and (d) real space density in the red region in the phase diagram. The black line in panel (a) corresponds to the $\eta_s = 0$ case, while red and blue lines correspond to the dynamics with nonzero $\eta_s \ll \eta_s^c$. From oscillations of the cavity field phase ϕ_y, one can recover the structure of the real-space checkerboard lattice: when $\phi_y > 0$ odd sites are occupied, and when $\phi_y < 0$ even sited are more occupied. The $n_y = 0$ case corresponds to the maximally entangled state in which the checkerboard is formed by the projection of the spin on the x axis rather than the density lattice.

the possibility of noninvasive continuous monitoring of the entanglement dynamics. In Fig. 6(a) for parameters below, the gray line in panel (a) $T \to \infty$, while for parameters above the line, it takes a finite value.

In the regime where the field $\langle a_y \rangle$ oscillates with zero average, the precession frequency of the pseudospin $\langle J^x \rangle$ can be calculated as the inverse of the time interval over which the phase of $\langle a_y \rangle$ changes by 2π. Simultaneously, the amplitude of $\langle J^x \rangle$ oscillations can be deduced from the maximum value of n_y during one period, $\mathrm{ampl}(\langle J^x \rangle) = [\max(n_y)(\omega_y^2 + \kappa^2)]^{1/2}/(2\eta_s)$.

The time evolution shown in Figs. 6(b)–6(d) is not unique but depends on the phase that is initially imprinted in the boson c_i (pseudospins Σ_{ij}) operators. Different initial conditions can lead to dephasing and variations in the amplitudes and frequencies for different observables due to the nonlinear nature of the problem. However, as we have checked numerically, the oscillatory behavior in Figs. 6(c) and 6(d) is generic for different realizations of the initial conditions, meaning one can observe oscillations of the magnitude of the cavity fields and also periodic jumps of the phase of the auxiliary cavity field.

In the opposite limit, when $\eta_s > \eta_s^c$ and η is below its critical value [blue region in Fig. 6(a)], the transition to the SR phase takes place in cavity field $\langle a_y \rangle$ and pseudospin $\langle J^x \rangle$, while cavity mode $\langle a_z \rangle$ experiences oscillations with zero time-average. These oscillations appear due to the explicit symmetry breaking in Hamiltonian H in Eq. (2) and subsequent precession of the pseudospin $\langle S^x \rangle$. Similarly to the previous case, the precession period is equal to the time interval during which $\phi_z = \arg(\langle a_z \rangle)$ changes by 2π, and the amplitude of $\langle S^x \rangle$ oscillations is $\mathrm{ampl}(\langle S^x \rangle) = [\max(n_z)(\omega_z^2 + \kappa^2)]^{1/2}/(2\eta)$.

Finally, when both couplings are above the critical ones [see the yellow region in Fig. 6(a)], both cavity modes, $\langle a_y \rangle$ and $\langle a_z \rangle$, become nonzero, and the symmetry of both H_s in Eq. (7) and H in Eq. (2) are spontaneously broken in a self-consistent way. Here, both cavity fields have fixed phases, while their magnitudes can oscillate while the system approaches a (stationary) steady state.

B. Slow relaxation in multilevel Dicke model

The oscillations shown in Fig. 6(b) persist far longer than the operational timescales of the experiment. Below, we discuss the mechanism that induces such prolonged relaxation in the dissipative model (8).

The evolution of energy in the two-level Dicke model during relaxation is given by $d\langle E \rangle/dt = \kappa \mathcal{D}(\omega_c a^\dagger a + 2\eta(a + a^\dagger)J^x)$, which in terms of spin degrees of freedom is proportional to $d\langle E \rangle/dt \propto \langle J^x \rangle \langle J^y \rangle$. In the steady state $\langle J^y \rangle = 0$ and the system's energy is constant, indicating that all energy pumped from the external driving fields is completely lost through the dissipation of the cavity mode. However, on its way to stationarity, the spin component $\langle J^y \rangle$ oscillates around zero value, which means that with period $2\omega_0$ energy

is pumped in (negative $\langle J^y \rangle$) and out (positive $\langle J^y \rangle$) of the system, leading to the relaxation time $\tau = (\omega_y^2 + \kappa^2)/(\omega_0^2 \kappa) \gg 1/\kappa$ [68,72].

In contrast, in the four-level model (8), the superradiance in one spin species acts as an "effective drive" for the other, inducing an additional factor that slows down the relaxation. Here, the explicit breaking of the Hamiltonian symmetry results in the generation of nonstationary phases. It happens due to the competing conditions on the phases of the boson fields, $\phi_0, \ldots, \phi_3$, set by H [Eq. (2)] and H_s [Eq. (7)]. Relaxation in the four-level model (8) is conditioned from the temporal evolution of phases of the boson operators $\phi_{0,\ldots,3}$, whose interdependence slows down reaching a steady state, as it happens in constrained models [73,74]. Such slow relaxation is crucial for the continuous read-out of the system's dynamics since spin precession can be easily captured at extensive timescales.

C. Read-out

We now relate the dynamics of the auxiliary cavity field $\langle a_y \rangle$ to the evolution of both the entanglement entropy S_{vN} and the condensate's microscopic degrees of freedom. An instance of such dynamics for parameters as in the red region in Fig. 6 ($\eta_s = 0.3\eta_s^c$, $\eta = 1.6\eta^c$) is shown in Fig. 7. Here, the blue line in panel (a) shows the dynamics of the entanglement entropy, panel (b) the dynamics of the populations of the two cavity modes, panel (c) the dynamics of the phase of two cavity fields, and finally panel (d) shows snapshots of the condensate density at different times. Arrows in panel (d) indicate spin magnetization in the centers of the checkerboard lattice sites.

The oscillations of the photon number $n_y = \langle a_y^\dagger a_y \rangle$ [panel(b)] and the phase $\phi_y = \arg(\langle a_y \rangle)$ [panel (c)] capture precession of the external pseudospin $\langle J^x \rangle$, as $\langle a_y \rangle \approx -2\eta_s(\langle J_{01}^x \rangle + \langle J_{23}^x \rangle)/(\omega_y - i\kappa)$. When the phase of the cavity field changes by $\pm\pi$, the real space density checkerboard lattice changes its parity [odd or even lattice sites are more occupied, see panel (d)]. Concomitantly, the system reaches the maximum value of the entanglement entropy [panel (a)]. At the same time, the checkerboard lattice with period $\lambda = 2\pi/k$ is formed not by modulation of the density but rather by the different orientations of the spin in the centers of even and odd sites.

When the phase of the field $\langle a_y \rangle$ gains $\pm\pi$ jump, the spatial density profile changes parity. At the same time, the increase of the photon number n_y indicates a decrease of entanglement since the coupling η_s tends to disentangle spin and momentum, while a decrease of n_y, on the other hand, indicates the developing of the spin-momentum correlations in the system. In this way, one can capture real-time oscillations of the entanglement entropy from the oscillations of the cavity field $\langle a_y \rangle$.

Finally, the fixed phase of the cavity field a_z, $\phi_z = \arg(\langle a_z \rangle)$, indicates the spontaneous symmetry breaking in H [cf. Eq. (2)]. In terms of the atomic degrees of freedom, the fixed phase ϕ_z in panel (c) captures the absence of the mirror symmetry between maximally entangled states, namely, for two consecutive maximally entangled states, the spin lattices are exactly the same, without the symmetry under swapping even and odd sites, cf. even panels in Fig. 7(d).

The heterodyne detection of two cavity modes a_y and a_z enables distinguishing different dynamical phases in the system in a nondestructive way. However, by itself, the coupling to the auxiliary cavity mode can change the steady state properties and, more importantly in the context of this paper, change the entanglement of the system compared to the single-mode model. In this regard, it is important to separate a range of couplings for which utilizing additional polarization preserves most of the entanglement and, at the same time, is sufficient to perform measurements. We dedicate the next section to this aim.

VI. ENTANGLEMENT IN THE TWO PHOTON FIELDS MODEL

In this section, we revisit the system's various dynamical responses in terms of spin-momentum entanglement generation when both cavity modes contribute to the dynamics and identify parameter ranges suitable for noninvasive monitoring of the dynamics of collective observables. We show criteria to determine the range of parameters for which the auxiliary cavity mode creates a minimal backaction on the system's dynamics. For all extra details, we refer the reader to Appendix G.

The entanglement properties of the system are conditioned from the competition between η (which couples spin-momentum pseudospins with cavity mode a_z and tries to entangle spin and momentum) and η_s (which couples momentum pseudospins J with the cavity field a_y and tends to maintain spin and momentum separable). Figure 8 shows numerical data on the maximal entanglement $\max(S_{\mathrm{vN}})$ as a function of these "spin-momentum" η and "momentum" η_s couplings. Here, we maintain the same parameters as those in the phase diagram of Fig. 6(a). The plot shows that increasing η induces stronger correlations between spin and momentum, while η_s acts as a disentangling agent.

The interplay between η and η_s can significantly alter not only the $\max(S_{\mathrm{vN}})$ but also the steady-state properties of the system along with the evolution of the S_{vN} compared to the $\eta_s = 0$ case. Figure 7(a) shows the evolution of the S_{vN} for weak, strong, and zero coupling η_s to the auxiliary mode a_y. Compared to the unprobed model ($\eta_s = 0$, black line), for weak values the photon-matter coupling slightly modifies the steady state and entanglement dynamics ($\eta_s = 0.3\eta_s^c \ll \eta_s^c$, blue line), while for strong values, it can alter dynamics of the S_{vN} significantly ($\eta_s = 0.8\eta_s^c$, yellow line). These regimes can be distinguished from the dynamics of the auxiliary field. For weak couplings, the read-out is noninvasive, and the auxiliary field oscillates with the zero time average for timescales that significantly exceed the operational timescale of the experiment ($t_{\mathrm{op}} \propto 0.01$ s). In the experiment, these oscillations correspond to periodic changes in the phase of the auxiliary field. In the strong coupling regime, the read-out procedure is invasive, and the phase of the auxiliary field becomes fixed after some time, T, which is comparable with the operational timescale of the experiment. At this time, the explicitly broken symmetry of the Hamiltonian is restored, and the system starts evolving toward the SR state for both cavity fields.

The restoration of the symmetry indicates the change in the steady state and, thus also entanglement properties of the system. Because of this, for nondestructive probing

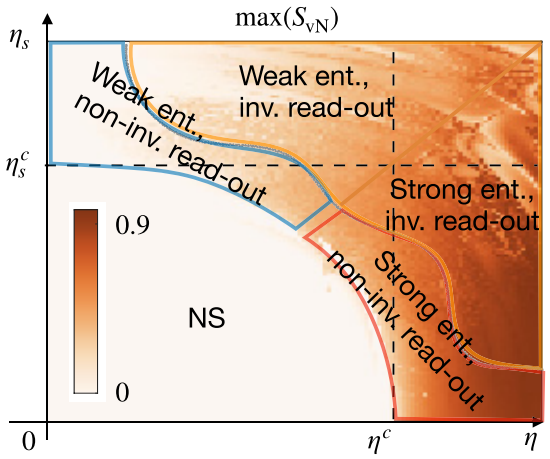

FIG. 8. Maximum value of the entanglement entropy at late times as a function of the couplings η and η_s. Parameters are the same as in Fig. 6. The cartoon in Fig. 1(c) is sketched from the data of this figure. Blue, yellow, and orange lines are added to distinguish different regimes in terms of the amount of spin-momentum entanglement and the invasiveness of the read-out procedure.

of the dynamics, it would be convenient to work in a parameter regime where $T/t_{\rm op} \to \infty$. Our numerics suggests that $T \propto \exp(\eta_s - \eta_s^c)$, revealing that symmetry restoration occurs more rapidly as the coupling to the auxiliary mode approaches the critical threshold, cf. Appendix G. As such, for nondestructive monitoring dynamics, it is essential to maintain the coupling to the auxiliary field significantly below the critical value.

Combining the information on relaxation timescales with the amount of entanglement generated in Fig. 8 (see Appendix C for more details), it appears that in the limit of $\eta \gg \eta^c$ and $\eta_s \ll \eta_s^c$ (parameters region, separated by the red lines in Fig. 8) highly entangled states are prepared, while the system keeps oscillating for long times, facilitating the reconstruction of oscillations of the entanglement entropy by measuring the auxiliary cavity field $\langle a_y \rangle$ (cf. Fig. 7). On the other hand, in the part of the phase diagram dominated by the coupling η_s, there is no strong entanglement, albeit η can still induce short-lived spin-momentum correlations (see parameters region, separated by the blue line in Fig. 8). Finally, when both couplings are high enough (see parameters region separated by yellow lines), probing the system's dynamics with the auxiliary cavity field alters dynamics significantly, and T is finite.

By adjusting experimentally accessible parameters, such as couplings η, η_s and detuning ω_s, one can tune the amplitude, time-average, and oscillation frequency of the entanglement entropy, thereby dynamically controlling the correlation between spin and momentum. In principle, the simplest approach is to set $\omega_y/\kappa \to 0$, which ensures that pseudospins do not receive any feedback from a_y, and thus, all entanglement properties are solely determined by light-matter interactions contained in H. In this case, the dissipation induces a phase shift of the auxiliary cavity field, $\phi_\kappa^y = \tan^{-1}(-\kappa/\omega_y) = \pi/2$ [11], making it imaginary, $\langle a_y \rangle + \langle a_y^\dagger \rangle = 0$, and reducing backaction of the field a_y on the H, see Appendix G. However, the effective model with $H_{\rm tot}$ [Eq. (8)] breaks down for these extreme conditions because the many-body description of the model, in this case, requires taking into account higher momentum modes.

A more practical scenario is when the frequency of the auxiliary cavity photon ω_y is much higher than κ. In this case, it is easier to maintain $\eta_s/\eta_s^c \ll 1$, but have cavity occupations n_y large enough to continuously measure the collective momentum.

Furthermore, sizable stationary entanglement can be preserved when $\omega_s = 0$. Here, the Hamiltonian gains additional symmetry under the exchange of ground and excited momentum levels of two spin sublevels, $(|0\rangle, |1\rangle) \leftrightarrow (|2\rangle, |3\rangle)$. In this case, the induced as a result of the explicit symmetry breaking phase $\pm(\phi_1 - \phi_3)$ does not evolve in time, and the explicitly broken symmetry can not be restored, see Appendix G for comprehensive discussion. For $\omega_s = 0$, the maximal and time-averaged amount of entanglement remains similar to the one generated with one main cavity mode [see Fig. 3(a)], besides a small dressing induced by η_s.

VII. CONCLUSIONS AND OUTLOOK

In this work, we have presented an experimentally feasible cavity QED platform featuring an effective four-level atomic description and shown that it manifests two intertwined self-organization transitions. This system serves as a minimal model wherein spontaneous symmetry breaking occurs in an all-to-all interacting spin model, concomitant with the formation of tunable spin-momentum entanglement. The controlled leakage of intracavity photons plays an important stabilization role, as the resulting dissipative dynamics facilitate convergence towards the target entangled state in a manner resilient to imperfections in the system's couplings or initial state preparation. Extending the coupling scheme with an auxiliary cavity mode gives rise to persistent oscillations (due to explicit symmetry breaking) and facilitates real-time monitoring of the system dynamics, in particular, as a proxy for entanglement.

The tunable parameters of our model facilitate a straightforward extension to spin-exchange interactions, akin to the Tavis-Cummings model [30,36,50]. An interesting avenue for exploration lies in understanding how quantum correlations between spin and momentum can be continuously tuned as one transitions between the Tavis-Cummings and Dicke limits considered here.

We should note that a relation between multilevel atoms and entanglement has been previously reported both in cavity QED systems [29,75–77] and photonic waveguides [9,78–81]. In these cases, entangled states can be hosted within the subradiant subspaces of the multilevel atoms, with level degeneracies being crucial for the build-up of quantum correlations. The mechanism is markedly different from ours, although considering a combination of the two setups could naturally lead to further interesting developments.

Taking a broader perspective, one could investigate how different dynamical phases of matter routinely engineered in cavity QED would morph, when both spin and momentum degrees of freedom are optically addressed. Our analysis has focused on the superradiant phase transition as a paradigmatic

case, but it would be intriguing to see whether entanglement properties of spin-momentum hybridized states can be manipulated as a response to periodic drives [16,17,82] or in the context of dissipative-induced phase transitions [11,15,18,30,83].

ACKNOWLEDGMENTS

The authors thank Tilman Esslinger for fruitful discussions. O.C. is grateful to M. Stefanini and R. J. Valencia-Tortora for many useful discussions. This project has been supported by the Deutsche Forschungsgemeinschaft (DFG, German Research Foundation) Project-ID 429529648 TRR 306 QuCoLiMa "Quantum Cooperativity of Light and Matter") and by the QuantERA II Programme that has received funding from the European Union's Horizon 2020 Research and Innovation Programme under Grant Agreement No. 101017733 (QuSiED) and by the DFG (Project No. 499037529). We acknowledge funding from the Swiss National Science Foundation (Project No. 212168 and IZBRZ2_-186312), from EU Horizon 2020 (European Research Council advanced grant TransQ, Project No. 742579) and from the Swiss Secretariat for Education, Research and Innovation (SERI). J.M. and O.C. acknowledge support from the Dynamics and Topology Centre funded by the State of Rhineland Palatinate. K.S. acknowledges funding from NSF EAGER-QAC-QCH Award No. 2037687. The authors gratefully acknowledge the computing time granted on the supercomputer MOGON 2 at Johannes Gutenberg-University Mainz [84].

APPENDIX A: DERIVATION OF THE HAMILTONIAN

In this Appendix, we present a derivation of Hamiltonian $H_{\rm tot}$ for a setup depicted in Figs. 2 and 5. The derivation of the Hamiltonian H or H_s can be obtained by setting $E_s = 0$ or $E_b = E_r = 0$ below respectively.

We start with the general Hamiltonian for the light-matter interaction problems, which reads

$$H_{\rm tot} = H_c + H_a + H_{\rm int}, \tag{A1}$$

where H_c governs dynamics of the cavity mode, H_a is a single-atom Hamiltonian, and $H_{\rm int}$ describes interaction between atom and the cavity. We specify the explicit form of H_c, H_a, and $H_{\rm int}$ in the considered setup and show under which assumptions the low-energy physics of the model can be simulated by Eq. (8).

We immerse ^{87}Rb atoms inside an optical cavity oriented along the $\mathbf{e}_x$ axis. The cavity has a single relevant frequency $\omega_c = 2\pi \times 382.04685$ THz with a decay rate of $\kappa \sim 2\pi \times 1.25$ MHz, and two polarizations $\mathbf{e}_y$ and $\mathbf{e}_z$ in the transverse plane. We represent two corresponding cavity polarization modes by operators a_y and a_z, respectively. The cavity Hamiltonian reads

$$H_c = \hbar\omega_y a_y^\dagger a_y + \hbar\omega_z a_z^\dagger a_z. \tag{A2}$$

We apply a classical pump field with the standing-wave profile along $\mathbf{e}_z$ (perpendicular to the cavity axis) and a Gaussian profile in the transverse directions, along $\mathbf{e}_x$ and $\mathbf{e}_y$. We consider a dispersive regime, in which pumping frequency is chosen out-of-resonance with the electron transition $5^2S_{1/2} \to 5^2P_{1/2}$, $5^2P_{3/2}$. In this case, excited atomic states can be eliminated, and the resulting atomic Hamiltonian within the $F = 1$ hyperfine manifold of the $5^2S_{1/2}$ level reads

$$H_a = \frac{\mathbf{p}^2}{2M} + V_{\rm ext} + \sum_{F,m_F} \hbar\omega_{F,m_F} |F, m_F\rangle\langle F, m_F|, \tag{A3}$$

where $\mathbf{p}$ is the momentum of the atom, M is the atomic mass, $V_{\rm ext}$ describes an external trapping potential, and the energy of atomic level $|F, m_F\rangle$ is $\hbar\omega_{F,m_F}$. The sum in the last terms runs over all atomic levels in $F = 1$ manifold. We apply a strong magnetic field $\mathbf{B} = -B\mathbf{e}_z$ along z direction, which induces first- and second-order Zeeman splitting between levels with different magnetic numbers m_F. Introducing internal spin operator $\mathbf{F} = (F^x, F^y, F^z)$, the atomic part of the Hamiltonian can be rewritten

$$H_a = \frac{\mathbf{p}^2}{2M} + V_{\rm ext} + \hbar\omega_z^{(1)} F^z + \hbar\omega_z^{(2)} (F^z)^2, \tag{A4}$$

where $\omega_z^{(1)} < 0$ and $\omega_z^{(2)} > 0$ are the first and the second-order Zeeman splittings.

The atoms are neutral and are much smaller than the wavelength of the optical light fields so that the light-matter interaction can be described in the dipole approximation

$$H_{\rm int} = -\mathbf{d}_{\rm lab}\mathbf{E}_{\rm lab}, \tag{A5}$$

where the atomic dipole operator can be expanded in terms of the atom's internal states

$$\mathbf{d}_{\rm lab} = \sum_{e,g} \mathbf{d}_{eg} |e\rangle\langle g| + \text{H.c.}, \quad \mathbf{d}_{eg} = \langle e|\mathbf{d}|g\rangle. \tag{A6}$$

The total optical field $\mathbf{E}_{\rm lab}$ is the sum of the classical pump field, $\mathbf{E}_p(\mathbf{r})$, and the cavity field, $\mathbf{E}_c(\mathbf{r})$. The classical pump field with the polarization along $\mathbf{e}_y$, has a standing-wave profile in the longitudinal direction ($\mathbf{e}_z$) and a Gaussian profile in the transverse direction (along $\mathbf{e}_x$, $\mathbf{e}_y$):

$$\mathbf{E}_p(\mathbf{r}) = \mathbf{e}_y \sum_{\beta=b,r,s} \frac{E_\beta}{2} f_\beta(\mathbf{r}) e^{-i\omega_\beta t} + \text{H.c.}, \tag{A7}$$

with the mode function for each sideband is $f_\beta(\mathbf{r}) \equiv f(\mathbf{r}) = \exp(-2x^2/w_x^2 - 2y^2/w_y^2)\cos(k_\beta z)$. The widths of the transverse Gaussian profile are approximately $\omega_x, \omega_y \approx 25$ μm. The wave-vectors are $k_\beta = \omega_\beta/c \approx \omega_p/c$ with c denoting speed of light. To induce the atomic transitions, discussed in Secs. II and IV, we consider three laser drivers $\beta = b, r, s$, with the sideband frequencies $\omega_{b(r)}$ such that detunings $\delta\omega_\beta = \omega_\beta - \omega_p$ are chosen to correspond to the differences in first-order Zeeman shifts (in the $F = 1$ ground state manifold). In contrast, the third detuning is set to be zero, $\omega_s = (\omega_b + \omega_r)/2 = \bar{\omega}$. In this case, different driving schemes operate with the same momentum states. We limit our consideration to the case when $E_b = E_r \neq E_s$.

The cavity field TEM00 mode of a Fabry-Perot cavity has a standing-wave profile in the transverse direction ($\mathbf{e}_x$) and a Gaussian profile in the other two directions along $\mathbf{e}_y$ and $\mathbf{e}_z$:

$$\mathbf{E}_c(\mathbf{r}) = \mathbf{e}_y E_c g_y(\mathbf{r}) a_y + \mathbf{e}_z E_c g_z(\mathbf{r}) a_z + \text{H.c.}, \tag{A8}$$

where the mode functions are $g_{y,z}(\mathbf{r}) \equiv g(\mathbf{r}) = \exp(-2(y^2 + z^2)/w_c^2)\cos(k_c x)$ with the Gaussian profile having a width of approximately $w_c \approx 25$ μm. The wave-vectors are $k_{y,z} \approx k_c = \omega_c/c$.

As we are working in the dispersive regime, the excited atomic states can be eliminated using the Schrieffer-Wolff [85] transformation $H \to e^{S} H e^{-S}$, $[S, H_0] = -H_{\rm int}$, which results in the low-energy Hamiltonian

$$
\begin{aligned}
H_0 &= \frac{\mathbf{p}^2}{2M} + V_{\rm ext} + \hbar\omega^{(1)}F^z + \hbar\omega^{(2)}(F^z)^2 + \hbar\omega_c^y a_y^\dagger a_y + \hbar\omega_c^z a_z^\dagger a_z \\
H_{\rm int}^s &= \alpha_s f^2(\mathbf{r}) \left| \sum_\beta \frac{E_\beta}{2} e^{i\delta\omega_\beta t} \right|^2 + \alpha_s |E_c|^2 g^2(\mathbf{r}) \left(a_y^\dagger a_y + a_z^\dagger a_z\right) \\
&\quad + \alpha_s \overbrace{\left(\mathbf{e}_y \cdot \mathbf{e}_y\right)}^{=1} f(\mathbf{r}) g(\mathbf{r}) \sum_\beta \frac{E_\beta}{2} \left(e^{i\omega_\beta t} a_y + e^{-i\omega_\beta t} a_y^\dagger\right) + \alpha_s \overbrace{\left(\mathbf{e}_y \cdot \mathbf{e}_z\right)}^{=0} f(\mathbf{r}) g(\mathbf{r}) \sum_\beta \frac{E_\beta}{2} \left(e^{i\omega_\beta t} a_z + e^{-i\omega_\beta t} a_z^\dagger\right) \\
H_{\rm int}^v &= -i\frac{\alpha_v}{2F} g(\mathbf{r}) f(\mathbf{r}) \sum_\beta \frac{E_c E_\beta}{2} \left[\left(a_y e^{i\omega_\beta t} - a_y^\dagger e^{-i\omega_\beta t}\right) \overbrace{\left(\mathbf{e}_y \times \mathbf{e}_y\right)}^{=0} \cdot \mathbf{F} + \left(a_z e^{i\omega_\beta t} - a_z^\dagger e^{-i\omega_\beta t}\right) \overbrace{\left(\mathbf{e}_y \times \mathbf{e}_z\right)}^{=\mathbf{e}_x} \cdot \mathbf{F} \right] \\
&\quad \underbrace{-i\frac{\alpha_v}{2F} E_c^2 g^2(\mathbf{r}) \left(a_y^\dagger a_z - a_z^\dagger a_y\right) \left(\mathbf{e}_y \times \mathbf{e}_z\right) \cdot \overbrace{\mathbf{F}}^{\propto e^{\pm i\omega t}}}_{=0, \text{ because of resonance conditions}}
\end{aligned}
\tag{A9}
$$

For the transitions in multilevel atoms, it is convenient to account for selection rules using polarizabilities. In the above equation, $\alpha_{s,v}$ are scalar and vector polarizabilities of the atoms, which are components of the rank-2 tensor $\alpha_{i,j} = \sum_{g,g'} \sum_e \langle g|d_i|e\rangle\langle e|d_j^\dagger|g'\rangle|g\rangle\langle g'|/(\hbar\Delta_e) = \alpha_{\rm s} {\rm I}\delta_{ij} - i\alpha_{\rm v}/(2\,{\rm F})\epsilon_{ijk} + \ldots$ Here, diagonal components, proportional to α_s, describe the process when the spin of the atom remains unchanged, while vectorial nondiagonal components, proportional to α_v, describe the transition of the spin state of the atom after the two-photon process. The sum runs over all allowed transitions (see Ref. [86]), $d_i = (\mathbf{d}\mathbf{e}_i)$ is the ith component of the atomic dipole moment, $i = \{x, y, z\}$, and the detuning of the driving field from the resonance frequency is $\Delta_e \approx \omega_p - \omega_e$.

Finally, we move to a frame rotating with the classical pump frequency: $H_{\rm lab} \to H = U_p^\dagger H_{\rm lab} U_p - H_p$, where $U_p = \exp(-iH_p t/\hbar)$ and $H_p = \sum_e \hbar\omega_p |e\rangle\langle e| + \hbar\omega_p (a_y^\dagger a_y + a_z^\dagger a_z)$. The rotating-wave approximation brings us to the time-independent single-body Hamiltonian

$$
H_{\rm tot} = H_a + H_c + H_s + H_v, \tag{A10}
$$

$$
H_a = \frac{\mathbf{p}^2}{2M} + V_{\rm ext} + \hbar\delta^{(1)}F^z + \hbar\omega^{(2)}(F^z)^2, \tag{A11}
$$

$$
H_c = -\Delta_y a_y^\dagger a_y - \Delta_z a_z^\dagger a_z, \tag{A12}
$$

$$
\begin{aligned}
H_s &= \frac{\alpha_s}{4} f^2(\mathbf{r}) \left(E_s^2 + E_b^2 + E_r^2\right) + \alpha_s E_0^2 g^2(\mathbf{r}) \left(a_y^\dagger a_y + a_z^\dagger a_z\right) \\
&\quad + \frac{\alpha_s}{2} f(\mathbf{r}) g(\mathbf{r}) E_0 E_s \left(a_y + a_y^\dagger\right),
\end{aligned}
\tag{A13}
$$

$$
H_v = \frac{\alpha_v}{4} E_0 E_b f(\mathbf{r}) g(\mathbf{r}) \left(a_z + a_z^\dagger\right) F^x, \tag{A14}
$$

where $\delta^{(1)} = \omega_z^{(1)} + (\omega_b - \omega_r)/2$, $\Delta_{y,z} = \bar{\omega} - \omega_{y,z} < 0$. We have also applied a transformation $a_z \to i a_z$ to get rid of the minus sign in H_v. The first term in H_s describes the attractive potential created by the transverse driving fields, the second term describes the dispersive shift to the cavity detuning, and the last term produces the Bragg transition within the same atomic level. The vectorial interaction describes the Raman process when the transition happens between nearing sublevels of the ground-state manifold.

Let us consider a case when the magnetic field is strong. Specifically, let the second order Zeeman shift $\omega^{(2)} \propto 1$ MHz, and thus the resonant conditions for transition $m_F = 1 \leftrightarrow m_F = 0$ are out-of-resonance for transition $m_F = 0 \leftrightarrow m_F = -1$. In this case, if we prepare the initial state as a mixture of particles at levels with $m_F = 1, 0$, the dynamics will be restricted to these two atomic levels for the typical operational times of the experiment. Thus we can limit our consideration to the dynamics between two neighboring spin levels, defining the many-body spinor field operator

$$
\Psi(\mathbf{r}) = (0, \psi_\uparrow, \psi_\downarrow)^T, \tag{A15}
$$

which satisfies standard bosonic commutation relations $[\psi_\sigma(\mathbf{r}), \psi_{\sigma'}^\dagger(\mathbf{r}')] = \delta_{\sigma,\sigma'}\delta(\mathbf{r} - \mathbf{r}')$, $[\psi_\sigma(\mathbf{r}), \psi_{\sigma'}(\mathbf{r}')] = 0$, where $\sigma, \sigma' = \{\uparrow, \downarrow\}$. The $N-$body Hamiltonian reads

$$
\begin{aligned}
H_{\rm tot} &= H_c + \int d\mathbf{r} \Psi^\dagger(\mathbf{r}) (H_a + H_s + H_v) \Psi(\mathbf{r}) \\
&= H_c + \int d\mathbf{r} \left[\frac{\alpha_s}{4} \left(E_s^2 + E_b^2 + E_r^2\right) f^2(\mathbf{r}) + \alpha_s E_0^2 \left(a_y^\dagger a_y + a_z^\dagger a_z\right) g^2(\mathbf{r}) \right] \left(\psi_\uparrow^\dagger(\mathbf{r})\psi_\uparrow(\mathbf{r}) + \psi_\downarrow^\dagger(\mathbf{r})\psi_\downarrow(\mathbf{r})\right)
\end{aligned}
$$

$$+\int d\mathbf{r}\psi_\uparrow^\dagger(\mathbf{r})\left(-\frac{\hbar^2\nabla^2}{2M}+V_{\text{ext}}\right)\psi_\uparrow(\mathbf{r})+\int d\mathbf{r}\psi_\downarrow^\dagger(\mathbf{r})\left(-\frac{\hbar^2\nabla^2}{2M}+V_{\text{ext}}\right)\psi_\downarrow(\mathbf{r})$$
$$+\frac{\hbar\delta^{(1)}}{2}\int d\mathbf{r}\big(\psi_\uparrow^\dagger(\mathbf{r})\psi_\uparrow(\mathbf{r})-\psi_\downarrow^\dagger(\mathbf{r})\psi_\downarrow(\mathbf{r})\big)+\frac{\hbar\omega^{(2)}}{4}\int d\mathbf{r}\big(\psi_\uparrow^\dagger(\mathbf{r})\psi_\uparrow(\mathbf{r})+\psi_\downarrow^\dagger(\mathbf{r})\psi_\downarrow(\mathbf{r})\big)$$
$$+\frac{\alpha_s}{2}E_0E_s\big(a_y+a_y^\dagger\big)\int d\mathbf{r}f(\mathbf{r})g(\mathbf{r})\big(\psi_\uparrow^\dagger(\mathbf{r})\psi_\uparrow(\mathbf{r})+\psi_\downarrow^\dagger(\mathbf{r})\psi_\downarrow(\mathbf{r})\big)$$
$$+\frac{\alpha_v}{8}E_0E_b\big(a_z+a_z^\dagger\big)\int d\mathbf{r}f(\mathbf{r})g(\mathbf{r})\big(\psi_\uparrow^\dagger(\mathbf{r})\psi_\downarrow(\mathbf{r})+\psi_\downarrow^\dagger(\mathbf{r})\psi_\uparrow(\mathbf{r})\big). \tag{A16}$$

To derive an extended Dicke Hamiltonian, we should further restrict the Hilbert space of the model by considering only the two lowest momentum states of the model for both spinor components. In this approximation, the many-body wave function reads $\Psi(\mathbf{r})=(0,\phi_0(\mathbf{r})c_0+\phi_1(\mathbf{r})c_1,\phi_0c_2(\mathbf{r})+\phi_1(\mathbf{r})c_3)^T$. Here, c_i are the annihilation operators of the corresponding atomic modes, $[c_i,c_j^\dagger]=\delta_{i,j}$, $[c_i,c_j]=0$, and $\phi_1(\mathbf{r})=\mathcal{N}\cos kx\cos kz\phi_0(\mathbf{r})$, where $\mathcal{N}$ accounts for the correct normalization. In this notation, operators c_0 and c_2 correspond to the ground momentum states, while operators c_1 and c_2 correspond to the excited momentum states. After integrating over all space, the many-body Hamiltonian reads

$$\begin{aligned}H_{\text{tot}}=&-\hbar\tilde{\Delta}_ya_y^\dagger a_y+\hbar\omega_0(c_1^\dagger c_1+c_3^\dagger c_3)+\hbar\eta_s(a_y+a_y^\dagger)(c_0^\dagger c_1+c_1^\dagger c_0+c_2^\dagger c_3+c_3^\dagger c_2)\\&-\hbar\tilde{\Delta}_za_z^\dagger a_z+\hbar\omega_s(c_2^\dagger c_2+c_3^\dagger c_3)+\hbar\eta(a_z+a_z^\dagger)(c_1^\dagger c_2+c_0^\dagger c_3+c_2^\dagger c_1+c_3^\dagger c_0),\end{aligned} \tag{A17}$$

where the cavity detuning is dressed via the dynamic (dispersive) shift $\tilde{\Delta}_{y,z}=\Delta_{y,z}-\alpha_sE_0^2N\mathcal{I}/\hbar$, the level splitting between ground and excited momentum states is equal $\omega_0=2\omega_{\text{rec}}$, $\omega_s=\delta^{(1)}$, and coupling constants read as follows: $\hbar\eta_s=\alpha_sE_0E_s\mathcal{M}/2$, $\hbar\eta=-\alpha_vE_0E_b\mathcal{M}/4\sqrt{2}$, where $\mathcal{I}=\int d\mathbf{r}g^2(\mathbf{r})\phi_0^2(\mathbf{r})$, $\mathcal{M}=\int d\mathbf{r}f(\mathbf{r})f(\mathbf{r})\phi_1(\mathbf{r})\phi_0(\mathbf{r})$. We have omitted standing-wave potential $\alpha_s(E_s^2+E_b^2+E_r^2)\int d\mathbf{r}f^2(\mathbf{r})\phi_0^2(\mathbf{r})/4$ above as it only contributes to the higher momentum state and does not qualitatively modify the appearance of the phase transition discussed in the main text in Fig. 6.

Finally, one can introduce pseudospin operators according to Eq. (10), which brings the Hamiltonian to the following form:

$$\begin{aligned}H_{\text{tot}}=&\omega_ya_y^\dagger a_y+\omega_0\big(J_{01}^z+J_{23}^z\big)+\eta_s(a_y+a_y^\dagger)(J_{01}^++J_{23}^++J_{01}^-+J_{23}^-)\\&+\omega_za_z^\dagger a_z+\omega_s\big(S_{12}^z+S_{03}^z\big)+\eta(a_z+a_z^\dagger)(S_{12}^++S_{03}^++S_{12}^-+S_{03}^-),\end{aligned} \tag{A18}$$

where we set $\omega_{y,z}=-\tilde{\Delta}_{y,z}>0$ and have normalized the Hamiltonian by $\hbar\omega_{\text{rec}}$ so that $\omega_0=2$ above. One should take into account that due to the particle conservation, one has $J_{01}^z+J_{23}^z=S_{03}^z-S_{12}^z$. Additionally, when $\eta=0$, the term $\omega_s(S_{12}^z+S_{03}^z)$ can be omitted because the process $\eta_s(a_y+a_y^\dagger)(J_{01}^++J_{23}^++J_{01}^-+J_{23}^-)$ preserves the number of particles in the upper and lower spinor components, and thus the contribution to the energy of the system from the $\omega_s(S_{12}^z+S_{03}^z)$ remains constant during the whole course of the dynamics.

APPENDIX B: EQUATIONS OF MOTION

In this Appendix, we derive mean-field equations of motion from the Hamiltonian in (A18). Note that for the remainder of the Appendices, we omit $\langle\cdot\rangle$ for expectation values of observables for simplicity.

The mean-field equations of motion can be easily derived from the Lindblad master equation (9) and read

$$\begin{aligned}\dot{a}_y&=-i(\omega_y-i\kappa)a_y-i\eta_s(c_0^\dagger c_1+c_1^\dagger c_0+c_2^\dagger c_3+c_3^\dagger c_2),\\\dot{a}_z&=-i(\omega_z-i\kappa)a_z-i\eta(c_1^\dagger c_2+c_0^\dagger c_3+c_2^\dagger c_1+c_3^\dagger c_0),\\\dot{c}_0&=-i\eta(a_z+a_z^\dagger)c_3-i\eta_s(a_y+a_y^\dagger)c_1,\\\dot{c}_1&=-i\omega_0c_1-i\eta(a_z+a_z^\dagger)c_2-i\eta_s(a_y+a_y^\dagger)c_0,\\\dot{c}_2&=-i\omega_sc_2-i\eta(a_z+a_z^\dagger)c_1-i\eta_s(a_y+a_y^\dagger)c_3,\\\dot{c}_3&=-i(\omega_s+\omega_0)c_3-i\eta(a_z+a_z^\dagger)c_0-i\eta_s(a_y+a_y^\dagger)c_2.\end{aligned} \tag{B1}$$

In terms of pseudospin degrees of freedom (10), the equations of motion take the following form:

$$\begin{aligned}\frac{dJ_{01}^-}{dt}&=-2i\omega_0J_{01}^-+2i\eta_s(a_y+a_y^\dagger)J_{01}^z+i\eta(a_z+a_z^\dagger)(\mathcal{T}_{13}^+-\mathcal{T}_{02}^-),\\\frac{dJ_{23}^-}{dt}&=-2i\omega_0J_{23}^-+2i\eta_s(a_y+a_y^\dagger)J_{23}^z+i\eta(a_z+a_z^\dagger)(\mathcal{T}_{13}^--\mathcal{T}_{02}^+),\\\frac{dJ_{01}^z}{dt}&=i\eta_s(a_y+a_y^\dagger)(J_{01}^--J_{01}^+)+i\eta/2(a_z+a_z^\dagger)(S_{12}^+-S_{12}^-+S_{03}^--S_{03}^+),\end{aligned}$$

$$
\begin{aligned}
\frac{dJ^z_{23}}{dt} &= i\eta_s(a_y + a_y^\dagger)(J^-_{23} - J^+_{23}) + i\eta/2(a_z + a_z^\dagger)(S^+_{12} - S^-_{12} + S^-_{03} - S^+_{03}),\\
\frac{dS^-_{12}}{dt} &= 2i(\omega_0 - \omega_s)S^-_{12} + 2i\eta(a_z + a_z^\dagger)S^z_{12} + i\eta_s(a_y + a_y^\dagger)(\mathcal{T}^-_{02} - \mathcal{T}^-_{13}),\\
\frac{dS^-_{03}}{dt} &= -2i(\omega_0 + \omega_s)S^-_{03} + 2i\eta(a_z + a_z^\dagger)S^z_{03} + i\eta_s(a_y + a_y^\dagger)\big(\mathcal{T}^-_{13} - \mathcal{T}^-_{02}\big),\\
\frac{dS^z_{12}}{dt} &= i\eta(a_z + a_z^\dagger)(S^-_{12} - S^+_{12}) + i\eta_s/2(a_y + a_y^\dagger)(-J^-_{01} + J^+_{01} - J^-_{23} + J^+_{23}),\\
\frac{dS^z_{03}}{dt} &= i\eta(a_z + a_z^\dagger)(S^-_{03} - S^+_{03}) + i\eta_s/2(a_y + a_y^\dagger)(J^-_{01} - J^+_{01} + J^-_{23} - J^+_{23}),\\
\frac{d\mathcal{T}^-_{13}}{dt} &= -2i\omega_s\mathcal{T}^-_{13} + i\eta(a_z + a_z^\dagger)(J^-_{23} - J^+_{01}) + i\eta_s(a_y + a_y^\dagger)(S^-_{03} - S^-_{12}),\\
\frac{d\mathcal{T}^-_{02}}{dt} &= -2i\omega_s\mathcal{T}^-_{02} + i\eta(a_z + a_z^\dagger)(J^+_{23} - J^-_{01}) + i\eta_s(a_y + a_y^\dagger)(S^-_{12} - S^-_{03})\\
\frac{d\mathcal{T}^z_{13}}{dt} &= i\eta/2(a_z + a_z^\dagger)(S^-_{03} - S^+_{03} + S^-_{12} - S^+_{12}) + i\eta_s/2(a_y + a_y^\dagger)(J^-_{23} - J^+_{23} - J^-_{01} + J^+_{01}),\\
\frac{d\mathcal{T}^z_{02}}{dt} &= i\eta/2(a_z + a_z^\dagger)(S^-_{03} - S^+_{03} + S^-_{12} - S^+_{12}) + i\eta_s/2(a_y + a_y^\dagger)(J^+_{23} - J^-_{23} + J^-_{01} - J^+_{01}).
\end{aligned}
\tag{B2}
$$

Note that on the mean-field level, both (B1) and (B2) govern identical dynamics when the system is initially prepared in the coherent state. However, if the initial state contains higher-order correlations, one needs to consider higher-order corrections (i.e., cumulants expansion or similar methods) to capture dynamics accurately [61].

Finally, the equations of motion on the mean-field level can be derived without truncation over momentum states, starting from Hamiltonian (A16), $i\hbar\partial_t\Psi(\mathbf{r},t) = H_{\rm tot}(\mathbf{r})\Psi(\mathbf{r},t)$, which results into the following equations of motion:

$$
\begin{aligned}
i\hbar\frac{d\psi_\uparrow(\mathbf{r})}{dt} &\approx \frac{\hbar\delta^{(1)}}{2}\psi_\uparrow(\mathbf{r}) - \frac{\hbar^2\nabla^2}{2M}\psi_\uparrow(\mathbf{r}) + \overbrace{\frac{\alpha_s}{2}E_0E_s}^{\tilde\eta_s}\big(a_y + a_y^\dagger\big)f(\mathbf{r})g(\mathbf{r})\psi_\uparrow(\mathbf{r}) + \overbrace{\frac{\alpha_v}{8}E_0E_b}^{\tilde\eta}\big(a_z + a_z^\dagger\big)f(\mathbf{r})g(\mathbf{r})\psi_\downarrow(\mathbf{r})\\
i\hbar\frac{d\psi_\downarrow(\mathbf{r})}{dt} &\approx -\frac{\hbar\delta^{(1)}}{2}\psi_\downarrow(\mathbf{r}) - \frac{\hbar^2\nabla^2}{2M}\psi_\downarrow(\mathbf{r}) + \frac{\alpha_s}{2}E_0E_s\big(a_y + a_y^\dagger\big)f(\mathbf{r})g(\mathbf{r})\psi_\downarrow(\mathbf{r}) + \frac{\alpha_v}{8}E_0E_b\big(a_z + a_z^\dagger\big)f(\mathbf{r})g(\mathbf{r})\psi_\uparrow(\mathbf{r})\\
i\hbar\frac{da_y}{dt} &\approx \hbar(\omega_y - i\kappa)a_y + \frac{\alpha_s}{2}E_0E_s\int d\mathbf{r}f(\mathbf{r})g(\mathbf{r})\big(\psi^\dagger_\uparrow(\mathbf{r})\psi_\uparrow(\mathbf{r}) + \psi^\dagger_\downarrow(\mathbf{r})\psi_\downarrow(\mathbf{r})\big)\\
i\hbar\frac{da_z}{dt} &\approx \hbar(\omega_z - i\kappa)a_z + \frac{\alpha_v}{8}E_0E_b\int d\mathbf{r}f(\mathbf{r})g(\mathbf{r})\big(\psi^\dagger_\uparrow(\mathbf{r})\psi_\downarrow(\mathbf{r}) + \psi^\dagger_\downarrow(\mathbf{r})\psi_\uparrow(\mathbf{r})\big).
\end{aligned}
\tag{B3}
$$

To retrieve dynamics at short times one can sufficiently simplify equations by eliminating cavity fields, substituting $a_y \approx -\alpha_sE_0E_s\int d\mathbf{r}f(\mathbf{r})g(\mathbf{r})(\psi^\dagger_\uparrow(\mathbf{r})\psi_\uparrow(\mathbf{r}) + \psi^\dagger_\downarrow(\mathbf{r})\psi_\downarrow(\mathbf{r}))/(2\hbar(\omega_y - i\kappa))$ and $a_z \approx -\alpha_vE_0E_b\int d\mathbf{r}f(\mathbf{r})g(\mathbf{r})(\psi^\dagger_\uparrow(\mathbf{r})\psi_\downarrow(\mathbf{r}) + \psi^\dagger_\downarrow(\mathbf{r})\psi_\uparrow(\mathbf{r}))/(8\hbar(\omega_z - i\kappa))$. Choosing periodic boundary conditions for field $\Psi(\mathbf{r})$, the resultant equations of motion can be further efficiently evaluated with the split-step Fourier transform method [87].

Both equations (B1) and (B3) describe the similar dynamical behavior of the system and transition from the normal to superradiant phase with the subsequent population of the momentum states $|1\rangle_m$ [note that Eq. (B3) also captures population of the momentum states $|\pm 2k, 0, 0\rangle$ and $|0, 0, \pm 2k\rangle$, however for the most of the parameters the fraction of atoms there can be neglected]. However, to study long-time dynamics, evaluation of (B1) can be done much more efficiently, with much less computational cost. The further simplification via proper elimination of the cavity fields is described in the following Appendix.

APPENDIX C: REDFIELD EQUATIONS

To evaluate dynamics at late times, we also adiabatically eliminate dissipative cavity modes a_y and a_z and study the atom-only model. This procedure is justified by the separation of scales between cavity detunings/decay rates and atomic frequencies, which differ by two to three orders of magnitude. By applying the Schrieffer-Wolff transformation, the atom and photon modes can be decoupled, resulting in the effective atom-only description of the model. Following calculations in Refs. [70,71], we derive the following expressions for the

effective fields α_y and α_z:

$$\alpha_y = \frac{\eta_s(c_1^\dagger c_0 + c_3^\dagger c_2)}{-\omega_y - \omega_0 + i\kappa} + \frac{\eta_s(c_0^\dagger c_1 + c_2^\dagger c_3)}{-\omega_y + \omega_0 + i\kappa},$$
$$\alpha_z = \frac{\eta c_3^\dagger c_0}{-\omega_z - (\omega_s + \omega_0) + i\kappa} + \frac{\eta c_0^\dagger c_3}{-\omega_z + (\omega_s + \omega_0) + i\kappa} + \frac{\eta c_2^\dagger c_1}{-\omega_z + (\omega_0 - \omega_s) + i\kappa} + \frac{\eta c_1^\dagger c_2}{-\omega_z - (\omega_0 - \omega_s) + i\kappa}. \tag{C1}$$

On the mean-field level, the effective equations of motion can be derived by substituting into Eqs. (B1) (α_y, α_z) instead of boson fields (a_y, a_z). The atom-only model allows us to investigate long-time dynamics and numerically explore relaxation processes. However, it is important to note that this model operates correctly when both couplings are ramped up gradually. Abrupt changes in coupling can excite high-energy excitations in the model, which are not accounted for by the Redfield equation.

To evaluate the long-time dynamical response in Fig. 6(a) (and also in Fig. 8), we initialize the system in the normal state and then ramp up both coupling during ≈0.002 s, which is slow enough to make Redfield description of the dynamics valid and, at the same time, fast enough to excite nonstationary phases. We then compare dynamical properties of the system $(\langle a_y\rangle, \langle a_z\rangle)$ after the ramp at $t \approx 0.01$ s and at late times $t \approx 0.4$ s to distinguish between phases with the explicitly broken symmetry (which suit for noninvasive dynamics monitoring) and phases with explicitly broken symmetry, which identify strong coupling regime and invasive probing of the dynamics.

APPENDIX D: ANALYTICAL CALCULATION OF THE STEADY STATE

Both models (7) and (2) take the form of the Dicke model and thus undergo a phase transition associated with the spontaneous breaking of $\mathbb{Z}_2$ symmetry. The phases associated with this symmetry breaking are the normal phase, in which all spins are polarized long z direction and occupation of the cavity photon is zero, and the superradiant phase, in which spins develop a nonzero x component, with the cavity occupation taking a nonzero value. The solution for each case can be derived as a stable stationary state of Eqs. (B2). As an illustration, let us examine the case when one of the couplings is equal to zero.

1. $\eta = 0$ case

In this case, the critical coupling is equal to $\eta_s^c = \sqrt{\omega_0(\omega_y^2 + \kappa^2)/(4\omega_y)}$ and the solution in the SR phase read $J_{01}^z = -\mu\eta_s^{c2}/(2\eta_s^2)$, $J_{23}^z = -(1-\mu)\eta_s^{c2}/(2\eta_s^2)$, $J^x = \pm\sqrt{1/4 - J^{z2}}$, $a_y = -\eta_s/(\omega_y - i\kappa)\sqrt{1 - \eta_s^{c4}/\eta_s^4}$. Interestingly, in this case, the spins $\mathcal{T}$, S are not stationary but instead can precess according to the equations of motion

$$\frac{dS_{12}^-}{dt} = 2i(\omega_0 - \omega_s)S_{12}^- + i\eta_5\left(a_y + a_y^\dagger\right)\left(\mathcal{T}_{02}^- - \mathcal{T}_{13}^-\right)$$
$$\frac{dS_{03}^-}{dt} = -2i(\omega_0 + \omega_s)S_{03}^- + i\eta_5\left(a_y + a_y^\dagger\right)\left(\mathcal{T}_{13}^- - \mathcal{T}_{02}^-\right)$$
$$\frac{d\mathcal{T}_{13}^-}{dt} = -2i\omega_s\mathcal{T}_{13}^- + i\eta_5\left(a_y + a_y^\dagger\right)\left(S_{03}^- - S_{12}^-\right)$$
$$\frac{d\mathcal{T}_{02}^-}{dt} = -2i\omega_s\mathcal{T}_{02}^- + i\eta_5\left(a_y + a_y^\dagger\right)\left(S_{12}^- - S_{03}^-\right). \tag{D1}$$

In the normal phase, the frequency of the precession is equal to $\pm 2\omega_s$, while in the SR phase, additional dressing from the interaction with the cavity mode a_y takes place

$$\Omega = -2\omega_s \pm \frac{4\sqrt{\omega_0^2\left(\omega_y^2 + \kappa^2\right)^2/4 - \omega_y^2\left(\eta_s^{c4} - \eta_s^4\right)}}{\left(\omega_y^2 + \kappa^2\right)}. \tag{D2}$$

These dynamics stem from the fact that three species of the pseudospins in the model governed by $H_{\rm tot}$ in Eq. (8) are built from the same boson operators, and thus, they do not commute. Consequently, spontaneous symmetry breaking in one species of the pseudospins can induce explicit symmetry breaking for the rest of the spin species, which results in the oscillatory behavior unless the explicitly broken symmetry is restored, see Appendix F for more details.

One can also restore the occupation of the four levels in the steady-state superradiant phase

$$c_0^\dagger c_0 = \frac{\mu(1 - 2J^z)}{2},$$
$$c_1^\dagger c_1 = \frac{\mu(1 + 2J^z)}{2},$$
$$c_2^\dagger c_2 = \frac{(1-\mu)(1 - 2J^z)}{2},$$
$$c_3^\dagger c_3 = \frac{(1-\mu)(1 + 2J_z)}{2}, \tag{D3}$$

where μ is the fraction of atoms, initialized in state $|0\rangle$, $N_0 = Nc_0^\dagger c_0 = \mu N$.

It is worth mapping the solution in terms of spins (or bosons) back to the microscopic observables in the model (A16). In this way, one can unravel phase transition in the model (8) in the form of the self-organization transition(s) in terms of atomic degrees of freedom, such as condensate density and magnetization.

The density of the upper spinor component is $\rho_\uparrow = |\psi_\uparrow|^2 = |\langle c_0\rangle\phi_0 + \langle c_1\rangle\phi_1|^2 = |\langle c_0\rangle|^2\phi_0^2 + (\langle c_0^\dagger\rangle\langle c_1\rangle + \langle c_1^\dagger\rangle\langle c_0\rangle)\phi_0\phi_1 + |\langle c_1\rangle|^2\phi_1^2$. The first term here is constant, while the second one takes the form $\cos kx \cos kz \propto \phi_1$ and describes the creation of the checkerboard lattice with the periodicity $2\pi/k$ when the system is in the SR phase, cf. Figs. 5(d) and 5(e). Similarly, the density of the lower spinor component reads $\rho_\downarrow = |\psi_\downarrow|^2 = |\langle c_2\rangle\phi_0 + \langle c_3\rangle\phi_1|^2$. At the same time, one can calculate the spatial distribution of the spin through the lattice. The three components of this spin are given by $\sigma^z = (|\psi_\uparrow|^2 - |\psi_\downarrow|^2)/2$, $\sigma^x = \Re(\psi_\uparrow^*\psi_\downarrow)$, $\sigma^y = \Im(\psi_\uparrow^*\psi_\downarrow)$. Here, we denote spin-1/2 operators with σ^i to highlight the effective two internal spin levels nature of the effective model (operator F above is defined on the spin-1 manifold). In the main text, we have plotted the values of these spins, calculated at the center of lattice cells using arrows on top of the distribution of the condensate density.

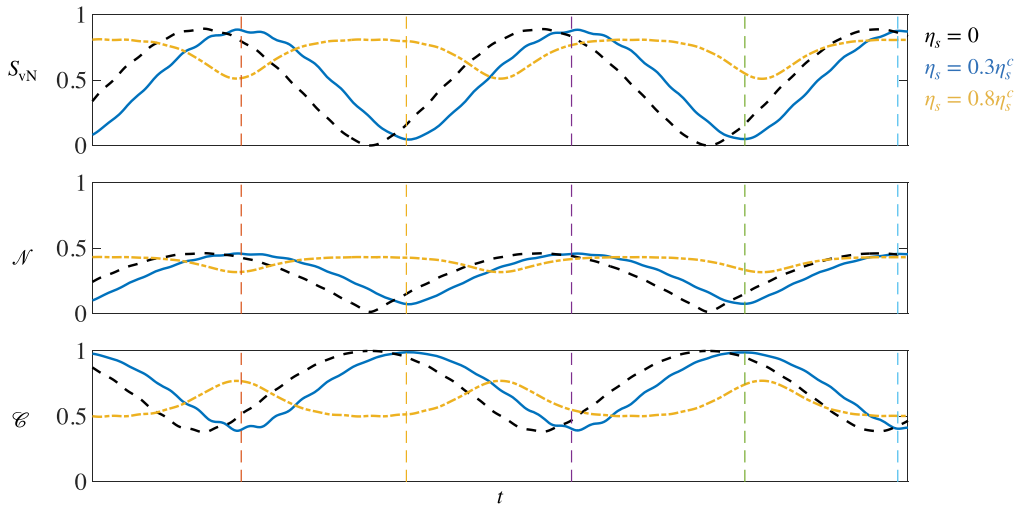

FIG. 9. Dynamics of (a) entanglement entropy S_{vN}, (b) negativity $\mathcal{N}$, and (c) concurrence $\mathscr{C}$ for parameters as in Fig. 7 in the main text. Different lines correspond to different values of coupling η_s. The vertical dashed lines added to guide the eye and show the time moments when the entropy measures for $\eta_s = 0.3\eta_s^c$ case take extremal values during dynamics.

2. $\eta_s = 0$ case

The model (2) is a two-spin Dicke model with disorder in the level splittings. By deriving stationary solutions for this model, one can recover that the critical coupling, at which transition to the SR phase occurs, depends on the initial state. The resulting expression is given by Eq. (4). The S^z spin components can be further found from $[(\omega_s+\omega_0)+2\omega_z\eta^2/(\omega_z^2+\kappa^2)S_z^{03}]S_x^{03}=0$ and $[(\omega_s-\omega_0)+2\omega_z\eta^2/(\omega_z^2+\kappa^2)S_z^{12}]S_x^{12}=0$. Also, note that when one or both of the level splittings $\omega_0 \pm \omega_s$ become negative, the initial state with particles prepared in the ground momentum state $\psi=\sqrt{\mu}|0\rangle+\sqrt{1-\mu}|2\rangle$ is effectively a population inverted state. Thus the transition to the SR phase appears on longer timescales after the system relaxes to the ground state (corresponding to an excited momentum state). In this case, one can first observe decay with a "burst" of atoms to the excited momentum states $|1\rangle$ and $|3\rangle$, and then approach the correct SR state with a finite population of ground and excited momentum states.

As it is illustrated in the main text, the SR transition in the spin S, which is built simultaneously from different momentum and spin atomic states [cf. Eq. (1)], can act as driving for both spin and density (momentum) of the BEC. Examples of such nonstationary behavior of internal/external degrees of freedom are shown in Figs. 2(d), 2(e) and 4(b), 4(c). This nonstationary behavior also can be seen by analyzing equations of motion for pseudospins $\mathcal{T}$ and J :

$$\begin{aligned}
\frac{dJ_{01}^-}{dt} &= -2i\omega_0 J_{01}^- + 2i\eta\Re(a_z)(\mathcal{T}_{13}^+ - \mathcal{T}_{02}^-),\\
\frac{dJ_{23}^-}{dt} &= -2i\omega_0 J_{23}^- + 2i\eta\Re(a_z)(\mathcal{T}_{13}^- - \mathcal{T}_{02}^+),\\
\frac{d\mathcal{T}_{13}^-}{dt} &= -2i\omega_s \mathcal{T}_{13}^- + 2i\eta\Re(a_z)(J_{23}^- - J_{01}^+),\\
\frac{d\mathcal{T}_{02}^-}{dt} &= -2i\omega_s \mathcal{T}_{02}^- + 2i\eta\Re(a_z)(J_{23}^+ - J_{01}^-).
\end{aligned} \tag{D4}$$

These equations result in the following precession frequencies

$$\begin{aligned}
\Omega &\to -\sqrt{2}\sqrt{-\frac{1}{4}\sqrt{\left(16\eta^2\Re(a_z)^2+4\omega_0^2+4\omega_s^2\right)^2-64\omega_0^2\omega_s^2}-4\eta^2\Re(a_z)^2-\omega_0^2-\omega_s^2},\\
\Omega &\to -\sqrt{2}\sqrt{\frac{1}{4}\sqrt{\left(16\eta^2\Re(a_z)^2+4\omega_0^2+4\omega_s^2\right)^2-64\omega_0^2\omega_s^2}-4\eta^2\Re(a_z)^2-\omega_0^2-\omega_s^2}.
\end{aligned} \tag{D5}$$

APPENDIX E: SPIN-MOMENTUM ENTANGLEMENT

In this Appendix, we show how the von Neumann entropy witnesses correlations between spin and momentum. Similar calculations for the negativity [54] and concurrence [55,56] have also been performed. In our simulations, both quantities behaved similarly for all simulations, cf. Fig. 9.

We can write down the atomic state as a superposition

$$|\psi\rangle = \alpha|0\rangle + \beta|1\rangle + \gamma|2\rangle + \delta|3\rangle, \tag{E1}$$

where $\alpha=\langle c_0\rangle$, $\beta=\langle c_1\rangle$, $\gamma=\langle c_2\rangle$, and $\delta=\langle c_3\rangle$, with $|\alpha|^2+|\beta|^2+|\gamma|^2+|\delta|^2=1$ as the total number of atoms is conserved and normalized. Rewriting states $|0\rangle,\ldots,|3\rangle$ in terms of spin and momentum states, see Eq. (1), the state of the system reads

$$\begin{aligned}
|\psi\rangle =& \alpha|0\rangle_m\otimes|\downarrow\rangle_s + \beta|1\rangle_m\otimes|\downarrow\rangle_s\\
&+\gamma|0\rangle_m\otimes|\uparrow\rangle_s + \delta|1\rangle_m\otimes|\uparrow\rangle_s.
\end{aligned} \tag{E2}$$

We now can construct a reduced density matrix by summing over the spin degree of freedom

$$\tilde{\rho} = \langle \text{spin}|\psi\rangle\langle\psi|\text{spin}\rangle \tag{E3}$$

or by summing over the momentum states

$$\tilde{\rho} = \langle \text{momentum}|\psi\rangle\langle\psi|\text{momentum}\rangle. \tag{E4}$$

The reduced density matrix reads

$$\tilde{\rho} = \begin{bmatrix} |\alpha|^2 + |\beta|^2 & \alpha\gamma^* + \beta\delta^* \\ \alpha^*\gamma + \beta^*\delta & |\gamma|^2 + |\delta|^2 \end{bmatrix} \tag{E5}$$

and can be easily diagonalized. The eigenvalues of this reduced density matrix are

$$\lambda = \tfrac{1}{2} \pm \tfrac{1}{2}\sqrt{1 - 4(|\alpha|^2|\delta|^2 + |\beta|^2|\gamma|^2 - \alpha\beta^*\gamma^*\delta - \alpha^*\beta\gamma\delta^*)}$$

or can alternatively be rewritten in terms of spins

$$\lambda = \tfrac{1}{2} \pm \tfrac{1}{2}\sqrt{1 - 4(S^-_{03}S^+_{03} + S^-_{12}S^+_{12} - J^+_{01}J^-_{23} - J^-_{01}J^+_{23})}.$$

When $\eta = 0$, the system always remains in the pure state as the momentum state is separable in this case; in the superradiant phase, the fraction of atoms in the excited momentum state for $m_F = 0$ is the same as the fraction of excited states for $m_F = 1$.

On the other hand, when $\eta_s = 0$, the interaction η induces entanglement between spin and momentum. The easiest way to see this is to consider the two-level case when all atoms are initially prepared in state $|0\rangle$. Then, by increasing the coupling η above its critical value, the wave function of the state becomes $\psi = \alpha|0\rangle + \delta|3\rangle = \alpha|0\rangle_m \otimes |\downarrow\rangle_s + \delta|1\rangle_m \otimes |\uparrow\rangle_s$, which is not separable in spin and momentum and, thus, is entangled. This state is maximally entangled when $\alpha = \delta = 1/\sqrt{2}$, and in terms of spin and momentum degrees of freedom, the state of the system is symmetric spin-momentum configuration.

APPENDIX F: SPONTANEOUS AND EXPLICIT SYMMETRY BREAKING

In this Appendix, we gather arguments to elucidate the source of the nonequilibrium oscillatory phases that arise when one coupling surpasses the critical threshold while the other remains below it [cf. red and blue regions in the phase diagram in Fig. 6(a)].

Let us consider the case when $\eta_s > \eta_s^c$, i.e., the cavity mode a_y is the important mode. The SR transition in H_s appears when the corresponding $\mathbb{Z}_2$ symmetry of the model is broken. For the subsystem built on the momentum states (via photon mode a_y, [12]), which is described by the Hamiltonian

$$\begin{aligned} H_s = {} & \omega_y a_y^\dagger a_y + \omega_0\big(c_1^\dagger c_1 + c_3^\dagger c_3\big) \\ & + \eta_s\big(a_y + a_y^\dagger\big)\big(c_0^\dagger c_1 + c_1^\dagger c_0 + c_2^\dagger c_3 + c_3^\dagger c_2\big), \end{aligned} \tag{F1}$$

we have the condition

$$\begin{aligned} a_y &\to -a_y \\ \big(c_0^\dagger c_1 + c_2^\dagger c_3 + \text{H.c.}\big) &\to -\big(c_0^\dagger c_1 + c_2^\dagger c_3 + \text{H.c.}\big). \end{aligned} \tag{F2}$$

The second line above corresponds to $J^x \to -J^x$ for the Dicke model. Under the corresponding transformation in Eq. (12) the bosonic part of the Hamiltonian transforms as

$$\begin{aligned} c_0^\dagger c_1 + c_2^\dagger c_3 + \text{H.c.} &\to c_0^\dagger c_1 e^{i(\phi_0-\phi_1)} + c_2^\dagger c_3 e^{i(\phi_2-\phi_3)} + \text{H.c.} \\ &= -\big(c_0^\dagger c_1 + c_2^\dagger c_3 + \text{H.c.}\big), \end{aligned} \tag{F3}$$

thus seting the constrains $e^{\pm i(\phi_1-\phi_0)} = -1$ and $e^{\pm i(\phi_2-\phi_3)} = -1$. These constraints bring us to the following condition on the relative phases:

$$\phi_0 - \phi_1 = \pi \pm 2\pi n, \quad \phi_2 - \phi_3 = \pi \pm 2\pi m. \tag{F4}$$

As only the relative phase between two bosonic fields enters the Hamiltonian, we get two conditions for four phases. If we perform the same transformation on the second interacting term in the total Hamiltonian in Eq. (8), which reads

$$\eta\big(a_z + a_z^\dagger\big)\big(c_1^\dagger c_2 + c_0^\dagger c_3 + c_2^\dagger c_1 + c_3^\dagger c_0\big), \tag{F5}$$

we find that it induces an additional phase for photon field a_z, which provokes an explicit symmetry breaking

$$\begin{aligned} & \eta\big(a_z e^{-i\phi_z} + a_z^\dagger e^{i\phi_z}\big)\big(c_1^\dagger c_2 e^{i(\phi_1-\phi_2)} + c_0^\dagger c_3 e^{i(\phi_0-\phi_3)} + c_2^\dagger c_1 e^{-i(\phi_1-\phi_2)} + c_3^\dagger c_0 e^{-i(\phi_0-\phi_3)}\big) \\ & = \eta\big(a_z e^{-i\phi_z} + a_z^\dagger e^{i\phi_z}\big)\big(c_1^\dagger c_2 e^{i(\phi_1-\phi_3-\pi)} + c_0^\dagger c_3 e^{i(\phi_1+\pi-\phi_3)} + c_2^\dagger c_1 e^{-i(\phi_1-\phi_3-\pi)} + c_3^\dagger c_0 e^{-i(\phi_1+\pi-\phi_3)}\big) \\ & = -\eta\big(a_z e^{-i\phi_z} + a_z^\dagger e^{i\phi_z}\big)\big(c_1^\dagger c_2 e^{i(\phi_1-\phi_3)} + c_0^\dagger c_3 e^{i(\phi_1-\phi_3)} + c_2^\dagger c_1 e^{-i(\phi_1-\phi_3)} + c_3^\dagger c_0 e^{-i(\phi_1-\phi_3)}\big). \end{aligned} \tag{F6}$$

One can recognize that the bosonic part gains a phase $\pm(\phi_1 - \phi_3)$ which, generally, can take an arbitrary value and cannot be immediately compensated by the phase ϕ_z. So, as soon as we turn on coupling η, we break the symmetry of the Hamiltonian. In general, to restore the symmetry at finite time T, the population of the two levels (one excited and another ground momentum states) must reach zero value. In practice, when $\omega_s > 0$, particles from levels $|2\rangle$ and $|3\rangle$ drift to states $|0\rangle$ and $|1\rangle$ (or in the opposite direction when $\omega_s < 0$).

The breaking of the symmetry can be seen also in the following calculation. Given the steady state for $\eta_s > \eta_s^c$ and $\eta = 0$ [cf. Eq. (D3)], after quenching η, the photon mode a_z becomes

$$a_z = -\frac{2\eta}{(\omega_z + i\kappa)}\sqrt{(1-\mu)\mu(1+2J^z)(1-2J^z)}, \tag{F7}$$

which is nonzero for $\mu \neq 0, 1$. Here, the typical time at which the photon approaches the value above is $\approx 1/\kappa$

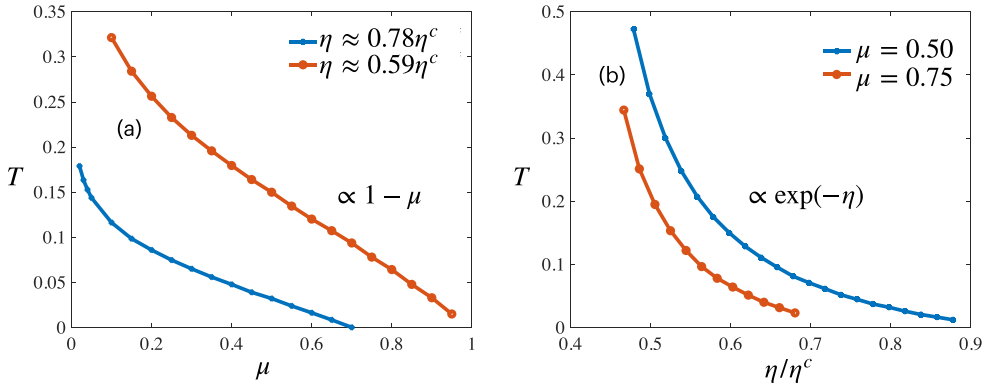

FIG. 10. Symmetry restoration time T (in seconds) as a function of (a) the initial population of the level $|0\rangle$, i.e., $N_0 = \mu N$ and (b) of the photon-matter coupling to the auxiliary cavity field. Here we consider mode a_y as the main and mode a_z as the auxiliary. Here, for simplicity, we set $\omega_y = \omega_z \approx \kappa/3$, $\omega_s = 0.2$. For these two simulations, we prepare the system in the superradiant phase for $\eta_s = 1.2\eta_s^c$, and then perform a fast ramp of $\eta < \eta^c$.

negligibly small. The explicit breaking of the symmetry in the term

$$\eta\left(a_z + a_z^\dagger\right)\left(c_1^\dagger c_2 + c_0^\dagger c_3 + c_2^\dagger c_1 + c_3^\dagger c_0\right) \to - \eta\left(a_z e^{-i\phi_z} + a_z^\dagger e^{i\phi_z}\right)\left(c_1^\dagger c_2 e^{i(\phi_1-\phi_3)} + c_0^\dagger c_3 e^{i(\phi_1-\phi_3)} + c_2^\dagger c_1 e^{-i(\phi_1-\phi_3)} + c_3^\dagger c_0 e^{-i(\phi_1-\phi_3)}\right) \tag{F8}$$

takes the system out of equilibrium. To reach steady state, the Hamiltonian must regain the symmetry via one of two mechanisms.

(1) The decay of the photon number of the auxiliary mode to zero, $n_z = 0$.

(2) The phases of the bosons adjusting to satisfy the condition $\phi_1 - \phi_3 \equiv 0$.

The oscillatory phase accompanies the system's dynamics until one of these two possibilities is realized. Below, we discuss both scenarios in more detail.

APPENDIX G: RELAXATION DYNAMICS AT LATE TIMES

In this Appendix, we study the properties of the system at late times and evaluate the time T at which the system restores its symmetry.

To restore the explicitly broken symmetry, one needs to tune the emergent phases in front of the auxiliary photons, ϕ_c, and pseudospins, $\phi_i - \phi_j$, to zero. This procedure can be trivially done when the corresponding occupation of the photon or atomic levels equals zero due to the ambiguity of the phase of these complex numbers when their magnitude is zero. In the former case, the symmetry restoration occurs asymptotically at time $T \to \infty$ through the slow decay of the cavity photon magnitude induced by the dissipation κ. In line with this scenario, the dynamics, when expressed in terms of the two cavity fields, resemble the behavior depicted in the middle panels of Figs. 6(c) and 6(d) during the course of the experiment.

According to the second mechanism, which takes a finite time T, during dynamics all particles slowly transfer to the lowest energy pair of ground and excited momentum states. For instance, if $\omega_s > 0$, all particles will redistribute to levels $|0\rangle$ and $|1\rangle$ resulting into $\langle c_2(T)\rangle = 0$ and $\langle c_3(T)\rangle = 0$. Then, when states with higher energy become empty, the explicitly broken symmetry of the system can be restored. Eventually, the phases of both cavity fields remain constant, and both fields start approaching true superradiant states with $n_y \neq 0$ and $n_z \neq 0$, cf. the right panels in Figs. 6(c) and 6(d).

Figure 10 shows the scaling of the relaxation time with (a) the fraction of particles at $t = 0$ in state $|0\rangle$, and (b) with the strength of the smaller of the two couplings, i.e., auxiliary one. Here, we prepare the system in the superradiant steady state with $\eta_s > \eta_s^c$, and then rapidly ramp the second coupling η. In these simulations we consider the mode a_z as the auxiliary one for simplicity because its critical coupling depends on μ. The finite time T corresponds to the scenario when symmetry restoration takes place through the transferring of all particles to the lower energy pair of ground and excited momentum states. For instance, for $\omega_s > 0$, the more particles are initially prepared in state $|2\rangle$, the longer is T [cf. Fig. 10(a)]. Assuming that the speed of particles transferring from levels $|2\rangle$ and $|3\rangle$ remains constant and depends solely on the couplings and detunings, the relaxation time will be proportional to the population of the zero momentum state with the higher energy. One would estimate in this case $T \propto (1-\mu)$ as we confirm numerically in panel (a). At the same time, when $\omega_s < 0$, the pair of states that have smaller energy are $|2\rangle$ and $|1\rangle$, and the relaxation time scales like $T \propto \mu$. This can also be seen from the Hamiltonian $H_{\rm tot}$ which in the normal state is invariant under the transformation $\mu \leftrightarrow 1-\mu$ when $\omega_s \to -\omega_s$.

On the other hand, the symmetry restoration time scales with the coupling to the auxiliary mode [η in Fig. 10(b)] like $T \propto \exp(-\eta)$. It means that the closer this auxiliary coupling is to its critical value, the faster the symmetry is restored. Consequently, operating within a parameter regime where the coupling to the auxiliary mode remains significantly below the critical threshold, yet remains finite, gives us the opportunity to probe the atomic dynamics within the system with minimal disruption.

Below we consider a few fine-tuned limits in which a stationary state can not be reached within the operational timescales of the experiment.

1. $\kappa/\omega_c \to \infty$ limit

The relaxation time T depends on the strength of the photon-matter coupling with the auxiliary mode; namely, the stronger the interaction, the faster the relaxation [see Fig. 10(b)]. On the other hand, the strength of this coupling controls the population of the auxiliary cavity mode, $n \propto \eta^2/(\omega_c^2+\kappa^2)$. As such, it is instructive to explore the regime where $\eta/\sqrt{\omega_c^2+\kappa^2}$ is large enough to produce sufficiently large cavity field amplitude to enable detections of oscillations in the auxiliary cavity field. We would also like to simultaneously satisfy the condition $\eta \ll \eta_c$ so that the system's restoration of its symmetry becomes protracted to exponentially late times. These conditions can be satisfied simultaneously when $\omega_c \ll \kappa$, a regime in which the critical coupling diverges like $\sqrt{\omega_0\kappa^2/\omega_c}$. The extreme case of $\omega_c = 0$ corresponds to the critical coupling tending to infinity. Counter-intuitively, in this case, one enters a strong dissipation regime which prevents the relaxation.

The main idea of why the strong dissipation regime prevents relaxation can be explained as follows: according to the Hamiltonian $H_{\rm tot}$ [Eq. (8)], pseudospins are coupled to the real quadrature of the cavity fields, $a + a^\dagger$. If the cavity fields are coupled to the $x-$components of pseudospins, then the cavity field is imaginary, $a_y \propto 2J^x/(-i\kappa)$ (or $a_z \propto 2S^x/(-i\kappa)$). Here the cavity decay rate causes a phase shift $\phi_\kappa^{y,z} = \tan^{-1}(-\kappa/\omega_{y,z})$ of the field scattered into the cavity by the atomic system [11]. Thus, by setting the cavity detuning ω_y or ω_z to be much smaller than κ, one can make the corresponding cavity field imaginary and eliminate its feedback on the spin dynamics. For instance, when $\eta_s > \eta_s^c$, $\eta < \eta^c$ and $\omega_y \neq 0$, $\omega_z \to 0$ [blue region in Fig. 6(a)], a_y approaches its steady state value, while $a_z \approx -2\eta(S^x_{03}+S^x_{12})/(-i\kappa)$ oscillates together with the precession of the pseudospin S^x. However, as $(a_z + a_z^\dagger) \to 0$, the nonstationary behavior of the cavity field does not impact the dynamics of pseudospin S^x. In other words, subsystem H_s constantly induces precession for pseudospin S^x (and thus oscillations to the cavity mode a_z) due to the explicit symmetry breaking; it does not, however, experience feedback from subsystem H. As a result, the lack of reciprocal interaction between the two subsystems prevents the system from reaching a steady state, and oscillations in the auxiliary cavity mode a_z survive for an arbitrarily long time.

When $\eta_s < \eta_s^c$ and $\eta > \eta^c$ [red region in the phase diagram in Fig. 6(a)], one should set $\omega_y \ll \kappa$ to prevent the system from reaching its steady state. In this case, the cavity mode a_y will exhibit oscillations around zero for an arbitrarily long time, reflecting the precession of pseudospin J^x. The cavity mode a_z, in turn, will approach its steady state value, determined solely by the Hamiltonian H [Eq. (2)] and initial conditions.

Interestingly, in the opposite limit where $\omega_c \gg \kappa$, the system can also experience slow relaxation. The critical coupling scales like $\eta_c \propto \sqrt{\omega_0\omega_c} \to \infty$; it is easier to keep the coupling strongly subcritical while still large enough to enable read-out. However, as the cavity occupation scales as $n \propto 1/\omega_c^2$, in order to keep n nonzero, it is essential to keep the cavity detuning finite.

2. $\omega_s \to 0$ limit

One can recognize from the level scheme in Fig. 2(b) that when $\omega_s = 0$, the two ground states in the momentum variables, $|0\rangle$, $|2\rangle$, and the two excited ones $|1\rangle$, $|3\rangle$ are degenerate. In this case, the Hamiltonian acquires an additional symmetry under exchange between ground or excited states, namely $c_1 \leftrightarrow c_3$, $c_0 \leftrightarrow c_2$ (see Hamiltonian in the bosonic representation in Appendix A). As a consequence, the dynamics for the pair of fields c_1, c_3 (and likewise for c_0, c_2) occur at the same frequencies $c_1, c_3 \propto \exp(i\Omega t)$. Accordingly, the phase that explicitly breaks the symmetry of the Hamiltonian, $\pm(\phi_1 - \phi_3)$, remains constant over time, determined solely by the initial conditions (which can be arbitrary and are not restricted in general). Thus, after the quench, both spins J^x and S^x gain fixed time values, and one can observe superradiance in both cavity modes simultaneously. Interestingly, in this case, n_y and n_z do not oscillate over time, and nonstationary behavior can only be observed at the level of the atomic observables. In particular, particles redistribute between different excited or ground momentum states so that the overall number of particles in the upper and lower spinor components oscillates over time around a common time-averaged value.

APPENDIX H: THREE-LEVEL MODEL

We now revisit the possibility of probing the system's dynamics with the auxiliary cavity field in a three-level system. As mentioned in the main text, such a model includes single ground momentum state $|2\rangle$, and two excited momentum states $|1\rangle$, $|3\rangle$, where we keep notation as in the Eq. (1). Such Hamiltonian can be implemented when fixing $\mathbf{e}_p = \mathbf{e}_x$ in Eq. (A7) and considering resonant spin changing and spin-dependent processes, cf. implementations in Refs. [11,36]. Here we omit the implementation of the three-level model, concentrating mostly on the physical phenomena, compared to the four-level model in Eq. (8). To do so, we study the effect of spontaneous symmetry breaking in one sector of the Hamiltonian on the dynamical properties in another sector. As we demonstrate below, explicit symmetry breaking in the self-ordered phase(s) is not pronounced in the three-level case, thereby resulting in trivial system dynamics.

The Hamiltonian of our three-level model reads

$$\begin{aligned} H_3 =& \omega_y a_y^\dagger a_y + \omega_z a_z^\dagger a_z + \omega_0(c_1^\dagger c_1 + c_3^\dagger c_3) + \omega_s(c_2^\dagger c_2 + c_3^\dagger c_3) \\ &+ \eta(a_z + a_z^\dagger)(c_1^\dagger c_2 + c_2^\dagger c_1) + \eta_s(a_y + a_y^\dagger)(c_2^\dagger c_3 + c_3^\dagger c_2). \end{aligned} \tag{H1}$$

Let us consider the effect of the spontaneous symmetry breaking in one subsystem on the dynamics of another, similarly as it is done in Appendix F. Firstly, we consider a steady state when $\eta_s > \eta_s^c$ and $\eta = 0$. In this case, the symmetry of a subsystem involving photon mode a_y is broken, meaning there exist two solutions, satisfying

$$a_y \to -a_y, \quad (c_2^\dagger c_3 + c_3^\dagger c_2) \to -(c_2^\dagger c_3 + c_3^\dagger c_2). \tag{H2}$$

Applying transformation (12), we can see that such transformation

$$c_2^\dagger c_3 + c_3^\dagger c_2 \to c_2^\dagger c_3 e^{i(\phi_2-\phi_3)} + c_3^\dagger c_2 e^{i(\phi_3-\phi_2)} = -\left(c_2^\dagger c_3 + c_3^\dagger c_2\right) \tag{H3}$$

sets the following constraints on relative phases:

$$\phi_2 - \phi_3 = \pi \pm 2\pi m. \tag{H4}$$

Note that there are no restrictions on the phase ϕ_1 because photon mode a_y is not coupled to the level $|1\rangle$. As such, making the second coupling, η, nonzero does not induce explicit symmetry breaking. This fact can be seen by applying the transformation (12) to this term:

$$\left(a_z e^{-i\phi_z} + a_z^\dagger e^{i\phi_z}\right)\left(c_1^\dagger c_2 e^{i(\phi_1-\phi_2)} + c_2^\dagger c_1 e^{-i(\phi_1-\phi_2)}\right) \propto \langle c_1\rangle \equiv 0. \tag{H5}$$

The phase of the boson field c_1 can always compensate for the restricted phase of c_2. Note that we assume that level $|1\rangle$ is unoccupied before increasing η, and thus the phase of c_1 can be changed arbitrarily. The system is therefore stable against quenches $\eta < \eta^c$. This behavior arises from the fact that each photon mode is not coupled to all atomic levels; symmetry breaking in one interaction term does not imply explicit symmetry breaking in another. More precisely, when $\eta_s > \eta_s^c$ and $\eta = 0$, one finds that

$$\begin{aligned} c_1^\dagger c_1 &= 0, \\ c_2^\dagger c_2 &= \frac{(1-2J^z)}{2}, \\ c_3^\dagger c_3 &= \frac{(1+2J_z)}{2}, \end{aligned} \tag{H6}$$

and after the quench of η, we get $a_z \propto (c_1^\dagger c_2 + c_2^\dagger c_1) = 0$ and the subsystem remains in steady state as long as $\eta/\eta^c < \eta_s/\eta_s^c$. The absence of restrictions on phase ϕ_1 makes it impossible to induce competing conditions and push the subsystem out of equilibrium. Indeed, in the case of four levels, one cannot manipulate the phase of a single boson separately, thereby resulting in the existence of long-lived oscillations of the auxiliary cavity field and the precession of corresponding pseudospins.

[1] J. J. Sakurai and E. D. Commins, *Modern quantum mechanics, revised edition* (Addison-Wesley Pub. Co., 1995).

[2] J. E. Hirsch, Spin Hall effect, Phys. Rev. Lett. **83**, 1834 (1999).

[3] M. Z. Hasan and C. L. Kane, Colloquium: Topological insulators, Rev. Mod. Phys. **82**, 3045 (2010).

[4] M. Sato and Y. Ando, Topological superconductors: a review, Rep. Prog. Phys. **80**, 076501 (2017).

[5] J. D. Sau, R. M. Lutchyn, S. Tewari, and S. Das Sarma, Generic new platform for topological quantum computation using semiconductor heterostructures, Phys. Rev. Lett. **104**, 040502 (2010).

[6] J. Qi, Z.-H. Liu, and H. Q. Xu, Spin-orbit interaction enabled high-fidelity two-qubit gates, New J. Phys. **26**, 013012 (2024).

[7] T. Stav, A. Faerman, E. Maguid, D. Oren, V. Kleiner, E. Hasman, and M. Segev, Quantum entanglement of the spin and orbital angular momentum of photons using metamaterials, Science **361**, 1101 (2018), .

[8] S. S. Kale, Y. Ding, Y. P. Chen, B. Friedrich, and S. Kais, Spin-momentum entanglement in a bose–einstein condensate, Phys. Chem. Chem. Phys. **22**, 25669 (2020).

[9] M. T. Manzoni, L. Mathey, and D. E. Chang, Designing exotic many-body states of atomic spin and motion in photonic crystals, Nat. Commun. **8**, 14696 (2017).

[10] F. Mivehvar, F. Piazza, T. Donner, and H. Ritsch, Cavity qed with quantum gases: new paradigms in many-body physics, Adv. Phys. **70**, 1 (2021).

[11] N. Dogra, M. Landini, K. Kroeger, L. Hruby, T. Donner, and T. Esslinger, Dissipation-induced structural instability and chiral dynamics in a quantum gas, Science **366**, 1496 (2019).

[12] K. Baumann, C. Guerlin, F. Brennecke, and T. Esslinger, Dicke quantum phase transition with a superfluid gas in an optical cavity, Nature (London) **464**, 1301 (2010).

[13] R. M. Kroeze, Y. Guo, and B. L. Lev, Dynamical spin-orbit coupling of a quantum gas, Phys. Rev. Lett. **123**, 160404 (2019).

[14] J. Marino, M. Eckstein, M. Foster, and A.-M. Rey, Dynamical phase transitions in the collisionless pre-thermal states of isolated quantum systems: theory and experiments, Rep. Prog. Phys. **85**, 116001 (2022).

[15] J. Klinder, H. Keßler, M. Wolke, L. Mathey, and A. Hemmerich, Dynamical phase transition in the open Dicke model, Proc. Natl. Acad. Sci. USA **112**, 3290 (2015), .

[16] J. Skulte, P. Kongkhambut, H. Keßler, A. Hemmerich, L. Mathey, and J. G. Cosme, Parametrically driven dissipative three-level Dicke model, Phys. Rev. A **104**, 063705 (2021).

[17] P. Kongkhambut, H. Keßler, J. Skulte, L. Mathey, J. G. Cosme, and A. Hemmerich, Realization of a periodically driven open three-level Dicke model, Phys. Rev. Lett. **127**, 253601 (2021).

[18] P. Kongkhambut, J. Skulte, L. Mathey, J. G. Cosme, A. Hemmerich, and H. Keßler, Observation of a continuous time crystal, Science **377**, 670 (2022).

[19] R. J. Lewis-Swan, D. Barberena, J. R. K. Cline, D. J. Young, J. K. Thompson, and A. M. Rey, Cavity-QED quantum simulator of dynamical phases of a Bardeen-Cooper-Schrieffer superconductor, Phys. Rev. Lett. **126**, 173601 (2021).

[20] F. Carollo and I. Lesanovsky, Exactness of mean-field equations for open Dicke models with an application to pattern retrieval dynamics, Phys. Rev. Lett. **126**, 230601 (2021).

[21] K. Seetharam, A. Lerose, R. Fazio, and J. Marino, Correlation engineering via nonlocal dissipation, Phys. Rev. Res. **4**, 013089 (2022).

[22] K. Seetharam, A. Lerose, R. Fazio, and J. Marino, Dynamical scaling of correlations generated by short- and long-range dissipation, Phys. Rev. B **105**, 184305 (2022).

[23] J. Marino, Universality class of ising critical states with long-range losses, Phys. Rev. Lett. **129**, 050603 (2022).

[24] A. Periwal, E. S. Cooper, P. Kunkel, J. F. Wienand, E. J. Davis, and M. Schleier-Smith, Programmable interactions and emergent geometry in an array of atom clouds, Nature (London) **600**, 630 (2021).

[25] F. Finger, R. Rosa-Medina, N. Reiter, P. Christodoulou, T. Donner, and T. Esslinger, Spin- and momentum-correlated atom pairs mediated by photon exchange, Phys. Rev. Lett. **132**, 093402 (2024).

[26] R. Rosa-Medina, F. Ferri, F. Finger, N. Dogra, K. Kroeger, R. Lin, R. Chitra, T. Donner, and T. Esslinger, Observing dynamical currents in a non-Hermitian momentum lattice, Phys. Rev. Lett. **128**, 143602 (2022).

[27] R. Lin, R. Rosa-Medina, F. Ferri, F. Finger, K. Kroeger, T. Donner, T. Esslinger, and R. Chitra, Dissipation-engineered family of nearly dark states in many-body cavity-atom systems, Phys. Rev. Lett. **128**, 153601 (2022).

[28] J. Skulte, P. Kongkhambut, S. Rao, L. Mathey, H. Keßler, A. Hemmerich, and J. G. Cosme, Condensate formation in a dark state of a driven atom-cavity system, Phys. Rev. Lett. **130**, 163603 (2023).

[29] A. Piñeiro Orioli, J. K. Thompson, and A. M. Rey, Emergent dark states from superradiant dynamics in multilevel atoms in a cavity, Phys. Rev. X **12**, 011054 (2022).

[30] M. Soriente, T. Donner, R. Chitra, and O. Zilberberg, Dissipation-induced anomalous multicritical phenomena, Phys. Rev. Lett. **120**, 183603 (2018).

[31] M. Landini, N. Dogra, K. Kröger, L. Hruby, T. Donner, and T. Esslinger, Formation of a spin texture in a quantum gas coupled to a cavity, Phys. Rev. Lett. **120**, 223602 (2018).

[32] D. Dreon, A. Baumgärtner, X. Li, S. Hertlein, T. Esslinger, and T. Donner, Self-oscillating pump in a topological dissipative atom–cavity system, Nature (London) **608**, 494 (2022).

[33] D. Nagy, G. Kónya, G. Szirmai, and P. Domokos, Dicke-model phase transition in the quantum motion of a Bose-Einstein condensate in an optical cavity, Phys. Rev. Lett. **104**, 130401 (2010).

[34] Z. Zhiqiang, C. H. Lee, R. Kumar, K. J. Arnold, S. J. Masson, A. S. Parkins, and M. D. Barrett, Nonequilibrium phase transition in a spin-1 Dicke model, Optica **4**, 424 (2017).

[35] S. J. Masson, M. D. Barrett, and S. Parkins, Cavity QED engineering of spin dynamics and squeezing in a spinor gas, Phys. Rev. Lett. **119**, 213601 (2017).

[36] F. Ferri, R. Rosa-Medina, F. Finger, N. Dogra, M. Soriente, O. Zilberberg, T. Donner, and T. Esslinger, Emerging dissipative phases in a superradiant quantum gas with tunable decay, Phys. Rev. X **11**, 041046 (2021).

[37] R. M. Kroeze, Y. Guo, V. D. Vaidya, J. Keeling, and B. L. Lev, Spinor self-ordering of a quantum gas in a cavity, Phys. Rev. Lett. **121**, 163601 (2018).

[38] F. Mivehvar, F. Piazza, and H. Ritsch, Disorder-driven density and spin self-ordering of a Bose-Einstein condensate in a cavity, Phys. Rev. Lett. **119**, 063602 (2017).

[39] J. D. Wilson, S. B. Jäger, J. T. Reilly, A. Shankar, M. L. Chiofalo, and M. J. Holland, Beyond one-axis twisting: Simultaneous spin-momentum squeezing, Phys. Rev. A **106**, 043711 (2022).

[40] D. Nagy, G. Szirmai, and P. Domokos, Critical exponent of a quantum-noise-driven phase transition: The open-system Dicke model, Phys. Rev. A **84**, 043637 (2011).

[41] K. C. Stitely, A. Giraldo, B. Krauskopf, and S. Parkins, Lasing and counter-lasing phase transitions in a cavity-QED system, Phys. Rev. Res. **4**, 023101 (2022).

[42] A. Lerose and S. Pappalardi, Bridging entanglement dynamics and chaos in semiclassical systems, Phys. Rev. A **102**, 032404 (2020).

[43] N. Defenu, A. Lerose, and S. Pappalardi, Out-of-equilibrium dynamics of quantum many-body systems with long-range interactions, Phys. Rep. **1074**, 1 (2024).

[44] P. Kirton, M. M. Roses, J. Keeling, and E. G. Dalla Torre, Introduction to the Dicke model: From equilibrium to nonequilibrium, and vice versa, Adv. Quantum Technol. **2**, 1800043 (2019).

[45] M. A. Nielsen and I. L. Chuang, *Quantum Computation and Quantum Information: 10th Anniversary Edition* (Cambridge University Press, Cambridge, 2010).

[46] Z. Zhang, C. H. Lee, R. Kumar, K. J. Arnold, S. J. Masson, A. L. Grimsmo, A. S. Parkins, and M. D. Barrett, Dicke-model simulation via cavity-assisted Raman transitions, Phys. Rev. A **97**, 043858 (2018).

[47] O. Chelpanova, A. Lerose, S. Zhang, I. Carusotto, Y. Tserkovnyak, and J. Marino, Intertwining of lasing and superradiance under spintronic pumping, Phys. Rev. B **108**, 104302 (2023).

[48] R. H. Dicke, Coherence in spontaneous radiation processes, Phys. Rev. **93**, 99 (1954).

[49] F. Dimer, B. Estienne, A. S. Parkins, and H. J. Carmichael, Proposed realization of the Dicke-Model quantum phase transition in an optical cavity qed system, Phys. Rev. A **75**, 013804 (2007).

[50] P. Kirton and J. Keeling, Superradiant and lasing states in driven-dissipative Dicke models, New J. Phys. **20**, 015009 (2018).

[51] F. Mivehvar, Unconventional Dicke model: Multistabilities and nonequilibrium dynamics, Phys. Rev. Lett. **132**, 073602 (2024).

[52] B. P. Marsh, R. M. Kroeze, S. Ganguli, S. Gopalakrishnan, J. Keeling, and B. L. Lev, Entanglement and replica symmetry breaking in a driven-dissipative quantum spin glass, Phys. Rev. X **14**, 011026 (2024).

[53] F. Mivehvar, H. Ritsch, and F. Piazza, Cavity-quantum-electrodynamical toolbox for quantum magnetism, Phys. Rev. Lett. **122**, 113603 (2019).

[54] E. Cornfeld, M. Goldstein, and E. Sela, Imbalance entanglement: Symmetry decomposition of negativity, Phys. Rev. A **98**, 032302 (2018).

[55] W. K. Wootters, Entanglement of formation and concurrence, Quantum Info. Comput. **1**, 27 (2001).

[56] J. Zou, S. Zhang, and Y. Tserkovnyak, Bell-state generation for spin qubits via dissipative coupling, Phys. Rev. B **106**, L180406 (2022).

[57] G. Vidal and R. F. Werner, Computable measure of entanglement, Phys. Rev. A **65**, 032314 (2002).

[58] D. Huybrechts, F. Minganti, F. Nori, M. Wouters, and N. Shammah, Validity of mean-field theory in a dissipative critical system: Liouvillian gap, $\mathbb{PT}$-symmetric antigap, and permutational symmetry in the *XYZ* model, Phys. Rev. B **101**, 214302 (2020).

[59] Z. Qi, T. Scaffidi, and X. Cao, Surprises in the deep Hilbert space of all-to-all systems: From superexponential scrambling to slow entanglement growth, Phys. Rev. B **108**, 054301 (2023).

[60] F. Iemini, D. Chang, and J. Marino, Dynamics of inhomogeneous spin ensembles with all-to-all interactions: break-

ing permutational invariance, Phys. Rev. A **109**, 032204 (2024).
[61] R. J. Valencia-Tortora, S. P. Kelly, T. Donner, G. Morigi, R. Fazio, and J. Marino, Crafting the dynamical structure of synchronization by harnessing bosonic multilevel cavity QED, Phys. Rev. Res. **5**, 023112 (2023).
[62] V. Galitski and I. B. Spielman, Spin–orbit coupling in quantum gases, Nature (London) **494**, 49 (2013).
[63] S. Lorenzo, J. Marino, F. Plastina, G. M. Palma, and T. J. G. Apollaro, Quantum critical scaling under periodic driving, Sci. Rep. **7**, 5672 (2017).
[64] S. S. Szigeti, O. Hosten, and S. A. Haine, Improving cold-atom sensors with quantum entanglement: Prospects and challenges, Appl. Phys. Lett. **118**, 140501 (2021).
[65] S. Colombo, E. Pedrozo-Peñafiel, and V. Vuletić, Entanglement-enhanced optical atomic clocks, Appl. Phys. Lett. **121**, 210502 (2022).
[66] G. P. Greve, C. Luo, B. Wu, and J. K. Thompson, Entanglement-enhanced matter-wave interferometry in a high-finesse cavity, Nature (London) **610**, 472 (2022).
[67] F. Brennecke, R. Mottl, K. Baumann, R. Landig, T. Donner, and T. Esslinger, Real-time observation of fluctuations at the driven-dissipative Dicke phase transition, Proc. Natl. Acad. Sci. USA **110**, 11763 (2013).
[68] M. J. Bhaseen, J. Mayoh, B. D. Simons, and J. Keeling, Dynamics of nonequilibrium Dicke models, Phys. Rev. A **85**, 013817 (2012).
[69] We also tried sampling various initial states and comparing dynamics. Our general observation is the oscillatory behavior is quite generic and repeats from simulation to simulation. However, the frequency of oscillations may depend on the initial state.
[70] F. Damanet, A. J. Daley, and J. Keeling, Atom-only descriptions of the driven-dissipative Dicke model, Phys. Rev. A **99**, 033845 (2019).
[71] S. B. Jäger, T. Schmit, G. Morigi, M. J. Holland, and R. Betzholz, Lindblad master equations for quantum systems coupled to dissipative bosonic modes, Phys. Rev. Lett. **129**, 063601 (2022).
[72] J. Keeling, M. J. Bhaseen, and B. D. Simons, Collective dynamics of Bose-Einstein condensates in optical cavities, Phys. Rev. Lett. **105**, 043001 (2010).
[73] T. Bhore, J.-Y. Desaules, and Z. Papi, Deep thermalization in constrained quantum systems, Phys. Rev. B **108**, 104317 (2023).
[74] R. J. Valencia-Tortora, N. Pancotti, and J. Marino, Kinetically constrained quantum dynamics in superconducting circuits, PRX Quantum **3**, 020346 (2022).
[75] A. Pineiro Orioli and A. M. Rey, Subradiance of multilevel fermionic atoms in arrays with filling $n \geqslant 2$, Phys. Rev. A **101**, 043816 (2020).
[76] C. Hotter, L. Ostermann, and H. Ritsch, Cavity sub- and superradiance for transversely driven atomic ensembles, Phys. Rev. Res. **5**, 013056 (2023).
[77] B. Sundar, D. Barberena, A. M. Rey, and A. P. Orioli, Squeezing multilevel atoms in dark states via cavity superradiance, Phys. Rev. Lett. **132**, 033601 (2024).
[78] A. Asenjo-Garcia, H. J. Kimble, and D. E. Chang, Optical waveguiding by atomic entanglement in multilevel atom arrays, Proc. Natl. Acad. Sci. USA **116**, 25503 (2019).
[79] S. J. Masson and A. Asenjo-Garcia, Universality of Dicke superradiance in arrays of quantum emitters, Nat. Commun. **13**, 2285 (2022).
[80] E. Sierra, S. J. Masson, and A. Asenjo-Garcia, Dicke superradiance in ordered lattices: dimensionality matters, Phys. Rev. Res. **4**, 023207 (2022).
[81] C. Tabares, A. Muñoz de las Heras, L. Tagliacozzo, D. Porras, and A. González-Tudela, Variational quantum simulators based on waveguide QED, Phys. Rev. Lett. **131**, 073602 (2023).
[82] J. T. Reilly, S. B. Jäger, J. D. Wilson, J. Cooper, S. Eggert, and M. J. Holland, Speeding up squeezing with a periodically driven Dicke model, Phys. Rev. Res. **6**, 033090 (2024).
[83] B. Buča and D. Jaksch, Dissipation induced nonstationarity in a quantum gas, Phys. Rev. Lett. **123**, 260401 (2019).
[84] http://hpc.uni-mainz.de.
[85] R. Ul Haq, S. S. Bharadwaj, and T. A. Wani, An explicit method for schrieffer-wolff transformation, arXiv:1901.08617.
[86] D. A. Steck, Rubidium 87 d line data (unpublished), http://steck.us/alkalidata.
[87] O. V. Sinkin, R. Holzlöhner, J. Zweck, and C. R. Menyuk, Optimization of the split-step fourier method in modeling optical-fiber communications systems, J. Lightwave Technol. **21**, 61 (2003).

CHAPTER 5

Beyond mean-field and Lindblad

This chapter of the thesis covers quantum aspects of the dynamics and discusses the relevance of correlations and how they can be captured via developed semiclassical method. For simplicity, we consider interacting dissipative spin models, that, for instance, emerge by adiabatic elimination of the cavity photons or describe evolution of the array of Rydberg atoms, as well as a free-space radiation of atomic arrays. The results are derived with the Keldysh path integral technique [97]. We study a particular example of spin decay, dephasing, and correlated dissipations, as well as revisit spontaneous decay in the presence of a non-Markovian environment.

5.1. Introduction

The models studied so far in this thesis are collective, and in the thermodynamic limit, all quantum effects are averaged out, making such a system classical, enabling mean-field description[1]. The follow-up direction is to concentrate on finite-range driven-dissipative models. Here, the exchange of the photon happens between only neighboring atoms, resulting in correlations that can not be tailored on the mean-field level.

The exact evaluation of the quantum dynamics of the system can be numerically impossible (unless the system contains dozens of spins at most) and does not bring too many gains. Methods such as stochastic unraveling also deal with small N and require a finite temperature [100]. The tensor networks methods are very efficient in 1d, however in higher dimensions there are still problems and limitations, and there is another complication in the presence of the collective dissipations [101]. At the same time, in many practical situations, quantum fluctuations average out, and overall dynamics are mostly classical (at least, at small timescales). For such cases, there is no need to solve quantum problems, and its (semi-)classical limit can be sufficient. One such semi-classical approach – discrete truncated Wigner approximation (DTWA) – consists of simulating the dynamics of multiple classical spins and then averaging over possible initial conditions [102–108]. While this method works very well for closed systems, it

[1]Note that this statement depends on the initial state of the system. If we initialize the system in the non-Gaussian state or exclude permutation invariance of particles, quantum effects arise; thus, the mean-field description becomes invalid [98, 99]. These cases are beyond the scope of this thesis.

has been a question on how to evaluate classical spin dynamics for dissipative systems. Below we give a short description of the method and then derive dissipative dynamics with the Keldysh path integral.

5.2. Model and semiclassical description of driven-dissipative dynamics

In this Chapter, we concentrate on the dissipative spin models. First, such models can be derived from studies in the previous chapters by adiabatic elimination of the photon fields. Also, there are simulators, such as Rydberg atoms, trapped ions, or NV centers, which can be naturally expressed via spin degrees of freedom.

We consider Hamiltonian of the general form

$$\hat{H} = \sum_{\alpha} \sum_{i=1}^{N} \Omega^{\alpha} \hat{\sigma}_i^{\alpha} + \frac{1}{2} \sum_{\alpha,\beta} \sum_{i \neq j}^{N} J_{ij}^{\alpha\beta} \hat{\sigma}_i^{\alpha} \hat{\sigma}_j^{\beta} \tag{5.1}$$

with couplings $J_{ij}^{\alpha\beta} = J_{ji}^{\alpha\beta} = J_{ij}^{\beta\alpha}$ and driving fields Ω^{α}. The dynamics of the spin ensemble are given by the Lindblad master equation (2.1) with dissipation rates γ_i. We consider the following dissipation channels

- Spin loss with $\gamma_i = \gamma$ and $\hat{L}_i = \hat{\sigma}_i^- = (\hat{\sigma}_i^x - i\hat{\sigma}_i^y)/2$;
- Spin dephasing with $\gamma_i = \kappa$ and $\hat{L}_i = \hat{\sigma}_i^z$;
- Collective spin loss when the dissipator takes a more general form $\sum_{mn} \Gamma_{mn} \left(2\hat{\sigma}_m^- \hat{\rho} \hat{\sigma}_n^+ - \hat{\sigma}_m^+ \hat{\sigma}_n^- \hat{\rho} - \hat{\rho} \hat{\sigma}_m^+ \hat{\sigma}_n^-\right)/2$, and the collective decay rates are given by eigenvalues of Γ_{ij}: $\Gamma_{nm} = V_{mi} D_{ii} V_{in}^{-1}$, $\gamma_i = D_{ii}$, $\hat{L}_i = \sum_m \hat{\sigma}_m^- V_{mi}$.

The non-local terms in (5.1) give rise to the dynamical build-up of correlations between different spins even if initially the ensemble were prepared in the product state,

$$|\Psi\rangle_0 = |\uparrow\rangle_1 \otimes \ldots \otimes |\uparrow\rangle_N . \tag{5.2}$$

As such, to solve the dynamics numerically, one needs to go beyond mean-field approximation. One way to proceed is to use the semiclassical Truncated Wigner Approximation method, according to which quantum uncertainty is substituted by the statistical variance. The method consists of building one-to-one correspondence between operators in the Hilbert space and functions in the phase space through the corresponding phase-point operator $\hat{A}$ and calculating observables as statistical averages over the phase space [102–108]. Precisely, one maps operators to the function in the appropriate phase space by calculating the so-called Weyl symbol of the operator, $O(\boldsymbol{\psi}, \overline{\boldsymbol{\psi}}) = \mathrm{Tr}[\hat{O}\left(\boldsymbol{\psi}, \boldsymbol{\psi}^{\dagger}\right) \hat{A}\left(\boldsymbol{\psi}, \boldsymbol{\psi}^{\dagger}\right)]$ (here, $\boldsymbol{\psi}, \boldsymbol{\psi}^{\dagger}$ are states in the Hilbert phase and $\boldsymbol{\psi}, \bar{\boldsymbol{\psi}}$ are corresponding states in the phase space; $\bar{\boldsymbol{\psi}}$ denotes a complex

conjugate of $\boldsymbol{\psi}$). The density matrix similarly is mapped to the Wigner function $W(\boldsymbol{\psi},\overline{\boldsymbol{\psi}}) = \mathrm{Tr}\left[\hat{\rho}\hat{A}\left(\boldsymbol{\psi},\boldsymbol{\psi}^{\dagger}\right)\right]$ which physical sense is the quasi-probability distribution of different states in the phase space. Then, the observables are given by averaging the corresponding Weyl symbol over the phase space with the quasi-probability distribution W, $\langle\hat{O}\left(\boldsymbol{\psi},\boldsymbol{\psi}^{\dagger}\right)\rangle = \iint \mathrm{d}\boldsymbol{\psi}\mathrm{d}\overline{\boldsymbol{\psi}}W(\boldsymbol{\psi},\overline{\boldsymbol{\psi}})O(\boldsymbol{\psi},\overline{\boldsymbol{\psi}})$.

To evaluate dynamics of observables according to TWA, in the lowest order of the effective Plank constant (semi-classically), one takes into account uncertainty in the initial conditions, but dynamics of phase-space functions O is fully classical, with equations of motion given by the Poisson bracket of this operator with the Weyl symbol of the Hamiltonian, $\dot{O}_c(\boldsymbol{\psi},\overline{\boldsymbol{\psi}},t) = \{O,\mathcal{H}_0\}_P$. Then, at arbitrary time moment t observables are given by the phase-space averaged of $O(\boldsymbol{\psi},\overline{\boldsymbol{\psi}},t)$ over all realization of initial conditions, given by W_0,

$$\langle\hat{O}(\hat{\boldsymbol{\psi}},\hat{\boldsymbol{\psi}}^{\dagger},t)\rangle = \iint d\boldsymbol{\psi}_0 d\bar{\boldsymbol{\psi}}_0 W_0(\boldsymbol{\psi}_0,\overline{\boldsymbol{\psi}}_0)O(\boldsymbol{\psi}(t),\overline{\boldsymbol{\psi}}(t),t). \tag{5.3}$$

For spins, the convenient choice is to consider continuous coherent phase space since spin models could be mapped to the interacting boson model by use of Swinger boson or Holstein-Primakoff approximations [64]. Such a method has been shown to work well for large spins and for collective models [102, 109]. For spins-1/2 instead, the convenient choice is to adopt the *discrete* phase-point operator $\hat{A}$ and follow the so-called discrete TWA (DTWA) approach [106].

Without going into details (curious readers are referred to the Appendix and Refs. [102, 104, 105, 108]), we consider a standard numerical implementation of DTWA in the case when all spins are initialized in the product state, polarized along z direction.

(1) Sample n_{tr} initial states according to Wigner quasi-probability distribution

$$\begin{aligned} W\left(\mathbf{s}_i\right) =& \frac{1}{4}\delta\left(s_i^z+1\right)\left[\delta\left(s_i^x+1\right)+\delta\left(s_i^x-1\right)\right] \\ &\times\left[\delta\left(s_i^y+1\right)+\delta\left(s_i^y-1\right)\right]. \end{aligned} \tag{5.4}$$

where index i refers to the $i-$th spin, and $\mathbf{s}$ is the classical spin in the phase space with the radius $\sqrt{3}$. Here, we initialize each classical spin with $s_{i,k}^z = 1$, but can choose with equal probability $s_{i,k}^{x,y} = \pm 1$. We introduce the additional index $k = 1,\ldots,n_{tr}$ that refers to the realization of the initial state. Thus, when averaged over n_{tr} realizations of the initial conditions, one gets correct first and second momenta for state (5.2), $\langle\sum_i \hat{\sigma}_i^z\rangle = N$, $\langle\sum_i \hat{\sigma}_i^{x,y}\rangle = 0$, $\langle\sum_{ij}\hat{\sigma}_i^{x,y}\hat{\sigma}_j^{x,y}\rangle = N$.

(2) Evaluate dynamics for spins according to classical equations of motion. For each of n_{tr} initial conditions evaluate $\boldsymbol{s}_{i,k}(t)$, where $i = 1,\ldots,N$ and $k = 1,\ldots,n_{tr}$.

(3) Evaluate observables, which in the classical limit are given as the average over different realizations of initial conditions,

$$\begin{aligned} \langle \hat{\sigma}_i^{\alpha}(t) \rangle &= \frac{1}{n_{trj}} \sum_{j=1}^{n_{trj}} s_{i,j}^{\alpha}(t) \\ \langle \{ \hat{\sigma}_i^{\alpha}(t) \hat{\sigma}_k^{\beta}(t) \}_s \rangle &= \frac{1}{n_{trj}} \sum_{j=1}^{n_{trj}} s_{i,j}^{\alpha}(t) s_{k,j}^{\beta}(t). \end{aligned} \tag{5.5}$$

Here $\alpha, \beta \in \{x, y, z\}$.

This simple algorithm has shown tremendous results for the dynamics of spin systems. In particular, it is capable of simulating dynamics of integrable Ising chains [106], capturing revivals; for evaluation of squeezing in short interacting models, and so on. Despite its simplicity and ease of implementation, the method matches exact diagonalization or density matrix renormalization group for a wide class of the model, at least at the early stages of the dynamics. Furthermore, the higher order corrections in the effective Plank constant could, in principle, also be targeted by combining truncated Wigner approximation (TWA) with the BBGKY hierarchy [110, 111].

The DTWA method has also been used to simulate the dynamics of the dissipative spin chains given by the Lindblad master equation. In Ref. [112], the deterministic dynamics was giving reasonable results for a short times $t \ll \gamma_i^{-1}$; however, naive evaluation of spin dynamics $\boldsymbol{s}_i$ according to mean-field equations of motion results in fundamentally wrong semi-classical dynamics at later times. In the presence of dissipation, the dynamics of classical fields converge to the steady-state attractor, diminishing quantum uncertainty over time. As the vast majority of quantum simulators operate in the presence of dissipations, and, most importantly, there are many proposals to use dissipations for engineering non-trivial dynamical phases, entanglement, squeezed states and controlled spread of correlations, the DTWA method needs modification to be efficient for exploring that kind of problems.

To overcome the artificial suppression of correlations, the deterministic evolution of spins should be replaced with the stochastic one [47, 61, 105], turning equations of motion for the classical spins into

$$\dot{s}^{\mu}(t) = \{ s^{\mu}, \mathcal{H}_0 \}_P + \dot{s}^{\mu}_{\text{dissip}}(t). \tag{5.6}$$

The $\dot{s}^{\mu}_{\text{dissip}}(t)$, in general, contains two contributions: dissipation, which makes the spin chain relax towards the correct steady state, and corresponding multiplicative noise term, which preserves the uncertainty over the course of the dynamics. The expression for $\dot{s}^{\mu}_{\text{dissip}}(t)$ can be obtained directly from the microscopic derivation [113], however, if the microscopic details of the problem are not known, some other methods are needed.

Starting from the quantum Langevin equation, stochastic spin dynamics can be obtained if mapping quantum noise to the classical random process [105]. However, the naive implementation of this mapping results in shrinking the spin length with time and non-physical results. By adjusting noise processes, the spin magnitude can be preserved. However, the expression for the noise process, in this case, should be guessed rather than derived. Alternatively, in Ref. [104], authors reported discrete-continuous TWA, which allows for numerical simulation of system dynamics with stronger dissipation. In particular, the method works very well for simulating the dynamics of driven atomic arrays. Also, it can be adopted for simulating dynamics for spin-boson models and shows good convergence to the exact dynamics in particular cases [103]. However, derivation of the stochastic equations of motion in this case can be challenging. Another way consists of unraveling dynamics back to its microscopics. Knowing details of the bath that induces dissipations to the system, one can derive stochastic Bloch equations of motions [114]. However, in some cases, such microscopic details are omitted, and there is no access to the bath details.

Below, we show how a similar derivation of classical stochastic equations of motion can be done using the formalism of Keldysh path integrall [64, 97]. The motivation stems from the formal way to express $\dot{s}^{\mu}_{\text{dissip}}(t)$ via Poisson bracket with the stochastic classical Hamiltonian term

$$H_{diss} = \sum_{m} \bar{\Phi}_m \boldsymbol{L}_m + \bar{\boldsymbol{L}}_m \Phi_m, \tag{5.7}$$

where $\boldsymbol{L}_m$ is the Weyl symbol for the jump operator, and the field Φ_m depends self-consistently on $\boldsymbol{L}_m$ itself plus contains stochastic contribution, $\Phi \propto \boldsymbol{L} + \eta$. Within Keldysh path integral framework, Φ can be found as a result of Hubbard-Stratonovich (HS) transformation of the action term, induced by Lindbladian (cf. derivation of the Langevin equation in Ref. [97]).

Providing details in the next Section, the overall procedure of derivation can be briefly summarized by the following steps:

(1) Choose an appropriate representation for spins suitable for the path integral technique. In our case, we followed the Swinger boson representation.
(2) Write down the Keldysh action for the Lindbladian term.
(3) (*) Perform HS transformation for the dissipator term. The resultant part of the action corresponds to effective Hamiltonian $\bar{L}_m \Phi_m + c.c.$ plus the term quadratic in Φ_m
(4) Perform Keldysh rotation from forward and backward fields to classical and quantum. Our goal is to treat quantum fields perturbatively.

(5) Use another HS transformation to linearize quadratic term in quantum fields, $\propto \bar{\phi}_q \phi_q$,
$\exp\left(\int dt \left[\frac{(2i)}{\gamma}\bar{\phi}^q_n(t)\phi^q_n(t)\right]\right) = \int \mathbf{D}[\xi(t),\bar{\xi}(t)]$
$\exp\left(\int \mathrm{d}t \left[-\bar{\xi}_n(t)\frac{\gamma}{2i}\xi_n(t) + \bar{\xi}_n(t)\phi^q_n(t) + \bar{\phi}^q_n(t)\xi_n(t)\right]\right)$. This second HS field ξ is nothing but the stochastic force with the variance $\langle \xi_n(t)\bar{\xi}_m(t')\rangle = 2\gamma\delta(t-t')\delta_{n,m}$.

(6) Neglect terms, which contain quantum fields above the linear order; Integrate out quantum fields and obtain equations of motion for the HS fields Φ_m and other classical fields, which were used in step (1) for spin representation.

(7) Re-express equations of motions for spins in terms of classical fields in (6).

Note that the step number (3*) above is optional, and its only benefit is a physical intuition. The noise terms in equations of motion with and without step (3*) are slightly different, but the resulting dynamics are identical.

5.3. Derivation of the Langevin equation for spins

We consider dissipative dynamics (the Hamiltonian part can be considered separately) given by the Lindblad master equation of the form

$$\dot{\hat{\rho}} = \sum_i \gamma_i \left(\hat{L}_i \hat{\rho} \hat{L}_i^\dagger - \frac{1}{2}\left\{ \hat{L}_i^\dagger \hat{L}_i, \hat{\rho} \right\} \right). \tag{5.8}$$

On the Keldysh contour, Eq. (5.8) corresponds to the following term in the Keldysh action [97, 114]

$$S_d = -i \int \mathrm{d}t \sum_a \frac{\gamma_a}{2} \left(2L_a^+ \bar{L}_a^- - L_a^- \bar{L}_a^- - L_a^+ \bar{L}_a^+ \right). \tag{5.9}$$

We write down a Keldysh action on closed time contour, denoting via subscripts '+' and '−' corresponding fields on the forward and backward time contours.

The fields L_a correspond to jump operators in the appropriate representation. Here, for convenience, we use Swinger-boson representation [64], according to which boson annihilation operators $\hat{a}_i$ ($\hat{b}_i$) correspond to the annihilation of the particle in the ground (excited) state of the two-level system. Thus, spin operators are built in the following way

$$\begin{aligned} \hat{\sigma}_i^+ &= \hat{b}_i^\dagger \hat{a}_i \\ \hat{\sigma}_i^z &= \hat{b}_i^\dagger \hat{b}_i - \hat{a}_i^\dagger \hat{a}_i, \end{aligned} \tag{5.10}$$

where boson operators $\hat{a},\ \hat{b}$ satisfy canonical commutation relations. Then, we can use bosonic coherent state representation, for which the free part of the action is given via $S_0 = \int \mathrm{d}t \sum_a \left[\bar{a}_a^+ i\partial_t a_a^+ + \bar{b}_a^+ i\partial_t b_a^+ - \bar{a}_a^- i\partial_t a_a^- - \bar{b}_a^- i\partial_t b_a^-\right]$.

According to the Swinger boson representation, spins are quadratic in bosonic operators. Thus, terms in the dissipative part of the action in Eq. (5.9) are of the fourth order in terms of appropriate fields $a,\ b$. Such a four-particle process can be decoupled via HS transformation into the interaction of two particles via a new HS field Φ_m. By absorbing a minus sign into jump fields L^- the dissipative part of the action reads

$$\begin{aligned} S_d &= \sum_a \int dt \begin{pmatrix} -\bar{L}_a^- & \bar{L}_a^+ \end{pmatrix} \begin{pmatrix} i\gamma_a/2 & 0 \\ i\gamma_a & i\gamma_a/2 \end{pmatrix} \begin{pmatrix} -L_a^- \\ L_a^+ \end{pmatrix} \\ &\equiv \sum_a \int dt \bar{X}_a D_a X_a. \end{aligned} \tag{5.11}$$

Then, following the Hubbard-Stratonovich transformation [64], this term can be rewritten as

$$\begin{aligned} Z_d &= \int \mathbf{D}[\bar{\phi}, \phi] \mathrm{e}^{i\sum_a \int dt \bar{X}_a D_a X_a} = \\ &= \int \mathbf{D}[\bar{\phi}, \phi] \mathbf{D}[\bar{\Phi}, \Phi] \mathrm{e}^{i\int \mathrm{d}t \sum_a \left(-\bar{\Phi}_a D_a^{-1} \Phi_a + \bar{X}_a \Phi_a + \bar{\Phi}_a X_a\right)}, \end{aligned} \tag{5.12}$$

with $\phi = \{a_1, \ldots, a_N, b_1 \ldots, b_N\}$, $\Phi_a = (\Phi_a^-, \Phi_a^+)^T$, $X_a = (-\bar{L}_a^-, L_a^+)$, and

$$D_a^{-1} = \begin{pmatrix} -2i/\gamma_a & 0 \\ 4i/\gamma_a & -2i/\gamma_a \end{pmatrix}. \tag{5.13}$$

The dissipative part of the action, $S_d = S_1 + S_2$, can be split into two parts: the first one describes the coupling of the jump fields to the HS ones

$$S_1 = \int \mathrm{d}t \sum_a \bar{\Phi}_a^+ L_a^+ + \bar{L}_a^+ \Phi_a^+ - \bar{\Phi}_a^- L_a^- - \bar{L}_a^- \Phi_a^-. \tag{5.14}$$

The second part determines the free evolution of the Φ_n:

$$S_2 = \int \mathrm{d}t \sum_a 2i\gamma_a (\bar{\Phi}_a^+ \Phi_a^+ + \bar{\Phi}_a^- \Phi_a^-) - 4i/\gamma_a \bar{\Phi}_a^- \Phi_a^+. \tag{5.15}$$

In this notation, the part (5.14) can be considered as the mapping of the effective Hamiltonian (5.7) onto the Keldysh contour while, as we show below, Eq. (5.20) determines the self-consistent dependence of Φ on L and appropriate noise term. To illustrate

these, we proceed by performing Keldysh rotation, following

$$\begin{aligned}\sqrt{2}\phi_a^c(t) &= \phi_a^+ + \phi_a^- \\ \sqrt{2}\phi_a^q(t) &= \phi_a^+ - \phi_a^- \\ \sqrt{2}\Phi_a^c(t) &= \Phi_a^+ + \Phi_a^- \\ \sqrt{2}\Phi_a^q(t) &= \Phi_a^+ - \Phi_a^-\end{aligned} \tag{5.16}$$

Similarly, we can also introduce new symmetric and anti-symmetric combinations for jump fields (which include both ϕ^c and ϕ^q when substituted explicitly)

$$\begin{aligned}L_a^c &= \frac{L_a^+ + L_a^-}{2}; \\ L_a^q &= \frac{L_a^+ - L_a^-}{2}.\end{aligned} \tag{5.17}$$

In this notation,

$$S_1 = \sqrt{2}\int \mathrm{d}t \sum_a \bar{\Phi}_a^c L_a^q + \bar{L}_a^q \Phi_a^c + \bar{\Phi}_a^q L_a^c + \bar{L}_a^c \Phi_a^q \tag{5.18}$$

and

$$S_2 = \int \mathrm{d}t \sum_a 2i/\gamma_a(\bar{\Phi}_a^q \Phi_a^c - \bar{\Phi}_a^c \Phi_a^q) + 4i/\gamma \bar{\Phi}_a^q \Phi_a^q. \tag{5.19}$$

The quadratic quantum term $S_2 = \int \mathrm{d}t \sum_a 4i/\gamma \bar{\Phi}_a^q \Phi_a^q$ can be linearized by the use of another Hubbard-Stratonovich transformation, resulting into

$$S_2 = S_2^* + \int \mathrm{d}t \sum_a \frac{2i}{\gamma_a}(\bar{\Phi}_a^q \Phi_a^c - \bar{\Phi}_a^c \Phi_a^q), \tag{5.20}$$

with

$$S_2^* = \int \mathrm{d}t \sum_a -\frac{\gamma_a}{4i}\bar{\xi}_a \xi_a + \bar{\Phi}_a^q \xi_a + \bar{\xi}_a \Phi_a^q. \tag{5.21}$$

Finally, by integrating out Φ_a^q, the values of classical HS fields Φ_a^c are given by

$$\Phi_a^c = \frac{i\gamma_a}{\sqrt{2}} L_a^c + \frac{i\gamma_a}{2}\xi_a \tag{5.22}$$

and the variance of the noise equals $\langle \xi_a(t)\bar{\xi}_b(t')\rangle = 4\delta_{a,b}\delta(t-t')/\gamma_a$.

Similarly, by keeping terms not higher than linear in quantum fields ϕ_a^q and integrating them out, one derives equations of motion for ϕ_a^c. Then, the dynamics for classical spins, which are a symmetric combinations of the classical fields on positive and negative parts of the contour, can be derived through the chain rule, following the connection

between classical spins and bosons.

$$\begin{aligned} s_i^+ &= \frac{\bar{b}_i^+ a_i^+ + \bar{b}_i^- a_i^-}{2} \approx \frac{\bar{b}_i^c a_i^c}{2} \\ s_i^z &= \frac{\bar{b}_i^+ b_i^+ + \bar{b}_i^- b_i^- - \bar{a}_i^+ a_i^+ - \bar{a}_i^- a_i^-}{2} \approx \frac{\bar{b}_i^c b_i^c - \bar{a}_i^c a_i^c}{2} \end{aligned} \tag{5.23}$$

Note that factor $1/2$ appears in the expression to the classical field with respect to the operators representation in Eq. (5.10). As such, for spin loss $L_a^c = \bar{a}_a^c b_a^c/2 \equiv s_a^-$, and for spin dephasing $L_a^c = (\bar{b}_a^c b_a^c - \bar{a}_a^c a_a^c)/2 \equiv s_a^z$.

5.4. Implementation

5.4.1. *Spin loss*

The Eq. (5.22) connects the HS field with the corresponding jump operator and Gaussian noise. For instance, for the spin loss, the HS fields are

$$\Phi_a^c = \frac{i\gamma}{\sqrt{2}} s_a^- + \frac{i\gamma}{2}\xi_a. \tag{5.24}$$

The dissipative part of the dynamics of classical spins is given by

$$\begin{aligned} \dot{s}_a^- &= -\frac{i}{\sqrt{2}} s_a^z \Phi_a^c \\ \dot{s}_a^z &= -i\sqrt{2}(s_a^- \bar{\Phi}_a^c - s_a^+ \Phi_a^c) \end{aligned} \tag{5.25}$$

which, after explicit substitution of Φ_a and some further algebra, gives the following dynamics

$$\begin{aligned} \dot{s}_a^x &= \frac{\gamma}{2} s_a^x s_a^z + \frac{\gamma}{\sqrt{2}} \xi_a' s_a^z \\ \dot{s}_a^y &= \frac{\gamma}{2} s_a^y s_a^z - \frac{\gamma}{\sqrt{2}} \xi_a'' s_a^z \\ \dot{s}_a^z &= -\frac{\gamma}{2}(s_a^x s_a^x + s_a^y s_a^y) - \frac{\gamma}{\sqrt{2}}(s_a^x \xi_a' - s_a^y \xi_a'') \end{aligned} \tag{5.26}$$

where $\xi_a' = \mathrm{Re}\{\xi_a\}$, $\xi_a'' = \mathrm{Im}\{\xi_a\}$, and $\langle \xi_a'(t)\xi_b'(t')\rangle = \langle \xi_a''(t)\xi_b''(t')\rangle = 2\delta_{a,b}\delta(t-t')/\gamma$. Note that the equations of motion conserve the total magnitude of the classical spin $\partial_t(s_a^x s_a^x + s_a^y s_a^y + s_a^z s_a^z) = 0$.

We simulated the dynamics of a single spin, prepared in the $|\uparrow\rangle$ state under the spontaneous decay with the rate γ and benchmark our DTWA result to the exact solution, given by $\sigma^x = \sigma^y = 0$ and $\sigma^z = 2e^{-\gamma t} - 1$, see Fig. 5.1. At early times, the method captures dynamics extremely well. At times $\propto \gamma^{-1}$, the DTWA result starts deviating from the exact solution. The reason for that is that during dynamics, the quantum correlations start to build up, and semiclassical description becomes invalid;

γ_i	$\hat{L}_i$	$\dot{s}^{\mu}_{\text{dissip}}(t)$	Noise variance
γ	$\hat{\sigma}_i^-$	$\dot{s}^x_m = \frac{\gamma}{2} s^x_m s^z_m + \xi^{\gamma''}_m s^z_m$ $\dot{s}^y_m = \frac{\gamma}{2} s^y_m s^z_m + \xi^{\gamma'}_m s^z_m$ $\dot{s}^z_m = -\frac{\gamma}{2}\left(s^x_m s^x_m + s^y_m s^y_m\right)$ $-\left(\xi^{\gamma'}_m s^y_m + \xi^{\gamma''}_m s^x_m\right)$	$\langle \xi^{\gamma}_a(t)\bar{\xi}^{\gamma}_b(t')\rangle = 2\gamma\delta(t-t')\delta_{ab}$ $\xi^{\gamma'}_m = \text{Re}\{\xi^{\gamma}_m\}$ $\xi^{\gamma''}_m = \text{Im}\{\xi^{\gamma}_m\}$
$\gamma_\uparrow$	$\hat{\sigma}_i^+$	$\dot{s}^x_m = -\frac{\gamma_\uparrow}{2} s^x_m s^z_m - \xi^{\gamma''}_m s^z_m$ $\dot{s}^y_m = -\frac{\gamma_\uparrow}{2} s^y_m s^z_m + \xi^{\gamma'}_m s^z_m$ $\dot{s}^z_m = \frac{\gamma_\uparrow}{2}\left(s^x_m s^x_m + s^y_m s^y_m\right)$ $+\left(-\xi^{\gamma'}_m s^y_m + \xi^{\gamma''}_m s^x_m\right)$	$\langle \xi^{\gamma}_a(t)\bar{\xi}^{\gamma}_b(t')\rangle = 2\gamma_\uparrow\delta(t-t')\delta_{ab}$ $\xi^{\gamma'}_m = \text{Re}\{\xi^{\gamma}_m\}$ $\xi^{\gamma''}_m = \text{Im}\{\xi^{\gamma}_m\}$
κ	$\hat{\sigma}_i^z$	$\dot{s}^x_m = \xi^{\kappa}_m s^y_m$ $\dot{s}^y_m = -\xi^{\kappa}_m s^x_m$ $\dot{s}^z_m = 0$	$\langle \xi^{\kappa}_a(t)\,\xi^{\kappa}_b(t')\rangle = 4\kappa\delta(t-t')\,\delta_{ab}$
$D_{ii} = \sum_{m,n} V^{-1}_{im}\Gamma_{mn}V_{ni}$	$\sum_m \hat{\sigma}^-_m V_{mi}$	$\dot{s}^x_m = \frac{1}{2}\sum_n s^x_n \Gamma_{nm} s^z_m + \xi^{''}_m s^z_m$ $\dot{s}^y_m = \frac{1}{2}\sum_n s^y_n \Gamma_{nm} s^z_m + \xi^{'}_m s^z_m$ $\dot{s}^z_m = -\sum_n \frac{1}{2}\left(s^x_m \Gamma_{mn} s^x_n + s^y_n \Gamma_{nm} s^y_m\right)$ $-\left(\xi^{''}_m s^x_m + \xi^{'}_m s^y_m\right)$	$\langle \xi_\mu(t)\,\bar{\xi}_\nu(t')\rangle = 2D_{\nu\nu}\delta(t-t')\,\delta_{\mu\nu}$ $\xi_m = \xi^q_\nu V^{-1}_{\nu m}$ $\xi^{'}_m = \text{Re}\{\xi_m\}$ $\xi^{''}_m = \text{Im}\{\xi_m\}$

TABLE 5.1. Dissipation induced contributions to equations of motion $\dot{s}^{\mu}_{\text{dissip}}(t)$ for different dissipation channels.

higher order corrections are needed to retrieve the correct steady state at late times. The accumulated error results in shrinking the radius of the Block sphere from 1 to $\sqrt{3}/2$.

5.4.2. *Spin dephasing*

Similarly, in the case of spin dephasing given by jump operators $\hat{L}_i = \hat{\sigma}^z_i$ and dissipation rate κ, on the Keldysh contour we use $L^{\pm}_a = (\bar{b}^{\pm}_a b^{\pm}_a - \bar{a}^{\pm}_a a^{\pm}_a)$, $2L^c_a = \bar{b}^c_a b^c_a - \bar{a}^c_a a^c_a + \bar{b}^q_a b^q_a - \bar{a}^q_a a^q_a \approx$

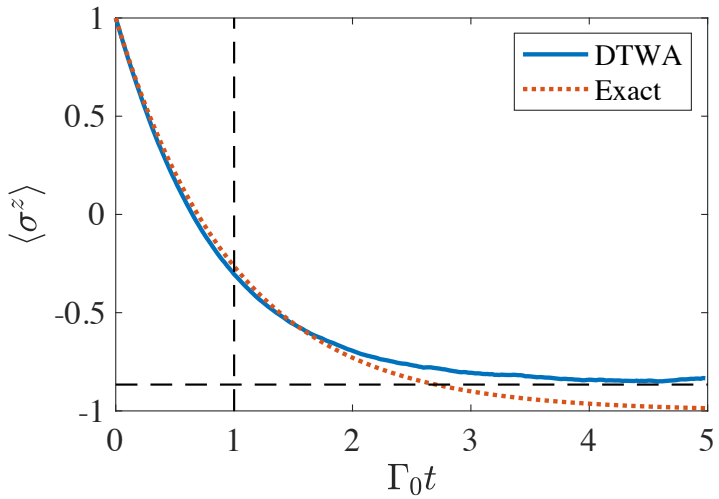

FIGURE 5.1. Dynamics of a single spin prepared in the spin-up state under spontaneous decay. The red dotted line is the exact solution, and the blue solid line is the result of the DTWA simulation.

$(\bar{b}_a^c b_a^c - \bar{a}_a^c a_a^c) = 2s_a^z$, $2L_a^q = \bar{b}_a^q b_a^c - \bar{a}_a^c a_a^q + \bar{b}_a^c b_a^q - \bar{a}_a^q a_a^c$ and $L_a^{c,q} = \bar{L}_a^{c,q}$. The effective dissipative part of the action then read

$$\begin{aligned} S_d &= i \sum_a \kappa \overbrace{\left(\bar{L}_a^q - L_a^q\right)}^{=0} s_a^z + \sum_a \bar{L}_a^q (\xi_a + \bar{\xi}_a) \\ &= \sum_a \xi_a^{'} (\bar{b}_a^q b_a^c - \bar{a}_a^c a_a^q + \bar{b}_a^c b_a^q - \bar{a}_a^q a_a^c). \end{aligned} \tag{5.27}$$

The dynamics of bosonic fields are then given by[2]

$$\begin{aligned} i\partial_t a_a^c - \xi_a^{'} a_a^c &= 0 \\ i\partial_t b_a^c + \xi_a^{'} b_a^c &= 0, \end{aligned} \tag{5.28}$$

which after some algebra results into equations from Table 5.1.

We benchmark the dynamics evaluated using DTWA and the exact solution for spin, polarized along $-x$ axis, in Fig. 5.2. The exact solution is given by $\sigma^x = \sigma^x(0)e^{-2\kappa t}$. The numerical results agree at all times in this case. Such agreement can be explained when one considers the origin of the dephasing: coupling of the spin to the infinite temperature (T much larger than the typical energy scale of the model) boson bath. At this temperature, all quantum effects are washed out, and spin coherences decay, making the semiclassical picture valid at all times.

[2]Here, we use the method with the single Hubbard-Stratonovich implementation. The resulting dynamics, when averaged over many realizations, remain the same.

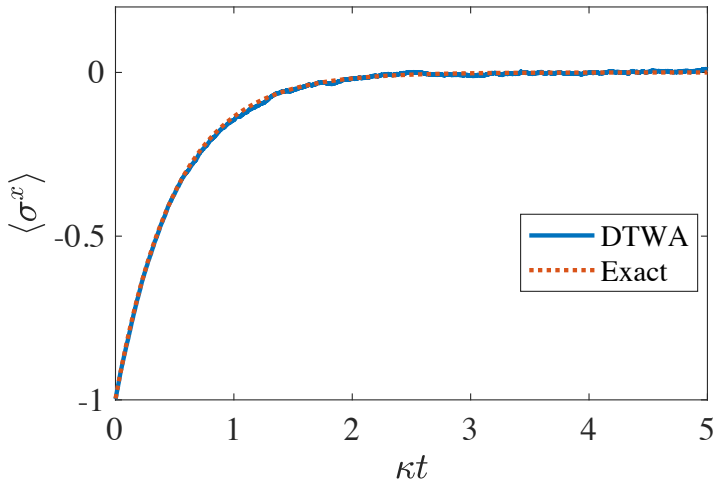

FIGURE 5.2. Dynamics of a single spin, polarized along x direction, under dephasing with the rate κ. The red dotted line is the exact solution, and the blue solid line is the result of the DTWA simulation.

5.4.3. *Collective spin loss*

The dynamics for collective spin loss can be derived similarly to the one for single spin loss, with one extra step. We diagonalize the Lindbladian part, $\Gamma_{nm} = \sum_i V_{mi} D_{ii} V_{in}^{-1}$, introducing N collective decay operators, $O_\nu = \sum_m \sigma_m^- V_{m\nu}$. Then, the dissipative action is given by

$$S_d = \int dt \left[-i \sum_\nu \frac{\Gamma_\nu}{2} \left(2 O_\nu^+ \bar{O}_\nu^- - \bar{O}_\nu^- O_\nu^- - \bar{O}_\nu^+ O_\nu^+ \right) \right], \tag{5.29}$$

and results in the following dynamics for boson fields

$$\begin{aligned} & i\partial_t a_m^c - i\frac{1}{2}\Gamma_\nu \sum_n V_{\nu n}^{-1} \bar{b}_n^c a_n^c b_m^c V_{m\nu} + \frac{1}{2} b_m^c \left(V_{m\nu} \bar{\xi}_\nu^q \right) = 0 \\ & i\partial_t b_m^c + i\frac{1}{2}\Gamma_\nu V_{\nu m}^{-1} a_m^c \sum_n \bar{a}_n^c b_n^c V_{n\nu} + \frac{1}{2} \left(\xi_\nu^q V_{\nu m}^{-1} \right) a_m^c = 0, \end{aligned} \tag{5.30}$$

where, for each $\Gamma_\nu \equiv D_{\nu\nu}$, we have noise HS fields with variance $\left\langle \xi_\nu(t) \bar{\xi}_\mu(t') \right\rangle = 2\Gamma_\nu \delta(t-t') \delta_{\mu\nu}$. Finally, by performing rotations $\xi_m = \sum_\nu \xi_\nu^q V_{\nu m}^{-1}$, the dissipative dynamics of correlated spin decay are given in Table 5.1.

Depending on Γ_{ij}, one can cover different models, starting from spontaneous emission when $\Gamma_{ij} = \gamma \delta_{ij}$ to a Dicke SR [65, 115] when $\Gamma_{ij} = \gamma$. The latter appears when the localized array of atoms radiates in free space with the wavelength λ much exceeding atomic spacing d. In this case, the constructive interference results in the factor N enhancement of the radiated light intensity due to the correlation between atoms. If the spacing between atoms increased to the orders of λ and above, different dissipation

channels (given by diagonalization of Γ_{ij}) interfere destructively, and the atoms dephase, resulting in independent exponential decay when $d \gg \lambda$ [116].

The correlated dissipation attracts a lot of attention these days through its application to superradiant lasers for the generation of ultra-narrow laser lines and the emission of non-Gaussian light from driven arrays [58, 116–118]. For a mesoscopic system with sub-wavelength spacing between emitters, the subradiant modes are commonly considered as a dark state since they show a power low instead of exponential decay and, through their long live timescales, they can be utilized for atomic clocks or some other applications [119]. The non-local dissipation has also been studied in the context of the controlled spread of correlations [120, 121] and realization of dissipative time crystals [122, 123]. Below, we consider an example of a free-space superradiance for a sub-wavelength array.

We consider a cloud of atoms in the lattice, with a single atom occupation of each site. Atomic positions are indicated by vectors $\mathbf{r}_i$ with $i = 1, \ldots, N$. Atoms interact with each other through dipole interaction, resulting in the following Hamiltonian

$$H = \omega_z \sum_i \hat{\sigma}_i^z + \sum_{ij} J_{ij} \hat{\sigma}_i^+ \hat{\sigma}_j^- . \tag{5.31}$$

The radiation of atoms then is given by the Lindblad master equation

$$\dot{\hat{\rho}} = -\frac{i}{\hbar}[\hat{H}, \hat{\rho}] + \sum_{mn} \frac{\Gamma_{mn}}{2} \left(2\hat{\sigma}_m^- \hat{\rho} \hat{\sigma}_n^+ - \{\hat{\sigma}_m^+ \hat{\sigma}_n^-, \hat{\rho}\} \right) . \tag{5.32}$$

The coherent and dissipative parts of interaction read [115, 119]

$$J_{ij} - i\frac{\Gamma_{ij}}{2} = -\frac{\mu_0 \omega_0^2}{\hbar} \wp^* \cdot \mathbf{G}_0 \left(\mathbf{r}_i, \mathbf{r}_j, \omega_0 \right) \cdot \wp \tag{5.33}$$

and depend on the dipole matrix elements $\wp$ for transition with given polarization (a circular one in this case), the propagator of the electromagnetic field $\mathbf{G}_0$, $\omega_0 = 2\pi c/\lambda$ with λ is a wavelength of the emitted light, and the vacuum permeability μ_0. Considering atoms being strongly localized by the trapping potential, we can consider $\mathbf{r}_i$ as the classical variables and substitute the propagator with the classical Green function. We also determine $\mathbf{r}_{ij} = \mathbf{r}_i - \mathbf{r}_j$. The free space dyadic Green function is given by [124, 125]

$$\mathbf{G}_0(\mathbf{r}, \omega) = \frac{e^{ik_0 r}}{4\pi k_0^2 r^3} \left[(k_0^2 r^2 + ik_0 r - 1)\mathbb{1} + (3 - 3ik_0 r - k_0^2 r^2) \frac{\mathbf{r} \otimes \mathbf{r}}{r^2} \right] \tag{5.34}$$

with $r = |\mathbf{r}|$, $k_0 = 2\pi/\lambda$, and momentum $k_0 = \omega_0/c$. The imaginary part gives the collective decay rates, with the diagonal elements corresponding to a free-space decay rate, which is denoted $\Gamma_{ii} \equiv \Gamma_0$, and the real part corresponds to the interaction between emitters. We absorb the diagonal elements J_{ii} to the definition of ω_z.

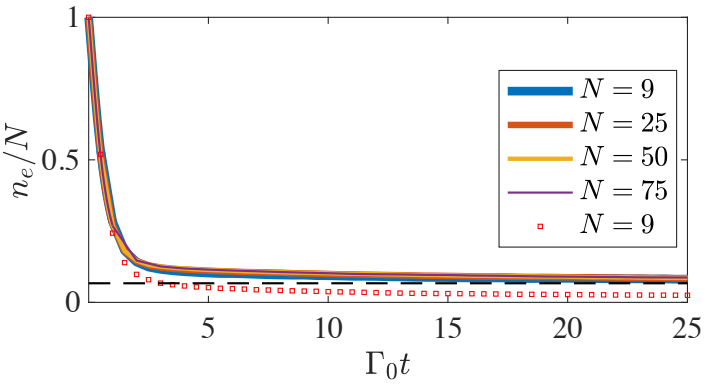

FIGURE 5.3. Normalized population of the excited state in the one-dimensional array of atoms for different system sizes. The red squares indicate the exact solution for $N = 9$, which munches DTWA calculation (blue solid line) at short times. The different line widths are used for better visibility.

When atoms are located close enough, the early time dynamics exhibit fast decay through the superradiant modes, and at later timescales, the dynamics are governed by slow subradiant modes. In this intermediate regime, the excited atomic state keeps populated with the decay rate given by smaller eigenvalues of Γ_{ij}.

We simulate the dynamics of such inverted atomic arrays via the DTWA method. The non-dissipative part of the equations of motion read

$$\begin{aligned}
\partial_t s_k^x &= s_k^z \sum_m J_{km} s_m^y - 2\omega_0 s_k^y \\
\partial_t s_k^y &= -s_k^z \sum_m J_{km} s_m^x + 2\omega_0 s_k^x \\
\partial_t s_k^z &= s_k^y \sum_m J_{km} s_m^x - s^x \sum_m J_{km} s_m^y
\end{aligned} \tag{5.35}$$

and the dissipation-induced contribution is given in Table 5.1.

The example of dynamics for 1d array of atoms separated by $a = \lambda/5$ is shown in Fig. 5.3. Here, we plot the population of the excited atomic state

$$n_e = \frac{N + \sum_i \sigma_i^z}{2} \tag{5.36}$$

as a function of time. At early times, $t < 1/\Gamma_0$, the DTWA calculations and exact solution of the master equation coincide, similarly to what we have seen for a single spin loss in Fig. 5.1. Then, DTWA predicts slow relaxation of the σ^z (and, respectively, n_e) towards the wrong steady state, given by $\sigma^z \to -\sqrt{3}/2$ (with $\sigma^{z2} \to 4/3$ instead of 1). The result is consistent for different system sizes and system dimensions. A similar mismatch has been observed in Ref. [126] for the continuous-discrete TWA method,

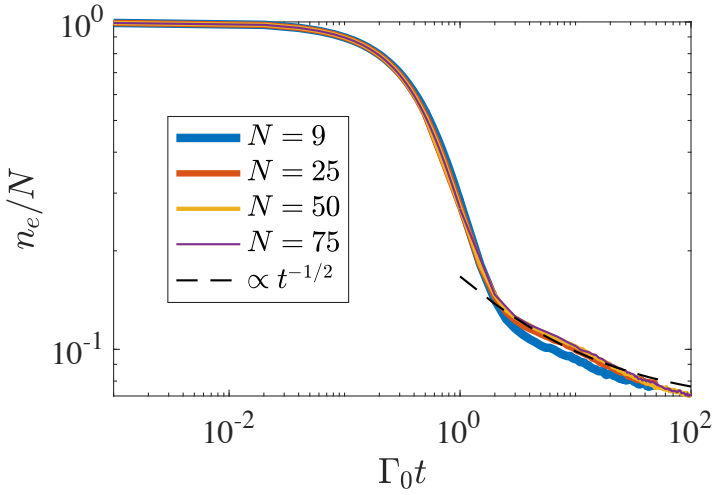

FIGURE 5.4. The same as in Fig. 5.3 but in logarithmic scale. The late time behavior follows $1/\sqrt{t}$ dependence, black dashed line.

highlighting the limitation of the semiclassical description to correlated dissipation: higher order corrections are needed to obtain correct late-time dynamics.

Nevertheless, the semiclassical dynamics can still be utilized for capturing slow sub-radiant modes. For instance, Fig. 5.4 shows that at a late time, one can recover a power-low decay (instead of exponential), although the absolute value of n_e is shifted by approximately 0.067 due to the renormalization of the Bloch sphere radius. What is also important is when one accounts for a shift in n_e, the dynamics follow $1/\sqrt{t}$ decay (cf. black dashed line in the Figure), predicted theoretically in a single-excitation sector [119].

5.4.4. *Resonance fluorescence Driven spin array*

We add the Rabi driving, described by the Hamiltonian

$$\hat{H}_d = \Omega \sum_n \hat{\sigma}_n^x, \tag{5.37}$$

and study correlated emission of the driven atomic array. The competition of the dissipation and coherent drive results in the evolution of the atomic population towards non-zero value in the steady state. However, due to the presence of the inter-atomic interaction J_{ij}, we do not have the analytical expression for finale n_e.

Fig. 5.5 compares dynamics of the normalized population of the excited state for different driving strengths Ω (solid lines) with the exact dynamics (dashed lines) for $N = 8$ atoms[3]. At small driving frequencies, $\Omega < \Gamma_0$, the late-time DTWA dynamics

[3]The number of atoms N is chosen low due to the memory limitations needed for the exact solution.

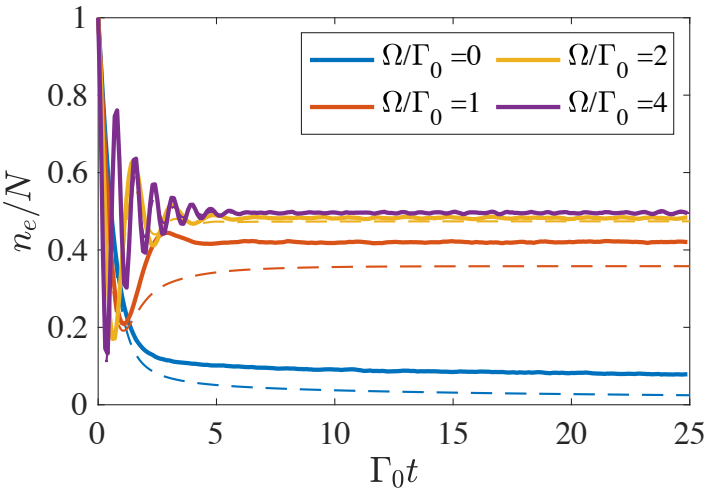

FIGURE 5.5. Dynamics of the excitation number of $N = 8$ spins prepared in the spin-up state under correlated decay. The system is subjected to an external Rabi drive with frequency Ω. The dotted lines are exact solutions, and the solid lines are the results of the DTWA simulations.

deviate from the exact solution due to the build-up of correlations and failure of the semiclassical method. However, if the drive is stronger, the Rabi part governs the dynamics, preventing the development of strong correlations, and the convergence with the exact solution becomes better. For $\Omega = 4\Gamma_0$, we even approach the correct steady state.

The important message here is that the method works better for strongly driven systems, $\Omega \gg \Gamma_0$. The driving field, in this case, prevents the development of strong correlations in the system, prolonging the validity of the semiclassical description.

As we have illustrated above, the developed semiclassical method allows for the accounting of correlations in the driven-dissipative spin models. The method is suitable for evaluating the dynamics of spin synchronizations, particularly boundary time crystals [123] and fluorescence of driven atomic arrays [127]. Access to the two-point correlation functions allows for exploring metrology-relevant spin squeezing at early time dynamics, as has been done for atomic clocks [128]. Another implementation is to study an array of driven Rydberg atoms in the presence of single-body loss and dephasing [104, 129]. The method is capable of capturing early dynamics as well as reaching the correct steady state if the driving (or dephasing) is sufficient.

5.5. Extension to a non-Markovian regime

Another direction for the systematical study of the phase transition is to revisit the origin of dissipation and explore the memory effect on the phase transitions. While for most cases of the phase transitions, encountering dissipations through the Lindblad master equation is sufficient, close to the criticality, such approximation can result in qualitative and quantitative changes (here, the effective Plank constant is given by $1/N$). The memory effects also become important when the source of dissipation is not the fluctuations of the electromagnetic field but, for instance, the magnetic field generated by the substrate material [130–132].

The non-Markovian semi-classical dynamics can be derived with the Keldysh path integral as well. Consider a system-bath Hamiltonian (2.3) with weak[4] linear coupling between the system and environment (2.4). On the Keldysh contour, the free part of the bath action reads

$$S_0 = \int dt \sum_{k,s} s \left(\bar{f}_k^s i\partial_t f_k^s - \omega_k \bar{f}_k^s f_k^s \right), \tag{5.38}$$

where we use the canonical part for coherent boson fields and the interaction

$$S_{int} = \int dt \left(- \sum_{k,i} \left[H_{ik}^+ - H_{ik}^- \right] \right) \tag{5.39}$$

with $H_{ik}^s = g_{ik} \left(\bar{f}_k^s O_i^s + \bar{O}_i^s f_k^s \right) + \eta_{ik} \left(\bar{f}_k^s \bar{O}_i^s + O_i^s f_k^s \right)$ and $s = \pm$. After Keldysh rotation to the classical-quantum basis, the action reads

$$S_0 = \int d\omega \sum_k \bar{F}_k G_k^{-1} F_k \tag{5.40}$$

with with $F_k = (f_k^c, f_k^q)^T$ and

$$G_k^{-1} = \begin{pmatrix} 0 & G_A^{-1}(\omega) \\ G_R^{-1}(\omega) & G_K^{-1}(\omega) \end{pmatrix} \tag{5.41}$$

and the time and frequency representation are connected via the Fourier transform. The system-bath interaction can be written in the form

$$S_{int} = \int dt \sum_{k,i} \left(- \left[\bar{F}_k O_k + \bar{O}_k F_k \right] \right) \tag{5.42}$$

where we consider $\bar{O} = \left(g_{ik} \bar{O}_i^q + \eta_{ik} O_i^q, g_{ik} \bar{O}_i^c + \eta_{ik} O_i^c \right)$. For a moment, we set $\eta_{ik} = 0$. After integrating out the baths degrees of freedom, the effective action for the system

[4]For quadratic bath Hamiltonian the strength of the coupling, is principle, is not crucial, however we maintain it low to assume factorizability of the system-bath density matrices.

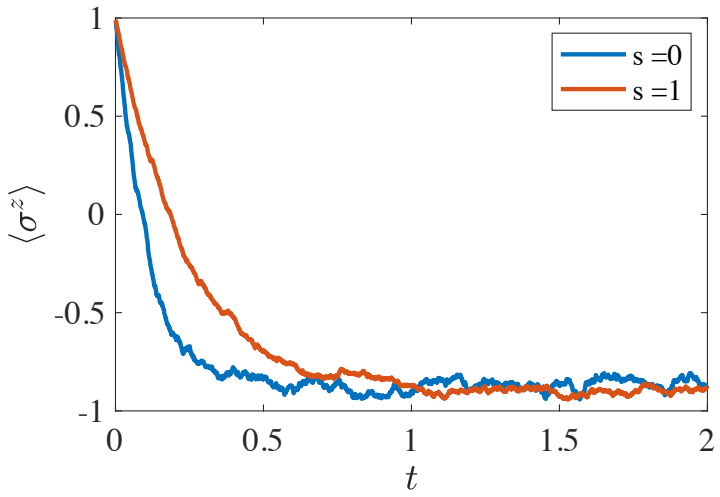

FIGURE 5.6. Example of single spin loss dynamics for flat and Ohmic environments.

reads

$$S_{eff} = \int dtdt' \left[-\sum_i \bar{O}_i(t) \mathcal{D}_{ij}(t-t') \sum_j O_j(t') \right] \tag{5.43}$$

where $\bar{O}_i = \left(\bar{O}_i^q, \bar{O}_i^c\right)$ and $\mathcal{D}_{ij}(t-t') = \sum_s g_{s,i} g_{s,j} G_s(t-t')$. Note that here we extracted couplings g_{ki} from the definition of O.

If the bath is in the thermal equilibrium, all Green's functions can be expressed via spectral density of the bath [64]

$$J^{ij}(\omega) = \pi \sum_k g_k^i g_k^j \delta(\omega - \omega_k) = \frac{2\gamma_{ij}}{\pi} \left(\frac{\omega}{\omega_z}\right)^s e^{-\frac{\omega}{\omega_c}}. \tag{5.44}$$

Here, $s \leq 1$, ω_c is the cutoff frequency, which should be much larger than the rest of the energy scales in the model, ω_z is the spin level splitting, and γ_{ij} is the coupling (or dissipation) strength. The corresponding expressions for Green's functions are

$$D_{ij}^K(\omega) = -2iJ_{ij}(\omega) \coth(\beta\omega/2) \tag{5.45}$$

and

$$D_{ij}^R(\omega) = \left(G_{ij}^A\right)^\dagger = -\frac{1}{2\pi} \int_{-\infty}^{+\infty} d\omega' \frac{J_{ij}(\omega')}{\omega' - \omega - i\eta}. \tag{5.46}$$

The action S_{eff} when keeping terms at most quadratic in quantum fields can be rewritten as

$$S_{eff} = \int dtdt' \left(-\bar{O}^q D^R O^c - \bar{O}^c D^A O^q + \bar{\xi} O^q + \bar{O}^q \xi\right) \tag{5.47}$$

where noise ξ is correlated according to

$$\langle \xi(t) \bar{\xi}(t') \rangle = D_K(t-t'). \tag{5.48}$$

For the case of a single spin coupled to the bath, and $\hat{O} = \hat{a}^\dagger \hat{b}$, the spin dynamics reads

$$\begin{aligned}
\partial_t \sigma^- &= \frac{i}{2}\sigma^z(t) \int dt' D^R(t-t')\sigma^-(t') - i\sigma^z(t)\xi(t) \\
\partial_t \sigma^z &= \left(i\sigma^-(t) \int dt' \left(D^R(t-t')\right)^\dagger \sigma^+(t') - i\sigma^+(t) \int dt' D^R(t-t')\sigma^-(t') \right) \\
&\quad + 2i\left(\sigma^+(t)\xi(t) - \sigma^-(t)\bar{\xi}(t)\right)
\end{aligned} \tag{5.49}$$

For a flat spectrum $D^R(t-t') \propto \delta(t-t')$ and one gets Markovian dynamics, identical to one given by Lindblad master equation. By adding structure to the environment and making bath spectral density vary with ω, the dynamics start to deviate from the flat case, cf.Fig. 5.6. Here, even though at late times, magnetization relaxes towards the same steady state, in the case of the Ohmic bath, relaxation appears slower. Given this, one can conclude that the structural bath may be efficient for preserving information in the system on longer timescales and, thus, may be more useful for all quantum information applications.

The method allows the evaluation of semi-classical dynamics of spin for structured environments. One can explore the role of the bath spectral density on the relaxation dynamics and also explore the time hierarchy by considering the dynamics of the system on the timescales comparable to the correlation time of the bath τ_B. By increasing τ_B, one can study the fate of the phase transition for different environments.

CHAPTER 6

Conclusions and Future Directions

In this thesis, we present results on non-equilibrium aspects of dissipative phase transitions in the collective models. We show how the interplay of different symmetries or involving various degrees of freedom results in peculiar phases, stationary and non-stationary, which may be realized in state-of-the-art experiments. Exploring such models is one of the crucial tasks nowadays to consider the dissipations not like a destructive agent but as a tool for harnessing complicated non-equilibrium dynamics.

We demonstrated that the dissipative pumping of the system in [1] can drive the system into the non-stationary 'lasing' phase with the persistent spin oscillations, and dissipation in the form of the photon loss stabilizes the system and make it oscillate with the certain polariton frequency (which can be tuned by changing photon-matter coupling). In Ref. [2], we have shown that the cavity losses in the cavity QED platform allow the system to dissipate the excess of energy and relax towards the steady state with the tunable spin-momentum entanglement. In this platform, there is a parameter regime in which the decay of the cavity field does not significantly alter the entanglement, while photons that leave the cavity may be detected through heterodyne detection and give information about the collective system. In particular, the dynamics of the cavity field in different polarizations can be considered a proxy of the entanglement dynamics.

We also developed a method for the inclusion of the semi-classical corrections to the dynamics. The method provides a simple protocol with clear physical meaning and works well in the presence of a drive. While for collective models, the classical description gives valid results in the thermodynamic limit, many quantum simulators with short-range interaction, or collective decay, display a build-up of correlations, which should be taken into account. The method allows to efficiently explore dynamical properties of dissipative spin models in different phases or regimes.

Importantly, the method can be extended to non-Markovian environments, which is of particular relevance for solid-state platforms, such as NV centers in diamonds, which usually interact with the structural electromagnetic environments [130]. The non-Markovian (memory) aspects are important from the perspective of more efficient preservation of information in different spin systems and more accurate evaluation of dynamics of quantum simulators [133–135].

Quantum simulators are a unique platform to explore emergent phenomena and phase transitions. They allow the creation of an analog of a desired physical system and probing its properties in a way that is usually inaccessible in real nature due to limited accessible energy scales, robustness of parameters, etc. The target model can be imprinted via different degrees of freedom, such as spin and momentum of atoms in cavity QED, spin or particles position in trapped ions, etc. Such tunability allows studying various models with continuous or discrete symmetries and short- or long-range interaction. The possible implementations include simulating many different phenomena, including superconductivity [136–138], replica symmetry breaking and quantum spin glass [86, 139], false vacuum decay [140, 141] and string breaking [142]. One could also study the effect of the interaction range on the dynamical properties, such as prethermalization [143, 144]. A competition between different ranges of interactions can be studied via dipolar condensates [37], atoms in a cavity with the optical dressing of interactions [145], etc. A relatively new direction is to adopt quantum statistics and use gas of fermions embedded in the cavity as experimental platform [146–151]. A particular benefit of this approach is a possible implementation of the Sachdev-Ye-Kitaev model [152], which is a core of importance for the investigation of high-temperature superconductivity.

One could also consider some practical applications by driving systems into correlated states and using them for metrology. Because, as we discussed, the effective model can be constructed from different degrees of freedom, such spin-squeezed states may be used for sensing different physical observables. A standard procedure here is to simulate a squeezing-generating Hamiltonian, such as one- or two-axis twisting Hamiltonians, and generate a spin variance in one direction lower than standard quantum limit [153, 154]; Another approach can be dissipation engineering of a dark squeezed state [55, 155]. Here, one can explore non-local dissipation (also generated by a non-Markovian environment) to establish an optimal protocol for the preparation of correlated states.

APPENDIX A

Discrete Truncated Wigner Approximation

Here, we give a short summary of the (Discrete) Truncated Wigner Approximation method; see Refs. [104–106, 108] for comprehensive discussion.

According to the TWA method, quantum operators are mapped to the classical phase space variables. The evolution of the phase space variables is evaluated classically, while quantum fluctuations are encoded in the random distribution of the initial conditions. Then, observables are evaluated by weighted averaging appropriate phase space variables over noise realizations. Precisely, a manifestation of quantum uncertainty in the Hilbert space is replaced with the statistical average in the phase space.

By introducing a continuous phase-point operator, which in coordinate-momentum representation reads

$$\hat{A}(\mathbf{q},\mathbf{p}) = \int \mathrm{d}\xi \, |\mathbf{q}-\xi/2\rangle \, \langle \mathbf{q}+\xi/2| \, e^{-i\mathbf{p}\xi/\hbar}, \tag{A.1}$$

the density matrix could be simulated in the phase space via Wigner quasi-probability distribution, which is the Weyl symbol of the density matrix, $W(\mathbf{p},\mathbf{q}) = \mathrm{Tr}[\hat{\rho}\hat{A}(\mathbf{p},\mathbf{q})]$, or

$$\hat{\rho} = \int \mathrm{d}\mathbf{p}\mathrm{d}\mathbf{q} \; W(\mathbf{q},\mathbf{p})\hat{A}(\mathbf{q},\mathbf{p}). \tag{A.2}$$

Similarly, each operator in the Hilbert space has in correspondence phase-space function, which is called a Weyl symbol of this operator and is defined according

$$O(\mathbf{q},\mathbf{p}) = \int \mathrm{d}\xi \left\langle \mathbf{q}+\frac{\xi}{2}\right| \hat{O}(\hat{\mathbf{q}},\hat{\mathbf{p}}) \left|\mathbf{q}-\frac{\xi}{2}\right\rangle e^{-i\mathbf{p}\xi/\hbar} \tag{A.3}$$

Then, observables can be evaluated with the averaged over the phase space, weighted with the Wigner distribution

$$\langle \hat{O}(\hat{\mathbf{q}},\hat{\mathbf{p}})\rangle = \int \mathrm{d}\mathbf{p}\mathrm{d}\mathbf{q} \; W(\mathbf{q},\mathbf{p})O(\mathbf{q},\mathbf{p}) \tag{A.4}$$

Assuming that $W_t(\mathbf{q},\mathbf{p}) = W_{t=0}(\mathbf{q},\mathbf{p})$, in the lowest order in $\hbar$, such observables can be evaluated as statistical average of $O(\mathbf{q},\mathbf{p})$ over different realization of classical dynamics, initial conditions for which are sampled according to $W_0(\mathbf{q},\mathbf{p})$.

Numerically, truncated Wigner approximation is implemented in the following way:

- Determine Wigner quasi-probability distribution. Conveniently, one starts from the large N coherent states, for which W is the Gaussian distribution [102, 109].
- For each $O(\mathbf{q}, \mathbf{p})$ sample n_{trj} initial conditions.
- For each initial condition, evaluate dynamics according to mean-field equations of motion.
- Evaluate observables at each time moment as a statistical average over n_{trj} realizations of dynamics.

When the Hilbert space is finite, a similar procedure has been introduced [107], where mapping to the phase space is done via *discrete* phase-space operators

$$\hat{A} = \frac{1}{4}\left(\hat{1}_2 + \boldsymbol{s}_{\boldsymbol{\alpha}}\hat{\boldsymbol{\sigma}} + \hat{1}_2 + \boldsymbol{s}_{\boldsymbol{\alpha}'}\hat{\boldsymbol{\sigma}}\right) \tag{A.5}$$

with $\boldsymbol{s}_{\boldsymbol{\alpha}} = \{(1,1,-1),(-1,-1,-1)\}$ and $\boldsymbol{s}_{\boldsymbol{\alpha}'} = \{(1,-1,-1),(-1,1,-1)\}$. This particular choice of $\boldsymbol{s}_{\boldsymbol{\alpha}',\boldsymbol{\alpha}}$ corresponds to the coherent state when all spins are polarized along negative z direction. The discrete Wigner function is given by $W = \frac{1}{2}\,\mathrm{Tr}\left[\hat{A}\hat{\rho}\right]$.

Since the phase-space operator is linear in spin, the dynamics of classical spins $\boldsymbol{s}(t)$ contains sufficient information to recover semi-classical dynamics [104]. Thus, one can consider the dynamics of such N classical spins according

$$\dot{s}^{\mu}(t) = \{s^{\mu}, \mathcal{H}_0\}_P\,, \tag{A.6}$$

where $\mathcal{H}_0$ is the Weyl symbol of the Hamiltonian and $\{,\}_P$ is the Poisson bracket [104].

Supposing that phase space operators are factorizable during the course of the dynamics and considering only initial states where all spins are uncorrelated, we end up with the factorized Wigner function

$$W(\mathbf{S}) = \otimes_{i=1}^{N} W(\mathbf{s}_i) \tag{A.7}$$

and for the particular initial state when all spins are pointed towards the south pole of the Bloch sphere, it reads

$$\begin{aligned} W(\mathbf{s}_i) =& \frac{1}{4}\delta(s_i^z+1)\left[\delta(s_i^x+1)+\delta(s_i^x-1)\right] \\ &\times\left[\delta(s_i^y+1)+\delta(s_i^y-1)\right]. \end{aligned} \tag{A.8}$$

It corresponds to the discrete sampling of the initial states when $s_j^z = -1$ and transverse components $s_j^{x,y} = \pm 1$ with equal probability. Note that for each spin $\boldsymbol{s}_j$, sampling is done separately.

After evaluation dynamics for $\boldsymbol{s}(t)$ according to classical equations of motion for n_{trj} different initial conditions, observables are given as the average over different realizations,

$$\begin{aligned}\langle\hat{\sigma}_i^{\alpha}(t)\rangle &= \frac{1}{n_{trj}}\sum_{j=1}^{n_{trj}} s_{i,j}^{\alpha}(t)\\ \langle\{\hat{\sigma}_i^{\alpha}(t)\hat{\sigma}_k^{\beta}(t)\}_s\rangle &= \frac{1}{n_{trj}}\sum_{j=1}^{n_{trj}} s_{i,j}^{\alpha}(t)s_{k,j}^{\beta}(t).\end{aligned} \tag{A.9}$$

Here $\alpha,\beta \in \{x,y,z\}$; and $i,k \in 1,..,N$ are positions of two spins. (D)TWA gives access to the symmetrized few-point correlation functions. The method is effective for calculating two-point functions if proper initial sampling is introduced, see discussion in Refs. [104, 108]. The method is able to capture dynamics beyond the semi-classics if it is combined with the BBGKY hierarchy of equations for few-point correlation functions [111]. In this case, dynamics for later times can be accessed.

Acknowledgements

First of all, I want to thank my supervisor, Jamir Marino, for all the knowledge, wisdom, and support I received during my studies.

I want to thank Shane P. Kelly for our numerous discussions on the solitons and life. I thank Allesio Lerose and Shu Zhang for our collaboration on the spintronics project. I thank Kushal Seetharam for sharing his broad experience and making me look at writing differently. I also thank Rodrigo Rosa-Medina, Nicola Reiter, and Fabian Finger for making atoms tangible. Special thanks to Hossein Hosseinabadi for our multiple chats on Keldysh.

I also thank the senior collaborators Giovanna Morigi, Yaroslav Tservonyak, Iacoppo Carusotto, Tobias Donner, and Ferdinand Schmidt-Kaler for providing a broad perspective and an immense source of inspiration and motivation.

I thank other former and present NEUQUAM group members, particularly Martino Stefanini, Aleksandra Ziolkowska, Riccardo J. Valencia-Tortora, and Mark Oehlgrien, for the fruitful discussions and support over the years. I also thank my Ukrainian friends from 111/2, with whom I could safely share all my Ph.D.-related and personal struggles.

I thank my family for supporting my interest in physics at school and accepting my decision later on.

Curriculum Vitae

Personal Information

Name	Oksana Chelpanova
Birth	30.03.1996, Radensk, Kherson Region, Ukraine
Nationality	Ukraine
Address	Wallstr. 33, 55122 Mainz, Germany

Education

Since 07/2020	Institut für Physik, Johannes Gutenberg Universität Mainz, Germany, thesis "Dissipative phases in open quantum systems", supervisor J-Prof. Dr. J. Marino
09/2018–06/2020	**M. S.**, Department of Physics, Taras Shevchenko National University of Kyiv, Ukraine, master thesis "Dissipative dynamics of topological structures in the non-linear medium with gain and loss," supervisor Dr. O. I. Yakimenko
09/2014–06/2018	**B. S.**, Department of Physics, Taras Shevchenko National University of Kyiv, Ukraine, bachelor thesis "Spatio-temporal vortex rings in the atomic Bose-Einstein condensates," supervisor Dr. O. I. Yakimenko
09/2011–05/20014	Kherson Physical and Technical Lyceum
09/2006–05/2011	Radensk secondary school
09/2003–05/206	Radensk primary school

Academic Career

Since 08/2020	Research assistant at Johannes Gutenberg Universität Mainz, in the group of J-Prof. Dr. Jamir Marino
Since 10/2022	Teaching assistant at the Johannes Gutenberg Universität Mainz

Bibliography

[1] O. Chelpanova et al. “Intertwining of lasing and superradiance under spintronic pumping”. In: *Phys. Rev. B* 108 (10 2023), p. 104302.

[2] O. Chelpanova et al. “Dynamics of spin-momentum entanglement from superradiant phase transitions”. In: *Phys. Rev. Res.* 6 (3 2024), p. 033193.

[3] O. Chelpanova et al. “Injection and nucleation of topological defects in the quench dynamics of the Frenkel-Kontorova model”. In: *Europhysics Letters* 143.2 (2023), p. 25002.

[4] O. Chelpanova et al. “Dynamics of quantum discommensurations in the Frenkel-Kontorova chain”. In: *Phys. Rev. B* 109 (21 2024), p. 214107.

[5] G. Jaeger. “The Ehrenfest classification of phase transitions: introduction and evolution”. In: *Archive for history of exact sciences* 53 (1998), pp. 51–81.

[6] P. im ueblichen und erweiterten Sinn. “classifiziert nach den entsprechenden Singularitaeten des thermodynamischen Potentiales”. In: *Proc. Amsterdam Akad* 36 (1933), pp. 153–157.

[7] L. D. Landau et al. “On the theory of phase transitions”. In: *Zh. eksp. teor. Fiz* 7.19-32 (1937), p. 926.

[8] N. Goldenfeld. *Lectures on phase transitions and the renormalization group*. CRC Press, 2018.

[9] J. Cardy. *Scaling and renormalization in statistical physics*. Vol. 5. Cambridge university press, 1996.

[10] K. G. Wilson. “Renormalization group and critical phenomena. I. Renormalization group and the Kadanoff scaling picture”. In: *Physical review B* 4.9 (1971), p. 3174.

[11] L. P. Kadanoff and A. Houghton. “Numerical evaluations of the critical properties of the two-dimensional Ising model”. In: *Physical Review B* 11.1 (1975), p. 377.

[12] L. P. Kadanoff. “Scaling laws for Ising models near T c”. In: *Physics Physique Fizika* 2.6 (1966), p. 263.

[13] K. G. Wilson and M. E. Fisher. “Critical exponents in 3.99 dimensions”. In: *Physical Review Letters* 28.4 (1972), p. 240.

[14] M. E. Fisher. “The theory of equilibrium critical phenomena”. In: *Reports on progress in physics* 30.2 (1967), p. 615.

[15] S. Sachdev. “Quantum phase transitions”. In: *Physics world* 12.4 (1999), p. 33.

[16] M. Greiner et al. “Quantum phase transition from a superfluid to a Mott insulator in a gas of ultracold atoms”. In: *nature* 415.6867 (2002), pp. 39–44.

[17] J. Kasprzak et al. “Bose–Einstein condensation of exciton polaritons”. In: *Nature* 443.7110 (2006), pp. 409–414.

[18] Y. Kawaguchi and M. Ueda. “Spinor bose–einstein condensates”. In: *Physics Reports* 520.5 (2012), pp. 253–381.

[19] M. Lu et al. “Strongly dipolar Bose-Einstein condensate of dysprosium”. In: *Physical review letters* 107.19 (2011), p. 190401.

[20] R. Heidemann et al. “Evidence for coherent collective Rydberg excitation in the strong blockade regime”. In: *Physical Review Letters* 99.16 (2007), p. 163601.

[21] B Olmos, R González-Férez, and I Lesanovsky. “Collective Rydberg excitations of an atomic gas confined in a ring lattice”. In: *Physical Review AAtomic, Molecular, and Optical Physics* 79.4 (2009), p. 043419.

[22] P. Schauß et al. “Observation of spatially ordered structures in a two-dimensional Rydberg gas”. In: *Nature* 491.7422 (2012), pp. 87–91.

[23] J. Zeiher et al. “Coherent many-body spin dynamics in a long-range interacting Ising chain”. In: *Physical review X* 7.4 (2017), p. 041063.

[24] H. Bernien et al. “Probing many-body dynamics on a 51-atom quantum simulator”. In: *Nature* 551.7682 (2017), pp. 579–584.

[25] H. Labuhn et al. “Tunable two-dimensional arrays of single Rydberg atoms for realizing quantum Ising models”. In: *Nature* 534.7609 (2016), pp. 667–670.

[26] C. Monroe et al. “Programmable quantum simulations of spin systems with trapped ions”. In: *Reviews of Modern Physics* 93.2 (2021), p. 025001.

[27] D. A. Gangloff, A. Bylinskii, and V. Vuletić. “Kinks and nanofriction: Structural phases in few-atom chains”. In: *Physical Review Research* 2.1 (2020), p. 013380.

[28] D. Porras and J. I. Cirac. “Effective quantum spin systems with trapped ions”. In: *Physical review letters* 92.20 (2004), p. 207901.

[29] A. Blais et al. “Circuit quantum electrodynamics”. In: *Reviews of Modern Physics* 93.2 (2021), p. 025005.

[30] F. Mivehvar et al. “Cavity QED with quantum gases: new paradigms in many-body physics”. In: *Advances in Physics* 70.1 (2021), pp. 1–153. eprint: https://doi.org/10.1080/00018732.2021.1969727.

[31] F. Brennecke et al. “Cavity QED with a Bose–Einstein condensate”. In: *nature* 450.7167 (2007), pp. 268–271.

[32] P. Lodahl et al. “Chiral quantum optics”. In: *Nature* 541.7638 (2017), pp. 473–480.

[33] K. Baumann et al. “Dicke quantum phase transition with a superfluid gas in an optical cavity”. In: *nature* 464.7293 (2010), pp. 1301–1306.

[34] K. Sacha and J. Zakrzewski. “Time crystals: a review”. In: *Reports on Progress in Physics* 81.1 (2017), p. 016401.

[35] M. P. Zaletel et al. “Colloquium: Quantum and classical discrete time crystals”. In: *Reviews of Modern Physics* 95.3 (2023), p. 031001.

[36] P. Kongkhambut et al. “Observation of a continuous time crystal”. In: *Science* 377.6606 (2022), pp. 670–673.

[37] A. Recati and S. Stringari. “Supersolidity in ultra-cold dipolar gases”. In: (2024).

[38] A. Baksic and C. Ciuti. “Controlling Discrete and Continuous Symmetries in "Superradiant" Phase Transitions with Circuit QED Systems”. In: (2014).

[39] F. Mivehvar et al. “Driven-Dissipative Supersolid in a Ring Cavity”. In: ().

[40] S. C. Schuster et al. “Supersolid properties of a Bose-Einstein condensate in a ring resonator”. In: ().

[41] T. Bland et al. “Two-Dimensional Supersolid Formation in Dipolar Condensates”. In: *Phys. Rev. Lett.* 128 (19 2022), p. 195302.

[42] Y. Deng and S. Yi. “Self-ordered supersolid phase beyond Dicke superradiance in a ring cavity”. In: *Phys. Rev. Res.* 5 (1 Jan. 2023), p. 13002.

[43] P. Shakya, A. Ratnakar, and S. Ghosh. “Dimensional cross-over in self-organised super-radiant phases of ultra-cold atoms inside a cavity”. In: *Journal of Physics B: Atomic, Molecular and Optical Physics* 56 (3 Feb. 2023).

[44] J. Léonard et al. “Supersolid formation in a quantum gas breaking a continuous translational symmetry”. In: *Nature* 543 (7643 Mar. 2017), pp. 87–90.

[45] A. Morales et al. *Coupling two order parameters in a quantum gas*. Aug. 2018.

[46] D. Walls and G. J. Milburn. “Quantum Information”. In: *Quantum Optics*. Springer, 2008, pp. 307–346.

[47] H.-P. Breuer and F. Petruccione. *The Theory of Open Quantum Systems*. Oxford University Press, Jan. 2007.

[48] L. M. Sieberer et al. “Dynamical critical phenomena in driven-dissipative systems”. In: *Physical review letters* 110.19 (2013), p. 195301.

[49] J. Marino and S. Diehl. “Driven markovian quantum criticality”. In: *Physical review letters* 116.7 (2016), p. 070407.

[50] L. M. Sieberer et al. “Universality in driven open quantum matter”. In: *arXiv preprint arXiv:2312.03073* (2023).

[51] J. Marino. “Universality Class of Ising Critical States with Long-Range Losses”. In: *Phys. Rev. Lett.* 129 (5 2022), p. 050603.

[52] R. Lin et al. “Dissipation-Engineered Family of Nearly Dark States in Many-Body Cavity-Atom Systems”. In: *Phys. Rev. Lett.* 128 (15 2022), p. 153601.

[53] J. Skulte et al. “Condensate Formation in a Dark State of a Driven Atom-Cavity System”. In: *Phys. Rev. Lett.* 130 (16 2023), p. 163603.

[54] A. Piñeiro Orioli, J. K. Thompson, and A. M. Rey. "Emergent Dark States from Superradiant Dynamics in Multilevel Atoms in a Cavity". In: *Phys. Rev. X* 12 (1 2022), p. 011054.

[55] B. Sundar et al. "Squeezing multilevel atoms in dark states via cavity superradiance". In: *arXiv preprint arXiv:2302.10828* (2023).

[56] J. T. Young et al. "Nonequilibrium fixed points of coupled Ising models". In: *Physical Review X* 10.1 (2020), p. 011039.

[57] F. Minganti et al. "Spectral theory of Liouvillians for dissipative phase transitions". In: *Physical Review A* 98.4 (2018), p. 042118.

[58] J. G. Bohnet et al. "A steady-state superradiant laser with less than one intracavity photon". In: *Nature* 484.7392 (2012), pp. 78–81.

[59] M. A. Norcia et al. "Cavity–mediated collective spin–exchange interactions in a strontium superradiant laser". In: *Science* 361.6399 (2018), pp. 259–262.

[60] F. Brennecke et al. "Real-time observation of fluctuations at the driven-dissipative Dicke phase transition". In: *Proceedings of the National Academy of Sciences* 110.29 (2013), pp. 11763–11767. eprint: https://www.pnas.org/doi/pdf/10.1073/pnas.1306993110.

[61] C. W. Gardiner. *Handbook of stochastic methods for physics, chemistry and the natural sciences*. Third. Vol. 13. Springer Series in Synergetics. Berlin: Springer-Verlag, 2004, pp. xviii+415.

[62] A. J. Daley. "Quantum trajectories and open many-body quantum systems". In: *Advances in Physics* 63.2 (2014), pp. 77–149.

[63] M. Stefanini and J. Marino. "Orthogonality catastrophe beyond bosonization from post-selection". In: *Phys. Rev. Res.* 6 (4 2024), p. L042022.

[64] A. Altland and B. D. Simons. *Condensed Matter Field Theory*. 2nd ed. Cambridge University Press, 2010.

[65] R. H. Dicke. "Coherence in spontaneous radiation processes". In: *Phys. Rev.* 93.1 (1954), p. 99.

[66] K. Hepp and E. H. Lieb. "Equilibrium Statistical Mechanics of Matter Interacting with the Quantized Radiation Field". In: *Phys. Rev. A* 8 (5 1973), pp. 2517–2525.

[67] K. Hepp and E. H. Lieb. "On the superradiant phase transition for molecules in a quantized radiation field: the dicke maser model". In: *Annals of Physics* 76.2 (1973), pp. 360–404.

[68] J. Keeling, M. J. Bhaseen, and B. D. Simons. "Collective dynamics of Bose–Einstein condensates in optical cavities". In: *Phys. Rev. Lett.* 105.4 (2010), p. 043001.

[69] J. Keeling, M. J. Bhaseen, and B. D. Simons. "Collective Dynamics of Bose-Einstein Condensates in Optical Cavities". In: *Phys. Rev. Lett.* 105 (4 2010), p. 043001.

[70] P. Kirton and J. Keeling. "Superradiant and lasing states in driven-dissipative Dicke models". In: *New Journal of Physics* 20.1 (2018), p. 015009.

[71] P. Kirton et al. "Introduction to the Dicke model: From equilibrium to nonequilibrium, and vice versa". In: *Advanced Quantum Technologies* 2.1-2 (2019), p. 1800043.

[72] N. Dogra et al. "Dissipation-induced structural instability and chiral dynamics in a quantum gas". In: *Science* 366.6472 (2019), pp. 1496–1499.

[73] D. Dreon et al. "Self-oscillating pump in a topological dissipative atom–cavity system". In: *Nature* 608.7923 (2022), pp. 494–498.

[74] P. Kirton and J. Keeling. "Suppressing and restoring the Dicke superradiance transition by dephasing and decay". In: *Phys. Rev. Lett.* 118.12 (2017), p. 123602.

[75] S. Haroche and J.-M. Raimond. *Exploring the quantum: atoms, cavities, and photons*. Oxford university press, 2006.

[76] H. Ritsch et al. "Cold atoms in cavity–generated dynamical optical potentials". In: *Rev. Mod. Phys.* 85.2 (2013), p. 553.

[77] E. M. Purcell, H. C. Torrey, and R. V. Pound. "Resonance absorption by nuclear magnetic moments in a solid". In: *Physical review* 69.1-2 (1946), p. 37.

[78] H. Walther et al. "Cavity quantum electrodynamics". In: *Reports on Progress in Physics* 69.5 (2006), p. 1325.

[79] K. B. Davis et al. "Bose-Einstein condensation in a gas of sodium atoms". In: *Physical review letters* 75.22 (1995), p. 3969.

[80] M. H. Anderson et al. "Observation of Bose-Einstein condensation in a dilute atomic vapor". In: *science* 269.5221 (1995), pp. 198–201.

[81] F. Ferri et al. "Emerging Dissipative Phases in a Superradiant Quantum Gas with Tunable Decay". In: *Phys. Rev. X* 11 (4 2021), p. 041046.

[82] R. M. Kroeze et al. "Spinor Self-Ordering of a Quantum Gas in a Cavity". In: *Phys. Rev. Lett.* 121 (16 2018), p. 163601.

[83] L. Carl et al. "Phases, instabilities and excitations in a two-component lattice model with photon-mediated interactions". In: *Physical Review Research* 5.3 (2023), p. L032003.

[84] N. Dogra et al. "Phase transitions in a Bose-Hubbard model with cavity-mediated global-range interactions". In: *Physical Review A* 94.2 (2016), p. 023632.

[85] V. D. Vaidya et al. "Tunable-Range, Photon-Mediated Atomic Interactions in Multimode Cavity QED". In: *Phys. Rev. X* 8 (1 2018), p. 011002.

[86] H. Hosseinabadi, D. E. Chang, and J. Marino. "Quantum-to-classical crossover in the spin glass dynamics of cavity QED simulators". In: *Phys. Rev. Res.* 6 (4 2024), p. 043313.

[87] H. Hosseinabadi, D. E. Chang, and J. Marino. "Far from equilibrium field theory for strongly coupled light and matter: Dynamics of frustrated multimode cavity QED". In: *Phys. Rev. Res.* 6 (4 2024), p. 043314.

[88] F. Mivehvar, H. Ritsch, and F. Piazza. "Cavity-Quantum-Electrodynamical Toolbox for Quantum Magnetism". In: *Phys. Rev. Lett.* 122 (11 2019), p. 113603.

[89] F. Mivehvar, F. Piazza, and H. Ritsch. "Disorder-Driven Density and Spin Self-Ordering of a Bose-Einstein Condensate in a Cavity". In: *Phys. Rev. Lett.* 119 (6 2017), p. 063602.

[90] F. Dimer et al. "Proposed realization of the Dicke-model quantum phase transition in an optical cavity QED system". In: *Phys. Rev. A* 75 (1 2007), p. 013804.

[91] S. B. Jäger et al. "Lindblad Master Equations for Quantum Systems Coupled to Dissipative Bosonic Modes". In: *Phys. Rev. Lett.* 129 (6 2022), p. 063601.

[92] F. m. c. Damanet, A. J. Daley, and J. Keeling. "Atom-only descriptions of the driven-dissipative Dicke model". In: *Phys. Rev. A* 99 (3 2019), p. 033845.

[93] M. Xu. "Theory of steady–state superradiance". PhD thesis. University of Colorado at Boulder, 2016.

[94] R. U. Haq, S. S. Bharadwaj, and T. A. Wani. *An Explicit Method for Schrieffer-Wolff Transformation*. 2019. arXiv: 1901.08617 [cond-mat.str-el].

[95] S. A. Bender, R. A. Duine, and Y. Tserkovnyak. "Electronic Pumping of Quasiequilibrium Bose–Einstein–Condensed Magnons". In: *Phys. Rev. Lett.* 108 (24 2012), p. 246601.

[96] B. Flebus et al. "Two-Fluid Theory for Spin Superfluidity in Magnetic Insulators". In: *Phys. Rev. Lett.* 116 (11 2016), p. 117201.

[97] A. Kamenev. *Field Theory of Non-Equilibrium Systems*. 2nd ed. Cambridge University Press, 2023.

[98] F. Iemini, D. Chang, and J. Marino. *Dynamics of inhomogeneous spin ensembles with all-to-all interactions: breaking permutational invariance*. 2023. arXiv: 2309.10746 [quant-ph].

[99] R. J. Valencia-Tortora et al. "Crafting the dynamical structure of synchronization by harnessing bosonic multilevel cavity QED". In: *Phys. Rev. Res.* 5 (2 2023), p. 023112.

[100] J. Johansson, P. Nation, and F. Nori. "QuTiP 2: A Python framework for the dynamics of open quantum systems". In: *Computer Physics Communications* 184.4 (2013), pp. 1234–1240.

[101] H. Weimer, A. Kshetrimayum, and R. Orús. "Simulation methods for open quantum many-body systems". In: *Reviews of Modern Physics* 93.1 (2021), p. 015008.

[102] A. Polkovnikov. "Phase space representation of quantum dynamics". In: *Annals of Physics* 325.8 (2010), pp. 1790–1852.

[103] L. J. Bond et al. *Open quantum dynamics with variational non-Gaussian states and the truncated Wigner approximation*. 2024. arXiv: 2407.02617 [quant-ph].

[104] C. D. Mink, D. Petrosyan, and M. Fleischhauer. "Hybrid discrete-continuous truncated Wigner approximation for driven, dissipative spin systems". In: *Phys. Rev. Res.* 4 (4 2022), p. 043136.

[105] J. Huber, A. M. Rey, and P. Rabl. "Realistic simulations of spin squeezing and cooperative coupling effects in large ensembles of interacting two-level systems". In: *Phys. Rev. A* 105 (1 2022), p. 013716.

[106] J. Schachenmayer, A. Pikovski, and A. M. Rey. "Many-Body Quantum Spin Dynamics with Monte Carlo Trajectories on a Discrete Phase Space". In: *Phys. Rev. X* 5 (1 2015), p. 011022.

[107] W. K. Wootters. "A Wigner-function formulation of finite-state quantum mechanics". In: *Annals of Physics* 176.1 (1987), pp. 1–21.

[108] B. Sundar, K. C. Wang, and K. R. A. Hazzard. "Analysis of continuous and discrete Wigner approximations for spin dynamics". In: *Phys. Rev. A* 99 (4 2019), p. 043627.

[109] J. Huber, P. Kirton, and P. Rabl. "Phase-space methods for simulating the dissipative many-body dynamics of collective spin systems". In: *SciPost Phys.* 10 (2021), p. 045.

[110] L. Pucci, A. Roy, and M. Kastner. "Simulation of quantum spin dynamics by phase space sampling of Bogoliubov-Born-Green-Kirkwood-Yvon trajectories". In: *Phys. Rev. B* 93 (17 2016), p. 174302.

[111] A. Piñeiro Orioli et al. "Nonequilibrium dynamics of spin-boson models from phase-space methods". In: *Phys. Rev. A* 96 (3 2017), p. 033607.

[112] C. Qu and A. M. Rey. "Spin squeezing and many-body dipolar dynamics in optical lattice clocks". In: *Phys. Rev. A* 100 (4 2019), p. 041602.

[113] J. Gelhausen and M. Buchhold. "Dissipative Dicke model with collective atomic decay: Bistability, noise-driven activation, and the nonthermal first-order superradiance transition". In: *Phys. Rev. A* 97 (2 2018), p. 023807.

[114] L. M. Sieberer, M. Buchhold, and S. Diehl. "Keldysh field theory for driven open quantum systems". In: *Reports on Progress in Physics* 79.9 (2016), p. 096001.

[115] M. Gross and S. Haroche. "Superradiance: An essay on the theory of collective spontaneous emission". In: *Physics Reports* 93.5 (1982), pp. 301–396.

[116] S. J. Masson et al. "Many-Body Signatures of Collective Decay in Atomic Chains". In: *Phys. Rev. Lett.* 125 (26 2020), p. 263601.

[117] D. Meiser et al. "Prospects for a millihertz-linewidth laser". In: *Physical review letters* 102.16 (2009), p. 163601.

[118] G. Ferioli et al. "Non-Gaussian Correlations in the Steady State of Driven-Dissipative Clouds of Two-Level Atoms". In: *Physical Review Letters* 132.13 (2024), p. 133601.

[119] L. Henriet et al. “Critical open-system dynamics in a one-dimensional optical-lattice clock”. In: *Phys. Rev. A* 99 (2 2019), p. 023802.

[120] K. Seetharam et al. “Correlation engineering via nonlocal dissipation”. In: *Phys. Rev. Res.* 4 (1 2022), p. 013089.

[121] K. Seetharam et al. “Dynamical scaling of correlations generated by short- and long-range dissipation”. In: *Phys. Rev. B* 105 (18 2022), p. 184305.

[122] G. Passarelli et al. “Dissipative time crystals with long-range Lindbladians”. In: *Physical Review B* 106.22 (2022), p. 224308.

[123] F. Iemini et al. “Boundary time crystals”. In: *Physical review letters* 121.3 (2018), p. 035301.

[124] L. Novotny and B. Hecht. *Principles of nano-optics*. Cambridge university press, 2012.

[125] C. D. Mink and M. Fleischhauer. “Collective radiative interactions in the discrete truncated Wigner approximation”. In: *SciPost Physics* 15.6 (2023), p. 233.

[126] J. Huber, A. M. Rey, and P. Rabl. “Realistic simulations of spin squeezing and cooperative coupling effects in large ensembles of interacting two-level systems”. In: *Phys. Rev. A* 105 (1 2022), p. 013716.

[127] G Ferioli et al. “Laser-driven superradiant ensembles of two-level atoms near Dicke regime”. In: *Physical Review Letters* 127.24 (2021), p. 243602.

[128] C. Qu and A. M. Rey. “Spin squeezing and many-body dipolar dynamics in optical lattice clocks”. In: *Physical Review A* 100.4 (2019), p. 041602.

[129] A. Browaeys and T. Lahaye. “Many-body physics with individually controlled Rydberg atoms”. In: *Nature Physics* 16.2 (2020), pp. 132–142.

[130] J. Zou, S. Zhang, and Y. Tserkovnyak. “Bell-state generation for spin qubits via dissipative coupling”. In: *Physical Review B* 106.18 (2022).

[131] X. Li et al. *A solid-state platform for cooperative quantum dynamics driven by correlated emission*. 2024. arXiv: 2309.08991 [quant-ph].

[132] R. Fazio et al. “Many-body open quantum systems”. In: *arXiv preprint arXiv:2409.10300* (2024).

[133] B. Vacchini. “NON-MARKOVIAN DYNAMICS IN OPEN QUANTUM SYSTEMS”. In: (2011).

[134] O. Goulko et al. “Transient dynamical phase diagram of the spin-boson model”. In: *arXiv preprint arXiv:2402.18561* (2024).

[135] B. Debecker, J. Martin, and F. Damanet. “Spectral theory of non-Markovian dissipative phase transitions”. In: *Physical Review A* 110.4 (2024), p. 042201.

[136] S. P. Kelly, A. M. Rey, and J. Marino. “Effect of active photons on dynamical frustration in cavity QED”. In: *Physical Review Letters* 126.13 (2021), p. 133603.

[137] R. J. Lewis-Swan et al. “Cavity-QED Quantum Simulator of Dynamical Phases of a Bardeen-Cooper-Schrieffer Superconductor”. In: *Phys. Rev. Lett.* 126 (17 2021), p. 173601.

[138] D. J. Young et al. “Observing dynamical phases of BCS superconductors in a cavity QED simulator”. In: *Nature* 625.7996 (Jan. 2024), pp. 679684.

[139] B. P. Marsh et al. “Entanglement and replica symmetry breaking in a driven-dissipative quantum spin glass”. In: *arXiv preprint arXiv:2307.10176* (2023).

[140] Z.-H. Zhu et al. “Probing false vacuum decay on a cold-atom gauge-theory quantum simulator”. In: *arXiv preprint arXiv:2411.12565* (2024).

[141] L. Batini, A. Chatrchyan, and J. Berges. “Real-time dynamics of false vacuum decay”. In: *Physical Review D* 109.2 (2024), p. 023502.

[142] A. De et al. “Observation of string-breaking dynamics in a quantum simulator”. In: *arXiv preprint arXiv:2410.13815* (2024).

[143] N. Defenu, A. Lerose, and S. Pappalardi. “Out-of-equilibrium dynamics of quantum many-body systems with long-range interactions”. In: *Physics Reports* 1074 (2024), pp. 1–92.

[144] N. Defenu et al. “Long-range interacting quantum systems”. In: *Rev. Mod. Phys.* 95 (3 2023), p. 035002.

[145] C. Luo et al. *Realization of three and four-body interactions between momentum states in a cavity through optical dressing*. 2024. arXiv: 2410.12132 [quant-ph].

[146] J. Keeling, M. J. Bhaseen, and B. D. Simons. “Fermionic superradiance in a transversely pumped optical cavity”. In: *Physical Review Letters* 112 (14 Apr. 2014).

[147] F. Piazza and P. Strack. “Quantum kinetics of ultracold fermions coupled to an optical resonator”. In: *Physical Review A - Atomic, Molecular, and Optical Physics* 90 (4 Oct. 2014).

[148] R. M. Sandner et al. “Self-ordered stationary states of driven quantum degenerate gases in optical resonators”. In: *EPL* 111 (5 Sept. 2015).

[149] V. Helson et al. “Density-wave ordering in a unitary Fermi gas with photon-mediated interactions”. In: *Nature* 618 (7966 June 2023), pp. 716–720.

[150] H. Konishi et al. “Universal pair polaritons in a strongly interacting Fermi gas”. In: *Nature* 596 (7873 Aug. 2021), pp. 509–513.

[151] K. Roux et al. “Strongly correlated Fermions strongly coupled to light”. In: *Nature Communications* 11 (1 Dec. 2020).

[152] P. Uhrich et al. *A cavity quantum electrodynamics implementation of the Sachdev-Ye-Kitaev model*.

[153] M. Kitagawa and M. Ueda. “Squeezed spin states”. In: *Physical Review A* 47.6 (1993), p. 5138.

[154] J. D. Wilson et al. “Beyond one-axis twisting: Simultaneous spin-momentum squeezing”. In: *Phys. Rev. A* 106 (4 2022), p. 043711.

[155] M. J. Kastoryano, F. Reiter, and A. S. Sørensen. “Dissipative preparation of entanglement in optical cavities”. In: *Physical review letters* 106.9 (2011), p. 090502.